Red Supergiants as Luminous Beacons of Cosmic Chemical Abundances:

The Infrared J–Band Spectroscopic Technique

A DISSERTATION SUBMITTED TO THE GRADUATE DIVISION OF THE UNIVERSITY OF HAWAIʻI AT MĀNOA IN PARTIAL FULFILLMENT OF THE REQUIREMENTS FOR THE DEGREE OF

DOCTOR OF PHILOSOPHY

IN

ASTRONOMY

August 2014

By
Jonathan Zachary Gazak

Dissertation Committee:

Rolf Kudritzki, Chairperson
Joshua Barnes
Fabio Bresolin
Benjamin Davies
Peter Englert
Lisa Kewley
John Rayner

Acknowledgements

Rolf and I have followed an unspoken rule over the course of my dissertation research. I get the bad weather for my science on Mauna Kea and, in exchange, Rolf takes the abysmal nights. He has pursued blue supergiants in the maser galaxy over and over, and each time I have to send the bad news home. His response is always some variation of "We will try again. It is a good project. I think it is time for a beer." Astronomy can be emotionally trying in this way. Still, I have built a solid dissertation and I owe this to Rolf. Besides inspiring−and sometimes demanding−enthusiasm despite circumstances, Rolf gave to me a freedom in my research that is uncommon. I know it must have been a challenge for him to watch me wander towards a conclusion to which he could see a direct path, but he still waited patiently for my arrival. I like to think, or at least hope, that we learned a thing or two from that meandering. I thank also Miguel Urbaneja, who collaborates closely with Rolf and has on many occasions helped me overcome obstacles and generate ideas for this work.

I owe much to Ben Davies and the team of scientists he has assembled, including Nate Bastian, Maria Bergemann, Chris Evans, Bertrand Plez, and Lee Patrick. Our annual red supergiant meetings are always productive, inspiring, and rejuvenating. We have done a lot of science over the last four years and have plenty more to accomplish.

My committee has treated me well over the years and I appreciate their willingness to help and support my research. I hope they are as content with this body of work as I am.

In early 2013 I enjoyed a short career in trampoline gymnastics. That lasted roughly forty five minutes and ended with a compound tibia and fibula fracture. My friends and family made certain that I never suffered more than the physical pain of that trauma. To that group of friends−especially

Ryan and Kacey Swindle, Lauren Zuckerburg, Megan Ansdell, Gabe Dima, and Garrett Elliot−I will be forever thankful. You put me back on my feet faster than I dared hope.

I know no suitable words with which to express my gratitude towards my parents, John and Julie, my sisters Alexis and Sarah, and my new brother-in-law Jared. There is an indescribable comfort in knowing that these are "my people" and in whatever case I am safe and happy with them. I have run home on more than one occasion and am always met with open arms. I am who I am because of you. I intend that−generally−as a compliment. I share this success with you.

Lucy Rosenthal. You pick me up when I fall and you make me laugh even though we "aren't nearly as funny as we think". My heart to you.

Abstract

A new spectroscopic method has been developed and tested which, with the advent of the next generation of 30 meter class telescopes, will enable the study of the chemical evolution of galaxies through the spectroscopy of individual red supergiant stars out to the Coma cluster of galaxies. This J–band (1.165-1.215 μm) technique requires modest spectral resolutions of $\lambda/\delta\lambda \sim 3000$, enabling multi object spectroscopy using existing 8 meter telescopes (Keck, VLT) and future "extremely large telescopes" such as the Thirty Meter Telescope.

We demonstrate the power of the technique and study its limitations with high spectral resolution observations of the galactic h and χ Persei clusters and then set our sights outward. We observe a population of RSGs in M31 using MOSFIRE on Keck and measure the central metallicity and gradient using individual supergiants in NGC 300 at 1.9 Mpc with KMOS on the VLT.

Following these successes we demonstrate an extension of the technique by proving that the J–band method is applicable to the integrated light of super star clusters. These distant, massive coeval ensembles of stars present as red supergiants photometrically and spectroscopically when the first such stars evolve after roughly six million years. We provide a photometric technique to select properly aged clusters and apply the technique to two test cases, a super-solar cluster in M83 and a sub-solar cluster in NGC 6946. After the successful applications to those clusters we observed three super star clusters in the Antennae galaxies at 20 Mpc and extract metallicity information from their J–band spectra without difficulty. This application over such a distance is a stunning success for a stellar chemical abundance technique and with it in hand we offer the J–band technique as

a powerful new tool for the study of galaxy evolution and the chemical enrichment of a significant volume of the local universe.

Table of Contents

List of Tables

List of Figures

Chapter 1

Introduction

1.1 Motivation: Extragalactic Metallicities

Measuring metallicities in star-forming galaxies is a ubiquitous goal across the field of extragalactic astronomy. The evolutionary state of a galaxy is imprinted in the central metallicity and radial abundance gradient of iron- and α-group elements. Observed trends in these measurements across ranges of galactic mass, redshift, and environment constrain the theory of galaxy formation and chemical evolution. Central metallicity is dictated by galactic mass, a relationship encoded by the initial properties and evolution of these objects (Lequeux et al. 1979; Tremonti et al. 2004; Maiolino et al. 2008). Radial metallicity gradients provide a wealth of information needed to describe the complex dynamics of galaxy evolution including clustering, merging, infall, galactic winds, star formation history, and initial mass function (Prantzos & Boissier 2000; Garnett 2004; Colavitti et al. 2008; Yin et al. 2009; Sánchez-Blázquez et al. 2009; De Lucia et al. 2004; de Rossi et al. 2007; Finlator & Davé 2008; Brooks et al. 2007; Köppen et al. 2007; Wiersma et al. 2009).

The pursuit of these scientific goals has been compromised by the difficulty of obtaining reliable metallicities. Investigations tend to rely on spectroscopy of the emission lines of H II regions. These methods require empirical calibration and choosing different commonly used calibrations yields varying and sometimes conflicting results from the same set of observations. Both the slope and absolute scaling of metallicity are susceptible to choice of calibration: the mass-metallicity dependence across all galaxies and the radial gradients within individual galaxies can change from

steep to flat while the overall metallicity can shift by a factor of up to four (Kewley & Ellison 2008; Kudritzki et al. 2008; Bresolin et al. 2009a). Even the more physical "T_e−based method" (which utilizes auroral lines to remove the need for "strong line" calibrations) is potentially subject to biases−especially in the metal rich regime characteristic of the disks of all massive spiral galaxies (Bergemann et al. 2014; Stasińska 2005; Bresolin et al. 2005; Ercolano et al. 2010; Zurita & Bresolin 2012).

One technique which avoids the uncertain calibrations of the "strong line" H II region method is the quantitative spectroscopy of supergiant stars. Blue supergiants (BSGs) have become a powerful tool for measuring metallicities, gradients, and distances to galaxies in and beyond the Local Group. This technique, while extremely promising, may also be subject to systematic uncertainties and needs to be checked by independent methods. Moreover, it requires optical spectroscopy while the next generation of telescopes such as the TMT and E–ELT will be optimized for observations at infrared wavelengths, using adaptive optics supported multi object spectrographs. Thus, we need bright abundance tracers which radiate strongly in the IR. Evolved stars–including red giants, the asymptotic giant branch, and red supergiants–will have a clear priority in future spectroscopic investigations.

The extremely luminous red supergiant stars (RSGs)—which emit 10^5 to $\sim 10^6$ $L/L_\odot$ largely in the infrared (Humphreys & Davidson 1979)—thus become ideal targets for measuring extragalactic cosmic abundances. Complications due to the densely packed spectral features characteristic of the cool, extended atmospheres of RSGs are minimized in the J–band. Here the dominant features are isolated atomic lines of iron, titanium, silicon, and magnesium. Molecular lines of OH, H_2O, CN, and CO manifest weakly or not at all in this bandpass. A new technique proposed by Davies, Kudritzki, & Figer (2010) (henceforth DFK10) has demonstrated that quantitative, medium resolution spectroscopy (R $[\lambda/\delta\lambda]$ $\sim$3000) in the J–band can, in principle, determine metallicities accurate to $\sim$0.15 dex for a single RSG. While a principal limitation of the quantitative spectroscopy of stars is distance, these supergiant studies using 8-meter class telescopes have the potential to be extended to $\sim$10 Mpc (Evans et al. 2011).

A RSG J–band technique would thus be poised to study a substantial volume of the local universe, one containing groups and clusters of galaxies. The determination of accurate abundances for the RSG populations of star forming galaxies in this volume would provide an unparalleled observational constraint for models of galaxy formation and evolution. Increased utilization of supergiant stars may also aid in the further development of the observationally efficient H II-region methods while providing independent alternate measurement technique to the blue supergiants.

Still, DFK10 is a pilot study of the J–band technique and the analysis methods to best study these stars require careful development and testing. Studies of RSGs have classically required high resolutions (R$\sim$20,000) in the H–band in order to separate and study the dense forest of atomic and molecular features present throughout their spectra. Part of this requirement is driven by the scientific desire to study stellar evolution, for which abundances of C, N, and O are important. The J–band technique returns only information about metallicity and no information specific to CNO processing and in exchange avoids the high observational overloads inherent to such studies. This repurposing for extracting global chemical enrichment at modest resolution is novel.

1.2 Dissertation Outline

The intent of this dissertation is twofold. The primary goal is to develop and exploit spectroscopic techniques for a new, independent stellar population capable of providing reliable chemical enrichment information and an additional test on the BSG methods discussed above. The RSGs represent a natural choice for this new population, and we utilize the remainder of this introductory chapter to develop that line of reasoning. In Chapter 2 we describe the theoretical and mathematical development of the J–band technique (Gazak et al. 2014b). The algorithms developed for this work are discussed and we describe a careful study on a nearby population of RSGs which defines the observational requirements to obtain accurate and precise metallicities across extragalactic distances.

With the J–band technique in hand, we use Chapter 3 to present the studies of three populations of RSGs completed over the course of this dissertation. The first study uses the same dataset as

Chapter 2, namely the RSG members of the Milky Way's h and χ Persei cluster as observed with IRCS on Subaru. We then move out of the galaxy and observe a population of RSGs in the star forming disk of the Local Group galaxy M31. This study is incomplete, as the required night with MOSFIRE on Keck was affected by significant cloud cover. We discuss the data recovered and have obtained additional time on MOSFIRE to complete this study. Finally, we leave the Local Group and observe RSGs across the disk of the southern galaxy NGC 300. This study utilized the newly commissioned KMOS multi object IFU spectrograph at the VLT, and we find excellent agreement between our J–band measurements of central metallicity and metallicity gradient with parallel studies using BSGs and T_e-based H II region techniques.

In Chapter 4 we describe the secondary goal of this dissertation, the application of our J–band technique to the integrated light of super star clusters (SSCs). While pursuing the fertile scientific opportunities proffered by single RSGs we furthered the development of the J–band technique for application across even greater distances using tens to hundreds of RSGs in young SSCs. We discuss the dominance of these stars on the IR luminance of SSCs. First (as in Gazak et al. 2013) we develop a population synthesis code along the lines of starburst99 or galex with functionality only for single bursts of star formation but with a powerfully flexible choice of stellar evolution framework and inclusion of the latest and greatest grid of MARCS models and TURBOSPECTRUM synthetic spectra for RSGs. We show that the evolution of massive stars into RSGs initiates a distinct hysteresis in color. The age of SSCs can be differentiated by this shift using only infrared photometry thus far simplifying target selection for studies requiring RSG dominated SSCs. We follow by describing modifications to our population synthesis code to output near IR spectra of SSCs of proper resolution to study the contaminative effects of the remaining stellar population. As part of that work we study two SSCs, one observed in NGC 6946 with SpeX on IRTF and another in M83 observed with ISAACS on the VLT (Gazak et al. 2014a). As the final scientific application of the J–band technique towards the completion of this dissertation we present a measurement of the metallicity of the merging Antennae galaxies (NGC 4038 and 4039) at a distance of 20 Mpc. This is a bold step out into the universe for the measurement of metallicities using accurate and precise supergiant star techniques.

In Chapter 5 we conclude the dissertation with an overview of the work completed and a discussion of future perspectives for the fields of quantitative spectroscopy and extragalactic astronomy.

1.3 Existing Techniques: H II Regions

The emission line spectrum of a H II region is the product of an ultraviolet radiation field from one or more massive stars interacting with a surrounding nebular region. As that radiation ionizes atomic species in the nebula, an equilibrium develops between the rate of ionization and recombination. Excess ionization energy is carried by free electrons which normalize into an electron gas with a characteristic temperature T_e. The energy in this gas excites atomic species and de-excitation releases energy from the H II region in the form of emission lines. A full set of parameters to model such a system is quite large, including the population and parameters of the ionizing stars, the geometry of those stars and the nebula, and the structure of the nebula itself.

For a proper abundance determination, the measurement of T_e is critical. Line strengths depend heavily on the temperature of the electron gas and disentangling the amount of oxygen from its level of ionization is otherwise not possible. That temperature dictates the ratio of emission from the faint auroral line ratio of [O III] at rest wavelengths of 4363 and 5007 angstroms and, so can be measured effectively using these lines. Studies using this direct method of measurement agree with abundances derived from populations of stars in environments where metallicity is below solar, for example, dwarf galaxies (Stasińska 2005; Bresolin et al. 2006; Lee et al. 2006), and for some regions in the Milky Way and M33 (MW: Rolleston et al. 2000; Deharveng et al. 2000; Daflon & Cunha 2004, M33: Vilchez et al. 1988; Urbaneja et al. 2005; Magrini et al. 2007; Rosolowsky & Simon 2008). Finally, work across the radial extent of the southern spiral galaxy NGC 300 shows excellent agreement with other metallicity indicators (Kudritzki et al. 2008; Bresolin et al. 2009a). Issues with the direct T_e method remain, though, as a single value of T_e does not necessarily adequately describe the complex and variable temperature structure within an individual H II region (Bresolin et al. 2009a).

At higher metallicities the auroral [O III] lines grow faint as cooling mechanisms begin to favor infrared transitions. In these cases, or when the signal to noise of the data is not enough to measure the [O III] lines effectively, scientists apply a host of "strong line" methods which use line ratios of the strongest emission lines in H II regions. These ratios are empirically calibrated or utilize extreme simplifying assumptions when dealing with H II regions. In this way the strong cooling emission lines have been adapted as tracers of metallicity without any direct tie to the physics of the situation. The theoretical and empirical calibrations of these lines have significant issues when applied to individual H II regions. The complexity of these systems are reduced by a significant set of assumptions, outlined by Pagel et al. (1979). These include reducing the stellar population to a single star, or at least stars of identical type, that the H II region is a collection of small identical clouds surrounded by empty space, and that oxygen abundance is the sole determinant of nebular cooling. These are bold assumptions. As one strong line example we describe that work by Pagel et al. (1979), in which the H II region is defined by three parameters: the temperature of the star, the oxygen abundance of the nebula, and a geometric factor describing the density of those small, isolated clouds.

A third method, the strength of O II recombination lines, returns abundances in disagreement with collisionally excited [O III] lines. This issue is known as the "abundance discrepancy" in photoionization regions and manifests as recombination line abundance measurements which are a factor of up to two too high when compared to collisional measurements (García-Rojas & Esteban 2007). This discrepancy is likely due to temperature fluctuations within the region and stresses again the difficult task of developing robust assumptions for such complicated physical systems.

1.4 Existing Techniques: Blue Supergiants

1.4.1 In The Milky Way

Stellar spectroscopists have long known that the best tracers of metallicity are the stars, those objects which both drive the creation of the heavier elements and provide the radiative power illuminating the universe. The promise of quantitative spectroscopy of BSGS began with Groth

(1961) presenting a measurement of the stellar parameters and chemical composition of Deneb. In the next decade, studies in the Milky Way and Magellanic Clouds provided additional measurements of the abundances of A supergiants (Wolf 1971, 1972, 1973). These early groundbreaking studies were to see significant improvement with the advent of NLTE model atmospheres and the realization (in the doctoral thesis of my committee chair) that the low gravity atmospheres of such stars could be strongly affected by NLTE effects (Kudritzki 1973). The development of improved NLTE model atmospheres bore fruit decades later in work by Venn (1995a,b) and Aufdenberg et al. (2002) on BSGs in the Milky Way. This work has continued to advance with observational and theoretical efforts increasing the precision of abundance measurements and range of elements studied. Przybilla et al. (2006) use tens of thousands of lines in NLTE in the determination of stellar parameters and abundances with high precision, including individual metal abundances to within $\sim$0.05 dex.

1.4.2 Extragalactic Applications

The exciting possibility of deriving metallicities from individual stars themselves still had the significant limitation that high spectral resolution is required and signal to noise requirements are based on continuum level emission as opposed to a set of bright emission lines. This meant that telescopes could observe one star at a time through a narrow longslit. This limited extragalactic applications to our nearest neighbors, the Magellanic Clouds. With the advent of 8m class telescopes, these methods were extended into the Local Group of galaxies (SMC – Venn 1999; M33 – McCarthy et al. 1995; M31 – McCarthy et al. 1997; Venn et al. 2000; NGC 6822 – Venn et al. 2001; WLM – Venn et al. 2003; Sextans A – Kaufer et al. 2004).

Still, the potential benefits of extragalactic stellar astronomy drove researchers to seek enhancements on existing methods. The goal is to derive chemical abundances across the disks of star forming galaxies from the rich atomic absorption spectra of the stars themselves, instead of relying solely on ambiguous H II region calibrations floating atop oxygen alone. The concept of reaching so far with individual supergiant stars was presented and discussed by Kudritzki et al. (1995) and in Kudritzki (1998). Driven by that work and the construction and commissioning of the low resolution FORS multi object spectrograph (MOS) at the VLT, Bresolin et al. (2001) and

Bresolin et al. (2002) broke the technological barriers limiting BSG techniques to the Local Group, with observations of individual supergiants in NGC 3621 (6.7 Mpc) and NGC 300 (1.9 Mpc).

The power of the BSG technique was significantly extended again by Kudritzki et al. (2003) and Kudritzki et al. (2008) who used a correlation between absolute bolometric magnitude and a flux weighted gravity $g_f = g/T_{eff}^4$ (FGLR) to derive distances to galaxies as well as the metallicities of their star forming disks. This FGLR utilizes the speed with which BSGs evolve across the Hertzsprung-Russell diagram (HRD) towards the RSG phase. During this evolution the mass and luminosities of these stars do not change and a simple theoretical relationship between luminosity and g_f exists.

The combination of metallicities and distances has driven a multitude of studies in and beyond the Local Group and the teams pursuing it remain scientifically lively as they push the limits of the existing methodologies (WLM – Bresolin et al. 2006; Urbaneja et al. 2008; NGC 3109 – Evans et al. 2007; IC1613 – Bresolin et al. 2007; M33 – U et al. 2009; M81 – Kudritzki et al. 2012; NGC 4258 – Kudritzki et al. 2013; NGC 3109 – Hosek et al. 2014; NGC 3621 – Kudritzki et al. 2014)

1.5 The Potential of Red Supergiants

RSGs are evolutionary successors to BSGs and, having evolved quickly through the main sequence, represent with similar fidelity the chemical makeup of the present day interstellar medium. The extreme luminosities of RSGs peak at $\sim 1\mu$m with absolute J-band magnitudes of $M_J = -8$ to -11. Their spectra in this bandpass are rich with features providing diagnostics for extraction of accurate abundances of multiple elements. To date the crippling limitation of utilizing RSGs for extragalactic work has been the need for spectral resolution in excess of R=20,000. However, the recent work by DFK10 has demonstrated a promising technique to access accurate chemical composition information from quantitative spectroscopy in the J band (1.15-1.23 μm) with resolution requirements of only R $\sim$2000-3000. As a result of this and instrumentation recently commissioned at Keck (MOSFIRE) and the VLT (KMOS), we have the opportunity to exploit RSGs as an independent probe of chemical enrichment to distances of up to $\sim$10 Mpc. While

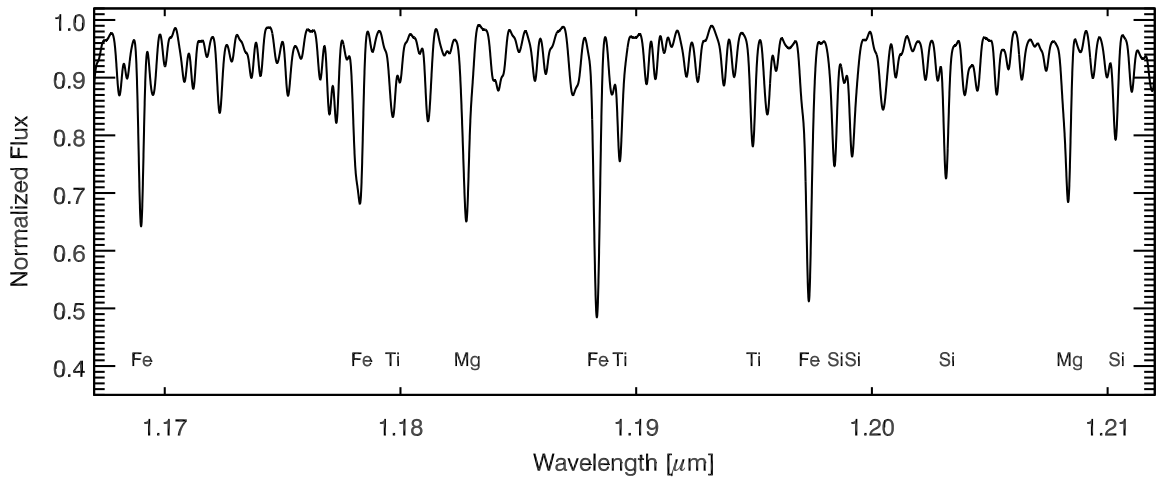

Figure 1.1 The J–band spectrum of a red supergiant. The resolution of the spectrum plotted is R $[\lambda/\delta\lambda] = 5000$. In this work we provide a technique to precisely and accurately study such stars in this spectral bandpass to resolutions below 3000 (see Figure 1.4). The critical diagnostic features are labeled. This synthetic spectrum is calculated using LTE MARCS stellar models and non-LTE corrections for the diagnostic features of Ti, Fe, and Si. Similar corrections for Mg are in development.

this work is posed to provide crucial results, the future implications are even brigher. With the next generation of ELTs−equipped with multi-conjugate adaptive optics optimized in the IR−this range can be extended to at least 30 Mpc and possibly out to ∼100 Mpc, meaning that the RSG populations of entire clusters of galaxies will become accessible targets (Evans, Davies, Kudritzki et al. 2011).

The J–band offers significant benefits over other IR windows. First, molecular absorption lines of OH, H_2O and CO are weak and appear as a pseudocontinuum at low resolution. This leaves as dominant spectral features Fe and the α-elements Si, Ti, and Mg−meaning that RSGs provide a unique opportunity to directly measure iron and alpha element abundances. For reference we plot a J–band spectrum at spectral resolution of R = 5000 in Figure 1.1. In general, these dominant features are separated such that blending is not an issue and of sufficient strength to study at low resolution. Furthermore, the IR excess due to circumstellar material often found in RSGs contributes only negligibly to the J–band, such that there is no dilution of stellar absorption lines. Similarly, interstellar reddening is suppressed in comparison to visible wavelengths which allows

more freedom in target selection and simplifies analysis techniques. As a final crucial advantage, the J–band is well-covered by existing and planned instrumentation as it is an ideal wavelength range to take full advantage of adaptive optics performance.

1.5.1 Evolution of Red Supergiants

When the most massive stars (those with $M_{init} \geq 8M_{\odot}$) exhaust their core hydrogen, their cores begin to collapse and fuse heavier elements. This departure from the main sequence occurs in a progression based on the balance between ongoing helium burning and the radiative escape of energy released. As the cores of these stars shrink and compress, the outer layers begin to expand and rarify. The physics behind this inverse behavior remains an open theoretical topic but the observational effect is undeniable. These super giant stars cool rapidly at near constant luminosity, first through the still hot BSG phase and finally, after reaching stellar radii of a few astronomical units, they enter the RSG phase. The RSGs are the largest, coolest stars, existing at the borderline for fully convective stars in the Hertzsprung-Russell diagram, the "Hayashi Limit". In their further evolution, RSGs may "climb" somewhat along the Hayashi limit and/or exercise "blue loops" before exploding as type II core collapse supernovae following the onset of carbon burning.

This scenario represents a simplification of a complicated reality, but is an apt description of those stars with initial masses between 8 and 17 $M_{\odot}$. The description ignores a varied set of phases in the evolution of massive stars including the Wolf Rayet stars and Luminous Blue Variables which may occur after a star has entered the RSG phase. In addition, as a result of heavy mass loss through radiation driven stellar winds in stars larger than 40 $M_{\odot}$the progressive periods of fusion and collapse in the core occur faster than the outer star can expand. In these cases a Wolf-Rayet phase and supernova occur before the stellar atmosphere cools to the RSG phase of $T_{\rm eff} \simeq$ 3400-4400 K. Furthermore, while RSGs with masses between 17 and 35 $M_{\odot}$ are observed (see our work in NGC 300 in Chapter 3; Levesque et al. 2005), type II progenitors of such mass are *not* seen (Smartt 2009). More massive progenitors appear as blue supergiants, such that above certain masses there is an evolutionary pathway back towards hotter temperatures after the RSG phase

and before stellar death. The details of this phase of stellar evolution are also complicated by the effects of binary evolution.

While our understanding of the complicated physics of massive star evolution continues to develop, the basic point for this dissertation is that the RSGs exist and, due to their extreme luminosities and low temperatures, are a critical population of stars in the universe in the near-IR. In Figure 1.2 we demonstrate this with modeled RSG spectral energy distributions ranging from temperatures of 3400 to 4400 K.

1.5.2 The Low Resolution J−Band Technique

Historically RSGs have been studied either locally at high resolution in the H and K bands or at greater distances, such as LMC, SMC, M31, and M33 with optical spectroscopy at modest spectral resolutions. This limited the use of the rich metal line spectra of these objects. High resolutions require unreasonable exposure times at extragalactic distances, and due to the low temperatures of these objects, optical spectroscopy is far less efficient than IR spectroscopy. The optical region of the spectra are dominated by strong band heads of TiO, which complicates measurements of metallicity and, with the current state of RSG stellar models, returns incorrect measurements of temperature (Davies et al. 2013). RSGs can be highly reddened by their own mass loss above that of the line of sight reddening. This has a significant effect on the optical spectra and can be difficult to disentangle from effects of stellar parameters in low resolution spectroscopy.

The ideal case is to exploit the flux peaks of these extremely luminous IR sources and to be able to do so at low resolution. In this way multi-object spectroscopy and models which better reproduce the observed spectra could be used to make RSGs into a powerful new probe of extragalactic chemical abundances.

In the H and K bands, however, strong molecular bands make observations at lower resolution extremely difficult to quantitatively study (see, for example, Figure 1.3). Even with ideal atomic information on the dense forests of these regions, the free parameters in such spectra include also the level of CNO processed dredge up material at the surface.

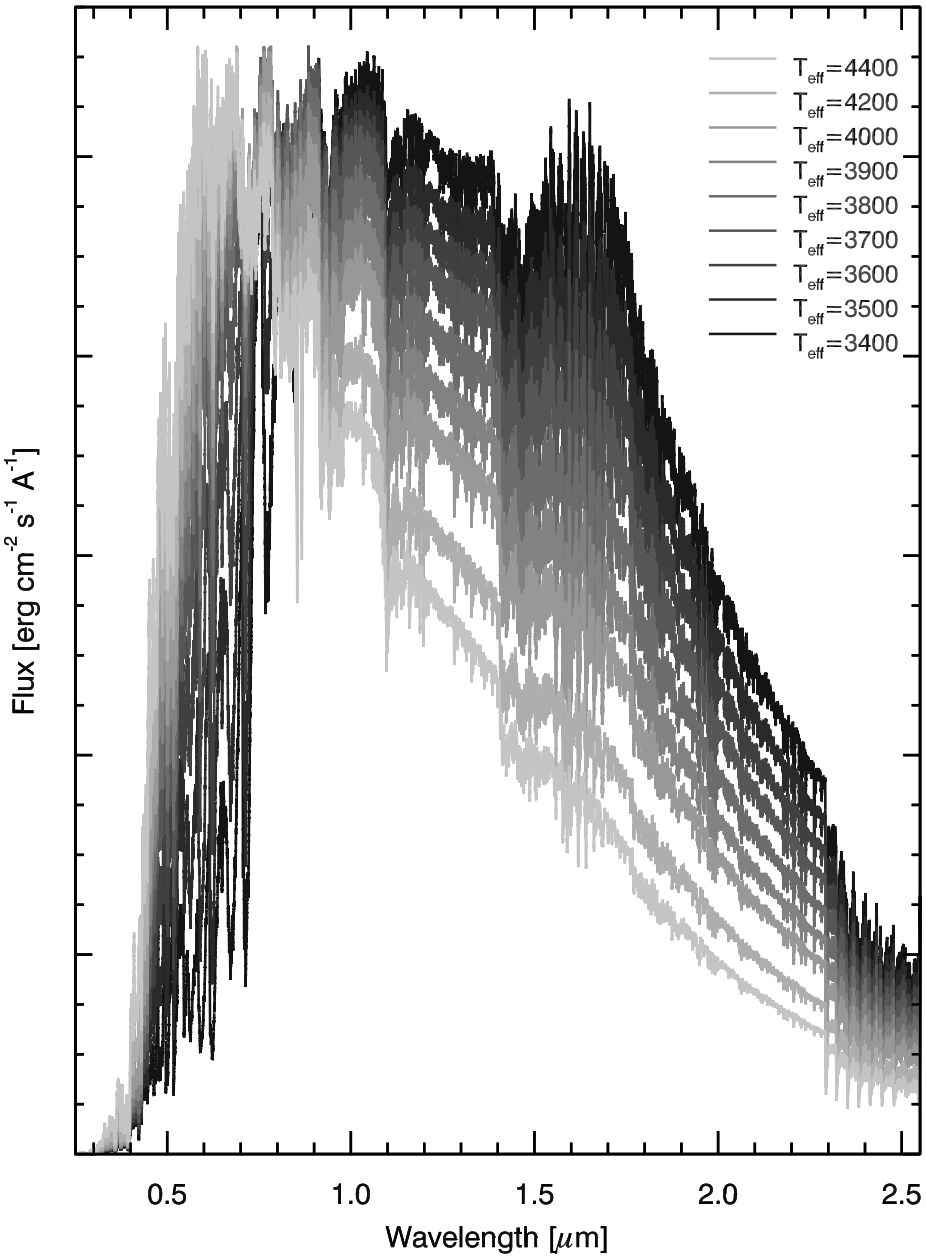

Figure 1.2 Example spectral energy distributions (SEDs) of RSGs at a variety of temperatures. Note that optical flux is largely suppressed by absorption by strong molecular features leaving the peak radiance in the near-IR. SEDs are generated using TURBOSPECTRUM on MARCS stellar models.

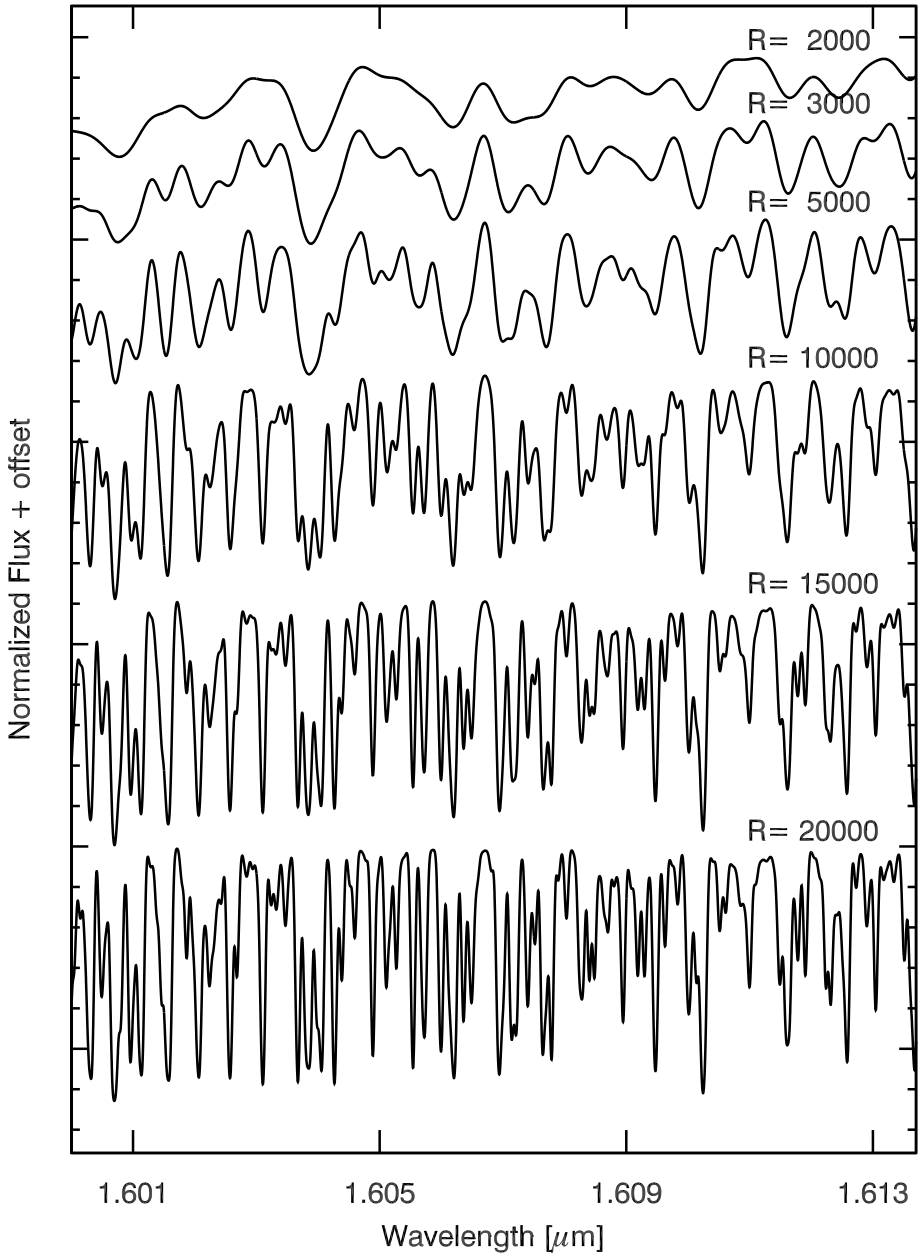

Figure 1.3 A narrow spectral slice of the H–band spectral window for comparison to the spectral form of the J–band (Figure 1.4). Note the extreme density of lines with no significantly stronger or well isolated features. The majority of these lines are due to molecular transitions and blend into a spectrum which is hopeless to study in a quantitative spectroscopic sense at low resolution.

The authors of DFK10 first proposed that the true power of RSGs as metallicity indicators could be realized in the J–band, where complications due to the densely packed spectral features associated with the cool, extended atmospheres of RSGs are minimized. As visualized in Figure 1.4, the morphology of the spectra remains distinct down to low resolutions.

Multiple facets of ongoing research examine the limitations and systematic uncertainties of the technique in great detail. Davies et al. (2013) provide a thorough investigation of the temperature scale of RSGs in the LMC and SMC and conclude that previous work at optical wavelengths yields effective temperatures which are too cool for these RSGs. They find that MARCS models which fit the strong optical TiO bands produce too little flux in the infrared to fit observed RSG spectral energy distributions. This discrepancy manifests in low measurements of effective temperature when fitting is performed with optical spectroscopy alone. This problem greatly reduced in the near-IR, which reveals deeper atmospheric layers. Additional research is assessing the significance−and observational effects−of the local thermodynamic equilibrium (LTE) assumption in calculations of synthetic spectra produced by the MARCS models. Departures from LTE have been calculated for iron and titanium (Bergemann et al. 2012) and silicon lines (Bergemann et al. 2013) in the J–band. Due to the low density environments in the extended atmospheres of RSGs, NLTE effects are noticeable and can be significant. For this work we have access to synthetic spectra calculated in both LTE (TURBOSPECTRUM − Alvarez & Plez 1998; Plez 2012) and with iron, titanium, and silicon lines in NLTE using the results from Bergemann et al. (2012, 2013). Chapters 2 and 3 will describe the technique and its detailed applications.

1.5.3 Extending the Baseline: Super Star Clusters

With a well tested J–band method in hand, current instrumentation on 8-meter class telescopes can extract accurate and precise metallicities using single RSGs out to a limiting distance of ∼10 Mpc (Evans et al. 2011). Still, to reach groups and clusters of galaxies significantly beyond the 10 Mpc, such techniques must await the next generation of 30-meter class telescopes. In Chapter 4 we demonstrate a new method for extending the observational baselines of stellar techniques by exploiting our low resolution methodology on the integrated light of coeval ensembles of stars.

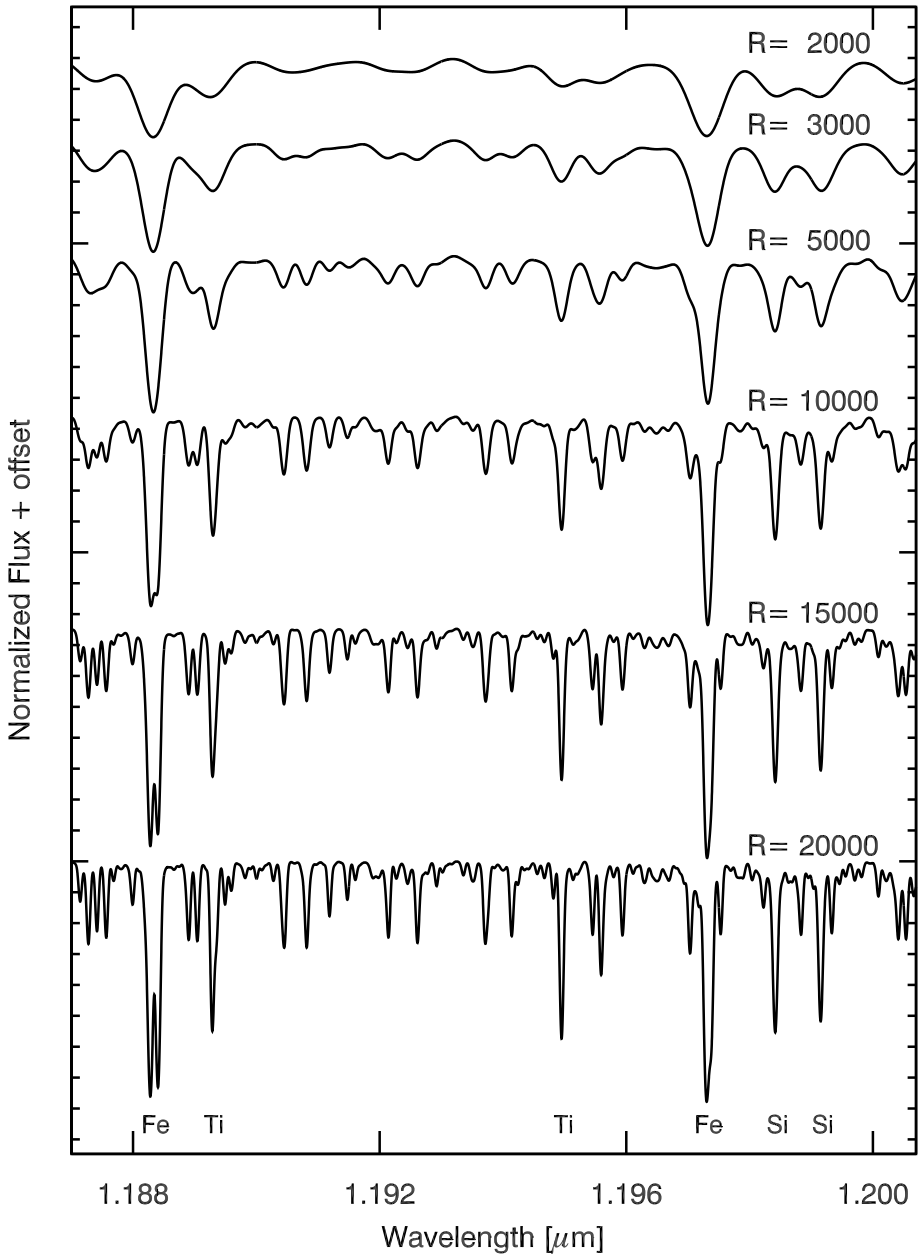

Figure 1.4 A narrow spectral slice of the J–band spectral window. The full width is 1.165-1.215 in the context of this work. Note that the effects of decreasing resolution include shallower lines and blending, but that the strongest features remain obvious down to resolutions of at least R$\sim$3000. These are the diagnostic atomic lines of Fe I, Ti I, and Si I used in this work. For comparison, see the density typical of the H band over the same spectral width in Figure 1.3.

In star forming galaxies, such populations exist as super star clusters (SSCs), the result of single bursts of star formation creating a population with a stellar mass of 10^4-10^6 $M_\odot$ in a tight association (Portegies Zwart et al. 2010). As the stars with masses in the range necessary to become RSGs begin to leave the main sequence, a steady flow of decreasingly luminous but increasingly numerous supergiant stars enter the RSG phase. As this flow begins it initiates a drastic change in the photometric colors of the cluster as the brightest stars in these clusters either explode as supernovae or shift the radiative power of their SEDs into the near IR (Figure 1.2).

In Gazak et al. (2013) we hypothesized that a discrete jump in the IR colors of SSCs at ages beyond 6 Myrs was caused by the appearance and flux dominance of the RSG members of these clusters. We demonstrated this to be the case by performing population synthesis experiments with synthetic photometry. The simulations agreed well with observed near IR colors of SSCs across a range of ages in M83 measured by Bastian et al. (2011, 2012). Indeed, by 6 Myr the population of tens to hundreds of RSGs dominates the near-IR light, commanding $\geq$ 90-95% of the J–band flux (Gazak et al. 2013). As a natural extension of that work we suggested that SSCs older than 6 Myr could be used for quantitative spectroscopy and the measurement of metallicity (Z) at far greater distances than is possible for single supergiants. We will follow up on this in Chapter 4.

Chapter 2

Calibrating the J–Band Technique

In this chapter we carefully study the proposed method of DFK10 and develop a proper understanding of the strengths, limitations, and systematics of the J–band technique. The ideal target for such a study is a nearby coeval population of RSGs, such that we may study the stars as individual objects and then test the potential of utilizing distant super star clusters (SSCs) in which the stellar population becomes an unresolved point source. Theoretical predictions by Gazak et al. (2013) show that in young SSCs the RSG population dominates the near-infrared flux. In this case the metallicity of the cluster could be extracted by studying the entire cluster as a single RSG. In order to accomplish these goals we investigate the galactic population of RSGs in the h and χ Persei double cluster (henceforth Perseus OB-1) by performing quantitative spectroscopy on high resolution, high signal to noise ratio (SNR) spectra collected using the Subaru Telescope atop Mauna Kea. The presence of a large population of supergiant stars limits the age of Perseus OB-1 to tens of millions of years, and offers a laboratory for the full range of stellar astrophysics–from IMF to post-main sequence stellar evolution. Currie et al. (2010) present a careful photometric and spectroscopic study of the double cluster and refine the physical parameters of this system. They find an age of 14±1 Myr and estimate a minimum total stellar mass of 20,000 $M_{\odot}$. Solar metallicity is a sensible assumption for such a young population in the Milky Way solar neighborhood, and studies of the B and A population of supergiant and giant stars−while incomplete−find solar or slightly sub-solar abundances. Our high resolution spectra of eleven RSGs in Perseus OB-1 provide an ideal dataset for testing multiple aspects of this project. We will discuss the major scientific

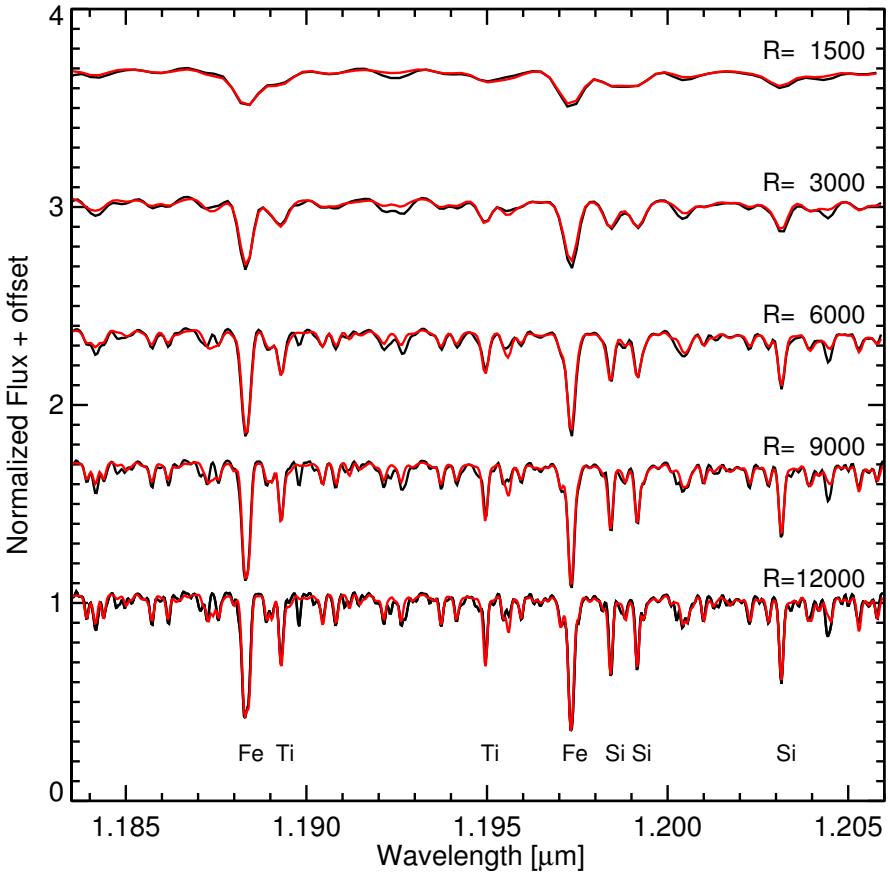

Figure 2.1 J–band spectrum of the RSG BD+56 595 in Perseus OB-1. The original effective resolution is R=12000. To investigate the effects of spectral resolution we also degrade the spectrum by a gaussian convolution. For each resolution the best fitting model spectrum is over plotted in red. As shown later, stellar metallicity and temperature are unaffected down to R∼3000.

results and implications of our work on h and χ Persei in Chapter 3. We will show that careful application of the MARCS model atmospheres returns measurements of Z consistent with solar metallicity. Using two grids of synthetic spectra−one in pure LTE and one with NLTE calculations for the most important diagnostic lines−we measure Z = +0.04 ± 0.10 (LTE) and Z = −0.04 ± 0.08 (NLTE) for the sample of eleven RSGs in the cluster.

In this chapter we develop and test the J–band technique using the observed spectra, which will be discussed in more detail in Chapter 3. In Figure 2.1 we plot the J–band spectrum of one single object. Since we will investigate the impact of spectral resolution on the accuracy of

Table 2.1. The MARCS Model Grid

Parameter	Notation	Min	Max	Spacing
Eff. Temperature [K]	T_{eff}	3400	4000	100
		4000	4400	200
Log gravity	$\log g$	-0.5	$+1.0$	0.5
Metallicity [dex]	Z	-1.00	$+1.00$	0.25
Microturbulence [km/s]	ξ	1.0	6.0	1.0

Note. — Parameter grid for MARCS atmospheres (and synthetic spectra) utilized in this work.

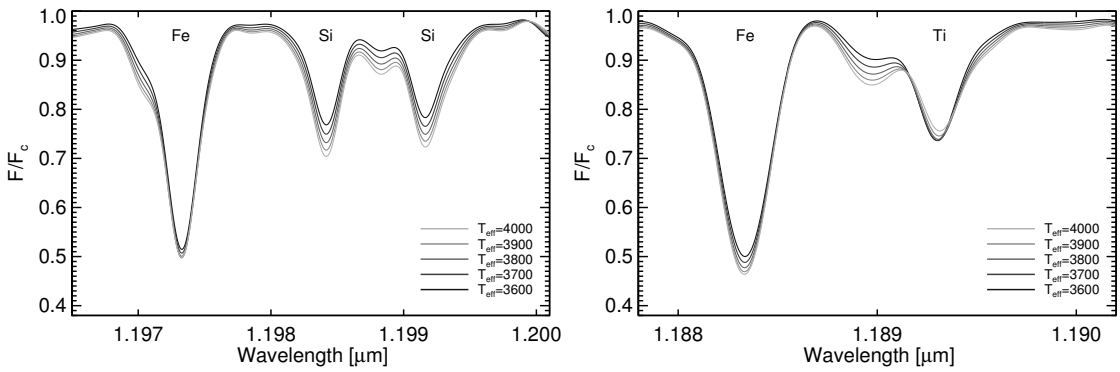

Figure 2.2 The effects of T_{eff} (see Table 2.1 on synthetic lines of diagnostic atomic features. Left panel: iron and silicon. Right panel: iron and titanium. Note the stronger response of silicon to T_{eff}.

stellar metallicity determination, we also show plots where we have degraded the resolution through gaussian convolution. The full spectral library appears in Chapter 3.

2.1 Atmospheric Models and Synthetic Spectra

For the analysis of RSGs in our sample we utilize two grids of synthetic spectra calculated using LTE and NLTE radiative transfer. Both grids of model spectra are calculated using as input an underlying grid of MARCS model atmospheres (Gustafsson et al. 2008). These atmospheric models are calculated in 1D LTE and, while not as complex as state-of-the-art 3D models, are well suited

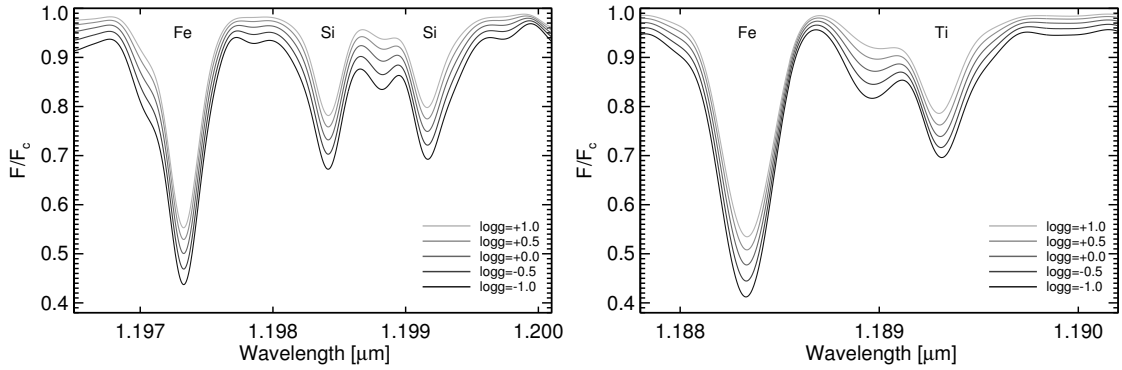

Figure 2.3 The effects of log$g$ (see Table 2.1 on synthetic lines of diagnostic atomic features. Left panel: iron and silicon. Right panel: iron and titanium.

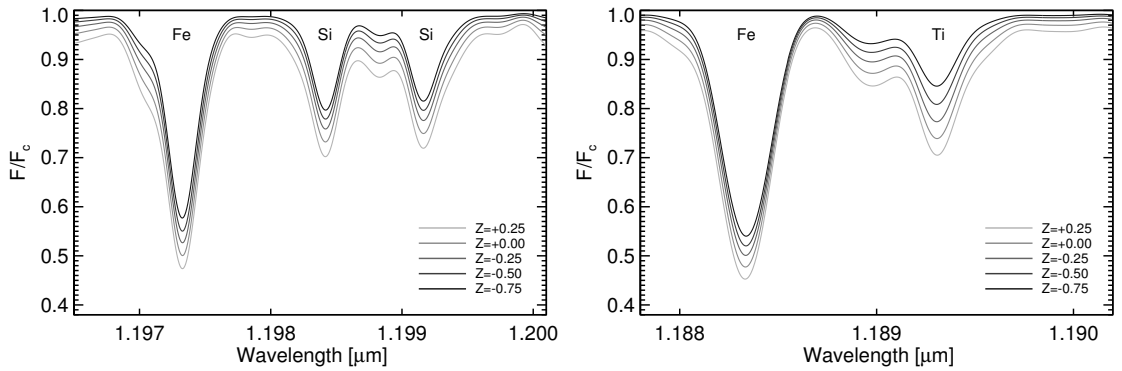

Figure 2.4 The effects of metallicity (Z) (see Table 2.1 on synthetic lines of diagnostic atomic features. Left panel: iron and silicon. Right panel: iron and titanium.

for this work. Notably, the MARCS model atmospheres have been well tested in the literature and converge quickly such that large grids are possible.

The MARCS grid used in this work covers a four dimensional parameter space including effective temperature, log gravity, metallicity on a logarithmic scale (normalized to Solar values), and microturbulence ($T_{\rm eff}$, log$g$, Z, ξ). The dimensions of this grid can be found in Table 2.1.

The grids of synthetic model spectra used in the analysis of this paper are calculated in first in LTE using TURBOSPECTRUM (Alvarez & Plez 1998; Plez 2012), and second with NLTE diagnostic lines (iron, titanium, and silicon) using the codes developed in Bergemann, Kudritzki et. al (2012, 2013).See Figure 3.3 for a visualization of the effects of the NLTE corrections.

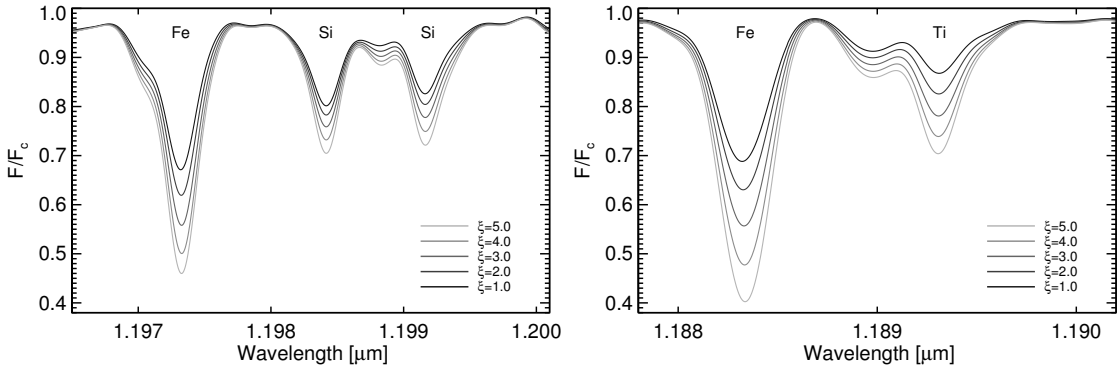

Figure 2.5 The effects of microturbulence (ξ) (see Table 2.1 on synthetic lines of diagnostic atomic features. Left panel: iron and silicon. Right panel: iron and titanium.

2.2 Continuum Fitting

The first step in any comparison between an observed spectrum (F_{obs}) and synthetic (F_{mod}) is to correct the flux scaling of one spectrum to the other. There are countless methodologies to accomplish this task and we have developed an optimal process for the J–band method which functions well at the great variety of spectral resolutions to which the method can be applied.

2.2.1 General Considerations

RSGs present absorption line spectra and thus the best approximation of the continuum will always be the spectral points with the highest flux levels. Still, it is important to note that the selection of continuum points must be completed on the model spectrum, not on the data. This is because the data is a "perfect spectrum" combined with various noise spectra. Even in the case of white, gaussian noise, the highest flux points in an observed spectrum will correlate to the continuum plus the upper tail of that gaussian noise.

$$F_{obs} = F_{source} + \sigma_{white} + \text{Reduction Noise} \tag{2.2.1}$$

A visualization of this is provided in Figure 2.6; here we demonstrate the difference between picking the highest 20% of the flux points in the data (left panel) to the continuum correction

method we apply (right panel). These plots consider a flat model of flux = 1.0 and three instances of "noisy" data (gaussian scatter of SNR = 100) with a flux offset (top), a linear trend (middle), and a nonlinear trend caused by, for example, sub par flat fielding (bottom) in the "data" of flux equal to unity.

At high resolutions it is straightforward to scale a model to the continuum level of the data. This is accomplished by selecting regions of the spectrum with flux of F_{mod} = unity, performing a polynomial fit to the ratio of those points to the matching F_{obs} as a function of wavelength, and then dividing the full wavelength range of the model by this derived fit. In this way we are comparing the depth and shape of spectral features between the observed spectrum and model.

2.2.2 Fitting the "Pseudocontinuum"

At lower resolutions the effort to correct the continuum increases in complexity as the dense forest of weak molecular lines blend together to form a "pseudocontinuum" such that the entire observation lies below the true continuum. We illustrate this effect in Figure 2.7 for Z= −1.0, 0.0, +0.5, and +1.0 at a spectral resolution of 3000. It is not possible to know a priori how to then properly correct for the continuum as depth below the true continuum is a function of the stellar parameters themselves, especially metallicity, the primary target of our work.

Our fitting method then becomes a measurement of the ratio of line depth to pseudocontinuum level. When applied uniformly to the observed and synthetic spectrum, the detrimental effects of low resolution are mitigated with no need for assumptions of the true continuum level.

2.2.3 Continuum Fitting Algorithm

In lower resolution cases, even selecting a top percentage of the model can improperly sample the spectrum, leaving gaps in wavelength where the pseudocontinuum is not sampled. This may result in continuum artifacts and introduce spurious signals into goodness of fit measurements. We demonstrate this wavelength sampling issue in Figure 2.6.

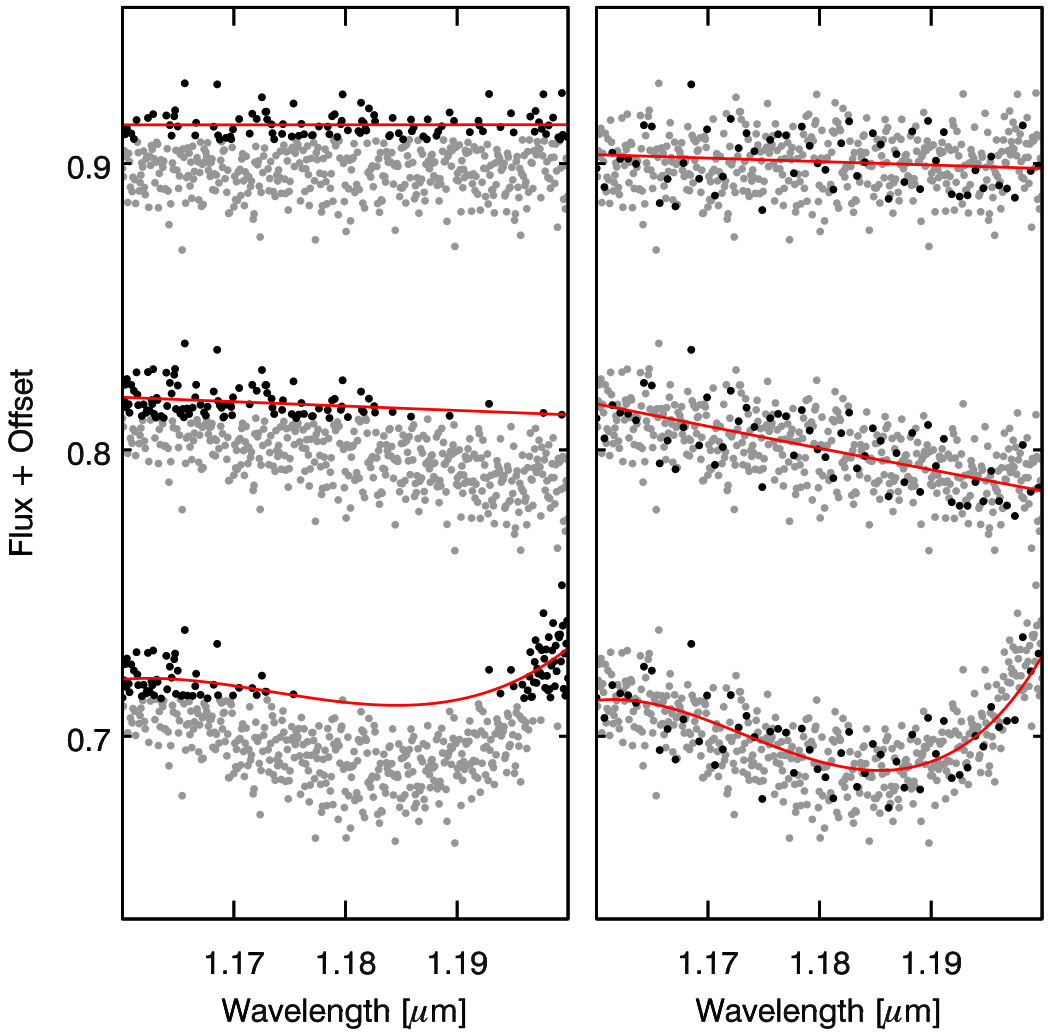

Figure 2.6 The effects of improper continuum fitting. Each panel shows three gaussian "continuum" spectra plotted as dots. Black dots are selected for the continuum fit while gray ones are ignored. Each spectrum has a different underlying trend (see text in §2.2.1). In the left panel we show the possible effects of selecting based only on the flux level of the data, notably the selection of the upper tail of the noise. In the right we apply our methodology by selecting points in the model (see §2.2.3). The method then selects a proper random sampling of the noise in the data and reproduces a scaling relationship far more effectively.

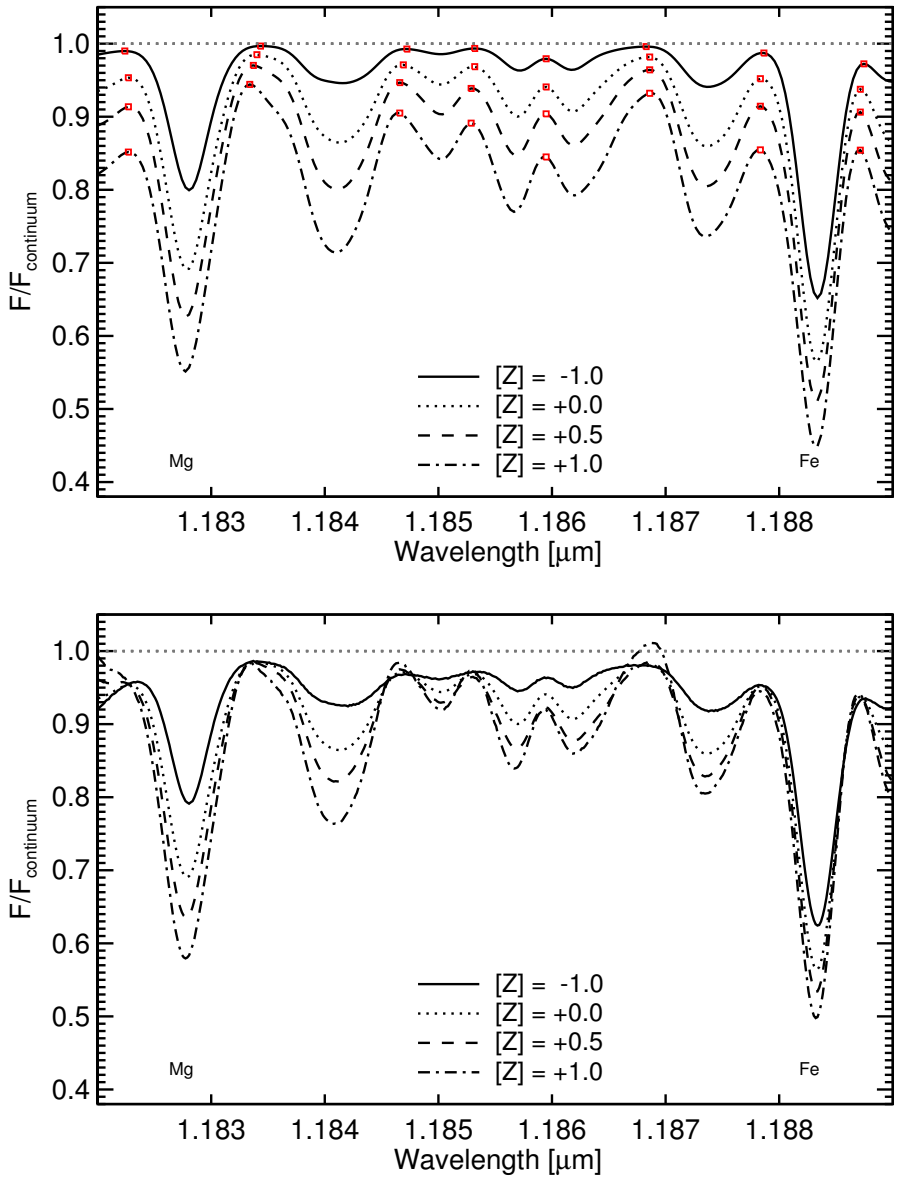

Figure 2.7 Plot of continuum region between two strong atomic features at spectral resolution of 3000. Each model has $T_{\rm eff}$=4000 log$g$=0.0, and ξ = 4.0. Top panel: models at four values of Z to demonstrate the pseudocontinuum. Red squares mark the continuum points used for each model. Bottom panel: each model is scaled to that of Z=0.0 assuming that it resembles the data set. The variable depth of atomic spectral features as a function of metallicity is still clearly seen. In addition, weak line features strengthen with metallicity and provide additional information with increasing metallicity.

We begin by defining a characteristic "continuum width",

$$CW = \lambda \times \frac{S}{R}, \tag{2.2.2}$$

where the inverse of spectral resolution R is scaled by a factor S to define the characteristic width in which we expect to find a spectral line and continuum point. The input model is sliced into segments of CW microns and the location of the maximum F_{mod} in each slice is recorded as the first-pass continuum, C_1. We experimented with a range of values in S and found that the ideal value is between 0.5 to 1.0, allowing for a perfect sampling of the pseudocontinuum maxima in a spectrum with equally spaced lines of width defined by spectral resolution R.

The dense spectra of RSGs are far from such an ideal. As a result, C_1 will contain multiple "edge maxima", where an entire CW slice lies within a spectral feature (a blend or extremely strong line) and the continuum point in that slice is, in reality, deep beneath the pseudocontinuum. We execute a second-pass filter to remove such cases. This is done by calculating the variance within the flux of the C_1 values and removing outliers,

$$C_2 = |F_{mod}(C_1) - \widetilde{F_{mod}(C_1)}| \leq 3\sigma \tag{2.2.3}$$

where σ is the standard deviation in the model flux at the C_1 continuum points. In this way, C_2 contains only the pseudocontinuum points of the given model.

At this point the correction function can be calculated from the ratio of model and data flux at the values of C_2 continuum points, $F_{mod}(C_2)/F_{obs}(C_2)$ as a function of wavelength, $\lambda(C_2)$. We fit an initial smooth polynomial through these points. While the order of the polynomial is dependent on the calibration of the observed spectrum, we find that in general with properly reduced spectra, a polynomial of order 3 is entirely adequate. In cases where an observed spectrum might contain a higher order continuum variation due to, say, a smooth variation in the flat field, the order of the polynomial fit may need to be increased or replaced with a different function entirely.

After the initial fit we complete an additional filtering to remove outlier point in the observed spectrum. Such outliers may be due to low fidelity telluric correction, spectral features present

in the observations but not models, or fake emission or absorption spikes due to data reduction in the presence of cosmic rays or instrument defects. This filtering is completed much like in Equation 2.2.3, except the variable of interest becomes the residuals of the initial continuum fit,

$$\text{residuals} = f_{cont}(C_2) - F_{mod}(C_2)/F_{obs}(C_2). \tag{2.2.4}$$

we again consider any points beyond three sigma of the residual distribution to be outliers, remove them, and fit a final continuum correction function through the resulting set of flux ratios of the final set of continuum points. This function is then applied to the full model spectrum to scale it to the level of the observation.

In the lower panel of Figure 2.7 we correct each model to the solar metallicity model to demonstrate that the models are not degenerate; they remain unique with respect to metallicity even at resolutions suffering the effects of the pseudocontinuum.

2.3 Data Resolution and Macroturbulence

While a spectrograph disperses incident flux at a characteristic resolution based on grating and slit width, the width of spectral features, or "effective" spectral resolution can vary significantly from these expected values based on the size of large-scale turbulent motions, terrestrial atmospheric conditions (e.g. seeing, especially in the case where a point spread function is narrower than the slit width of a spectrograph), and instrument setup (e.g. the focus of the telescope). For these reasons an independent measurement of spectral resolution is an important component in any quantitative spectroscopy. We find variations in effective spectral resolution even in spectra collected under ideal conditions. Any spectroscopic technique not measuring the effective resolution of the observed spectra is at risk of significant, unpredictable systematics.

We note that even for a method utilizing equivalent widths (EWs), spectral resolution is critical for the dense spectra of RSGs. With any significant change in spectral resolution (Figures 1.4, 2.8), two issues will influence measured EWs. The first is the level of the pseudocontinuum, discussed in §2.2. The level of that pseudocontinuum is strongly dependent on the spectral resolution and, since

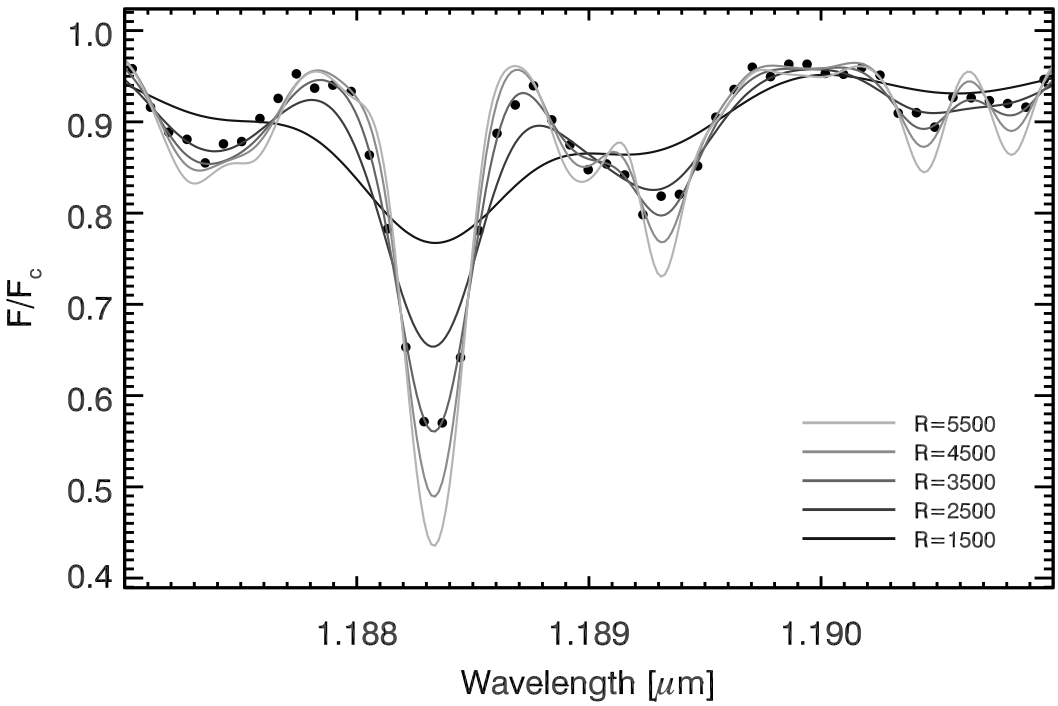

Figure 2.8 The importance of fitting for proper model resolution. A model spectrum degraded to R = 3500 and with gaussian scatter added is plotted as black points. The same model is over plotted in a range of R $\pm$ 2000 are plotted to demonstrate the significant effect of spectral resolution. Assuming the correct resolution for the model spectra is crucial. The application of incorrect spectral resolution to the dataset can potentially introduces severe systematic effects.

the true continuum of the data is unknown, that effect influences the EWs. Second, as resolution drops and the pseudocontinuum develops, not only is the continuum measurement critical, but so too does flux from neighboring lines "leak" into the diagnostic feature being measured. Since the amount of flux in those lines is dependent on fit parameters and the level of contamination is determined by spectral resolution, it is important to measure this value.

To accomplish this, we first fit a spectrum to the full model grid leaving resolution as a free parameter. Each model is degraded to a set of resolutions ranging from twice the expected spectral resolution and down until a χ^2 minimum is passed. We fit a parabola through χ^2 vs resolution. The minimum of this fit is adopted as the best fit resolution for that model. Upon completion we have a four dimensional χ^2 grid in which resolution is not constant. We adopt the model with the lowest overall χ^2 as the "best model" and the paired spectral resolution as the proper value for the observed data. At this point we refit the full grid of models locking each at the measured best spectral resolution to calculate a uniform grid of χ^2 values for parameter determination.

2.4 Determination of Stellar Parameters and their Significance

In this work we utilize χ^2 as a measure of goodness of fit, such that

$$\chi^2 = \sum_{i=1}^{N} \frac{(F_i - M_i)^2}{\sigma_i^2} \tag{2.4.1}$$

where F represents the observed spectrum with an associated error spectrum σ and M is a given synthetic model. The χ^2-statistic is then a sum of the squared residual spectrum weighted by per pixel uncertainties. This is an entirely reasonable way to compare a given set of models to an observed spectrum, and we use it to find the best fitting model in our four dimensional grid of synthetic spectra (Table 2.1).

After calculating a full four dimensional grid of χ^2 values we extract the best fit parameters. The methodology is as follows. We begin by selecting the "best" model−the model with the lowest χ^2 value. We use the parameters of this model to inform the selection of six two dimensional χ^2 planes (see Figure 2.10). Functionally, two parameters are locked at the "best values" for each

plane and the remaining two parameters are varied against each other. We interpolate the χ^2 grid of each plane onto a parameter grid four times as dense and take the minimum of the dense grid as the best fit values for the two free parameters. After completing this procedure for each of the six planes, we have three measured best values for each parameter. We average these values to arrive at a final fit for each parameter.

Standard χ^2 statistics requires that the deviations between data and model in each wavelength bin be gaussian in nature. However, gaussian deviates cannot be assumed for the following reasons: the models are likely to contain systematic errors; for example, residual features due to imperfect telluric corrections are not randomly normal across the spectrum. While a visualization of the residuals between model and data tend to be obviously non-gaussian, this idea can be mathematically tested by Fourier analysis. In the case of a set of pure gaussian deviates vs. wavelength, one will find no structure in the power density spectrum (PDS = $\log(\mathrm{fft}(\mathrm{residuals}))^2$, where fft is a fast Fourier transform). This is because each point is independent from every other one. In such a case, which we visualize in the top panel of Figure 2.9, the application of the χ^2 statistical distribution is warranted. As one moves away from the best fit model in parameter space, the increases in χ^2 are due only to the difference between the model and the data. In order to demonstrate a case where this is not true, we use the same gaussian noise in the top panel of Fig. 2.9 and smooth it by a boxcar function of fifteen pixels in width. We plot this noise in the center panel. The effect is to introduce spectral correlation in the noise. When we repeat the Fourier analysis, the PDS now contains structure attributed to that correlation. In the lower panel of Fig. 2.9 we plot actual "best fit" residuals between model and RSG spectrum. The evidence of correlation and structure in the residuals is obvious in the PDS and thus we cannot properly apply the χ^2 distribution to estimate parameter uncertainties.

We instead assess the significance of our parameter fits with a monte carlo simulation. We begin by constructing a spectrum at the exact extracted parameters by linearly interpolating between points in the model grid. For each of 1000 trials we add random gaussian noise of strength characteristic of the signal to noise of the measured spectrum. We fit each noisy interpolated model as described in this section. For each trial we determine the fit parameters and, after completing

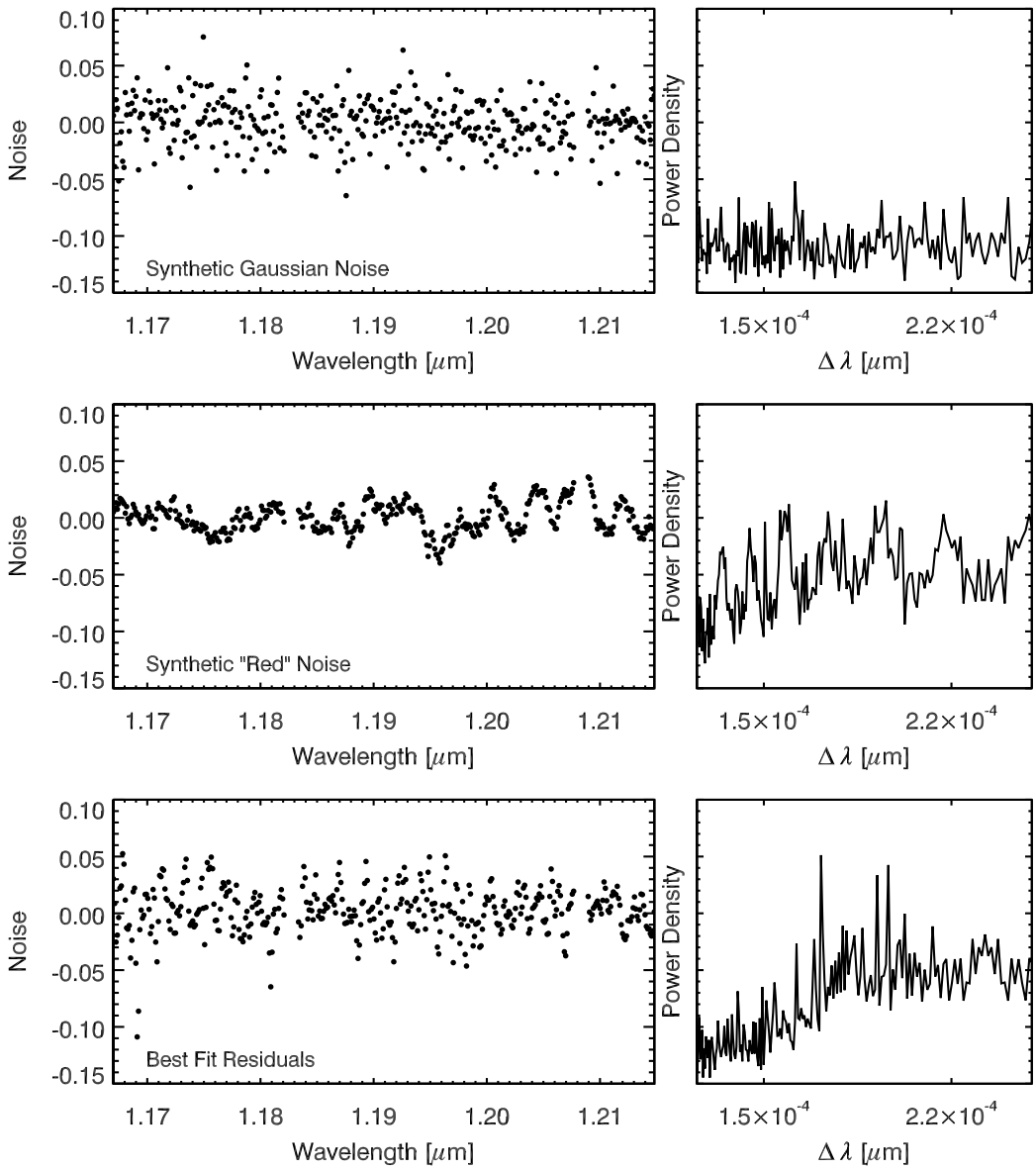

Figure 2.9 The non-Gaussian noise signature of the residuals (observed spectrum − model) of J–band RSG spectra. Top panel: simulated gaussian residuals on the left and the power density spectrum (PDS = $\log(\mathrm{fft(noise)})^2$, where fft = fast fourier transform). Note the flat PDS which signifies that no "information" remains in the noise. Center panel: Simulated red noise residuals (gaussian noise smoothed by a boxcar function over ten pixels to introduce spectral correlation), and the related PDS. Lower panel: Residuals from an actual observation with the best fitting model subtracted. Structure in the PDS of the red noise and the data offer evidence that the residuals are non-gaussian.

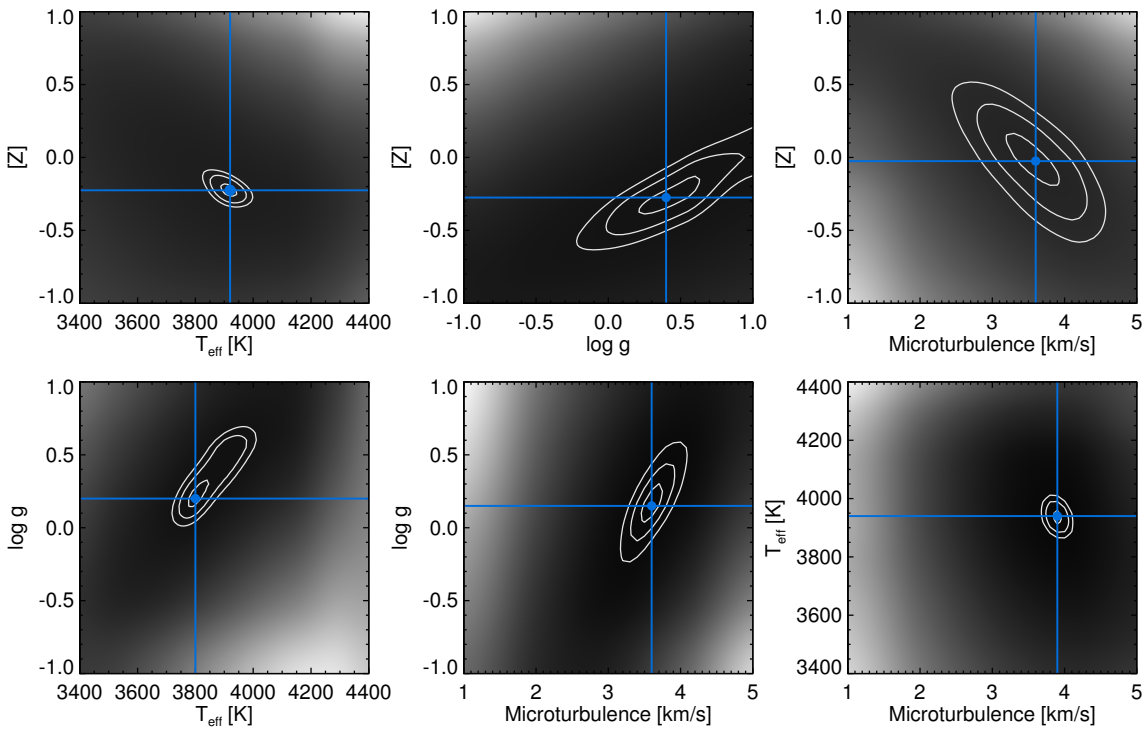

Figure 2.10 2D contour plots used to extract fit parameters in the analysis procedure. The smooth color gradient is an interpolated χ^2 map, with dark representing lower values (better fits). White contour lines depict fit areas of 1, 2, and 3 σ as determined by monte carlo sampling. The blue point at the intersection of blue lines shows the minimum χ^2 in each 2D slice.

the computations, analyze the distributions of fitted values for each parameter. In each parameter the zone of $\pm 1\sigma$ is contained between the 15.9 and 84.1 percentile levels. This technique accounts for the noise level in our data as well as any effects based on the spacing in our model grid. We adopt a minimum 1σ value of 20% of the grid spacing for each parameter as we consider a fit more precise than that to be unrealistic given the possibility of nonlinear behavior between grid points. In general our measured significance in metallicity lies above this minimum σ value such that we may confidently trust that our grid is fine enough in metallicity space for this work. In this work we find that lines of Mg I are never well fit. We know from work in progress (Bergemann, Kudritzki, et al. 2014) that the reason is the influence of NLTE effects, which are not yet included for Mg I. For this analysis we mask out lines of Mg I before calculating χ^2 (see §2.7).

2.5 Parameter Stability vs. Spectral Resolution

The power of the methodology presented in DFK10 is the need for only moderate resolution spectral data. Our high resolution spectral catalogue allows for the first systematic tests of the resolution limits of the J–band technique. In the following tests we degrade the resolution of our observed spectra and those spectra become the inputs to our fitting procedure. To achieve this degradation we convolve the high resolution observed spectrum with a gaussian with characteristic width of FWHM $= \sqrt{(\lambda/\mathrm{R})^2 - (\lambda/\mathrm{R_{data}})^2}$, where R represents the output resolution of the "new" spectra. For this experiment we maintain a constant signal to noise ratio of SNR=100 by adding noise at each new resolution.

We then follow identically the techniques presented in this chapter, treating each degraded spectra as an independent observation. We iterate from R of 10,000 to 2,000 in steps of 1,000. At each resolution we calculate the average and standard deviation of measured metallicity for the eleven objects. These values have been plotted in Figure 2.11. We find that the fitted average metallicity remains stable for both LTE and nLTE grids from spectral resolutions of 12,000 through 2,000. Furthermore, the standard deviation in the individual metallicity measurements holds stable at $\sim$0.12 dex down to R=3000. At this point individual atomic spectral features become too blended and diluted; the parameter fits of individual objects begin to diverge from high resolution fit values.

We conclude from these tests that the J–band technique can be utilized on RSGs down to spectral resolutions of 3000. To study large populations of RSGs at extragalactic distances, then, one needs a multi object spectrograph operating at R$\geq$3000 on a telescope with enough collecting area so that the limiting magnitude is fainter than the target RSGs. Two such instruments exist: MOSFIRE on Keck operates at R$\sim$3200 and KMOS on the VLT operates at R$\sim$3400. These ideal instruments for the study of extragalactic populations of RSGs operate near but safely above the resolution limits of our technique.

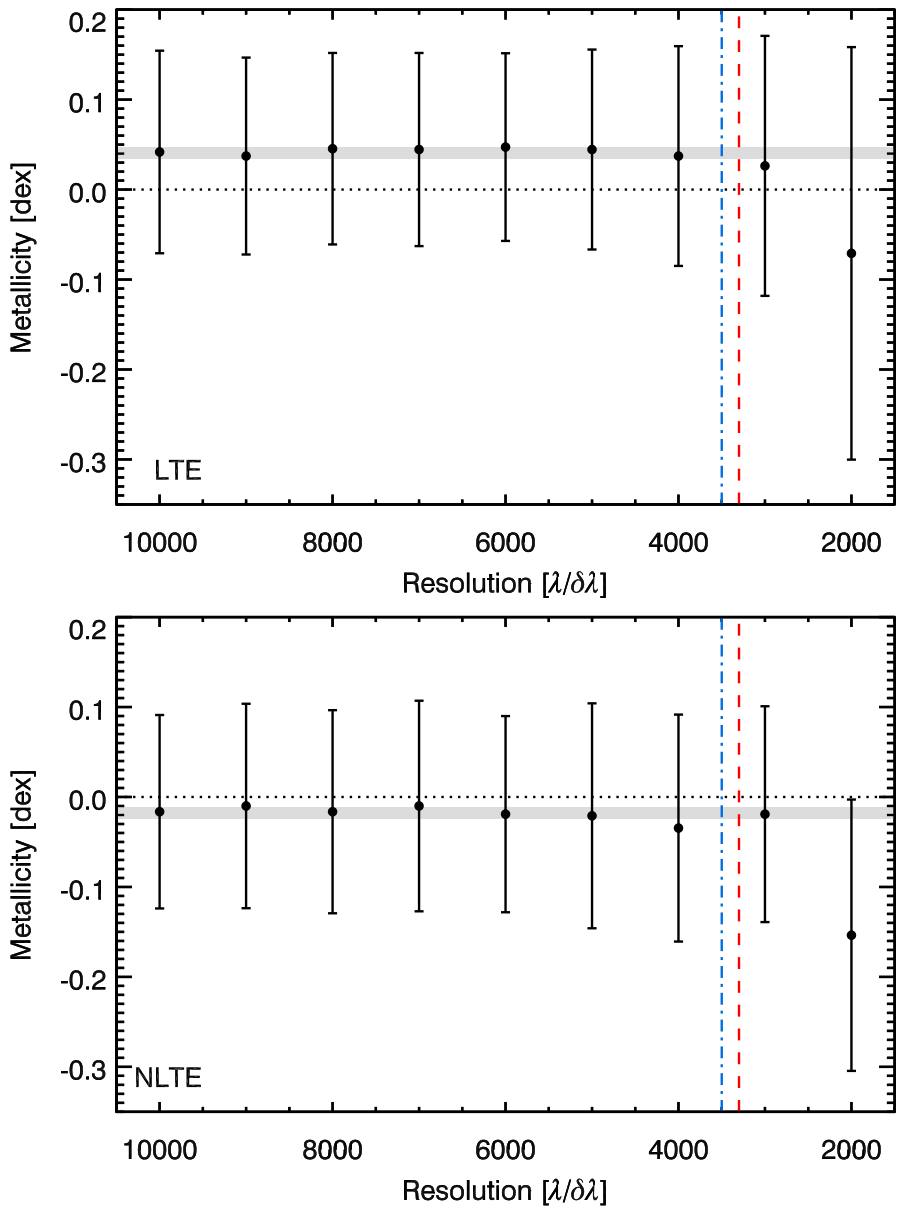

Figure 2.11 Change in the average measured metallicity for our sample of Perseus OB-1 stars as a function of spectral resolution. Error bars mark the standard deviation of the individual eleven measurements at each step. The horizontal gray region shows $\pm 1\sigma$ of the average metallicity between $12000 \leq R \leq 3000$, demonstrating the stability of the technique down to resolutions of R=3000. Vertical lines mark the spectral resolutions of key J–band spectrographs, KMOS on VLT in dash-dotted blue and MOSFIRE on Keck in dashed red. A horizontal dotted line marks solar metallicity. We plot results from the LTE model grid (upper panel) and NLTE grid (lower panel). The signal to noise for each spectra is kept constant by the addition of monte carlo noise at each resolution step.

2.6 Parameter Stability vs. Signal to Noise

In our tests for parameter stability as a function of spectral resolution we assume that at each resolution step we have the same signal to noise ratio (SNR) as in the original, high resolution spectrum. This value of SNR is $\approx$ 100-150 per object. By reducing the spectral resolution we functionally increase the SNR per resolution element. In the following, we devise a test to measure the minimum SNR as a function of resolution for which we obtain the same accuracy with respect to metallicity as for our high resolution case.

We calculate the SNR for our original spectra, $\mathrm{SNR_{meas}}$ as follows:

$$\mathrm{SNR_{meas}} = \left[\frac{1}{\mathrm{N}}\sum_{\mathrm{i=1}}^{\mathrm{N}}(\mathrm{F_i} - \mathrm{M_i})^2\right]^{-\frac{1}{2}} \tag{2.6.1}$$

In Equation 2.6.1, F is the input spectrum with N points and M is the model in the grid which returns the lowest χ^2. To measure the required SNR at each resolution we must adjust the effective SNR of the observed spectrum to any $\mathrm{SNR_{target}}$ less than $\mathrm{SNR_{meas}}$. This is accomplished by noting that the target SNR is just a quadrature sum of $\mathrm{SNR_{meas}}$ and the additional noise spectrum required. The strength of that gaussian noise, σ_{scale} is then

$$\sigma_{\mathrm{scale}} = \sqrt{\mathrm{SNR_{target}^{-2}} - \mathrm{SNR_{meas}^{-2}}} \tag{2.6.2}$$

Adding random gaussian noise scaled by σ_{scale} to our observed spectrum degrades it to $\mathrm{SNR_{target}}$.

To understand the SNR necessary to reach our target precision of $\sigma_{\mathrm{Z}} \approx 0.10$ we use the above method starting with a modest $\mathrm{SNR_{target}}$=5 and iteratively increase that value until the σ_{Z} we extract are consistent with those measured for the original spectrum, i.e., any additional SNR provides no increase in fit precision given the data and model grid. The results of this test are plotted in Figure 2.12, and indicate that for instruments operating at resolutions of $\sim$3000, a SNR of $\sim$100 per resolution element is an ideal target for observational programs.

As with our discussion in §2.4, we note that the residuals between data and model will not be purely gaussian in nature. This can be due to any combination of telluric contamination, detector

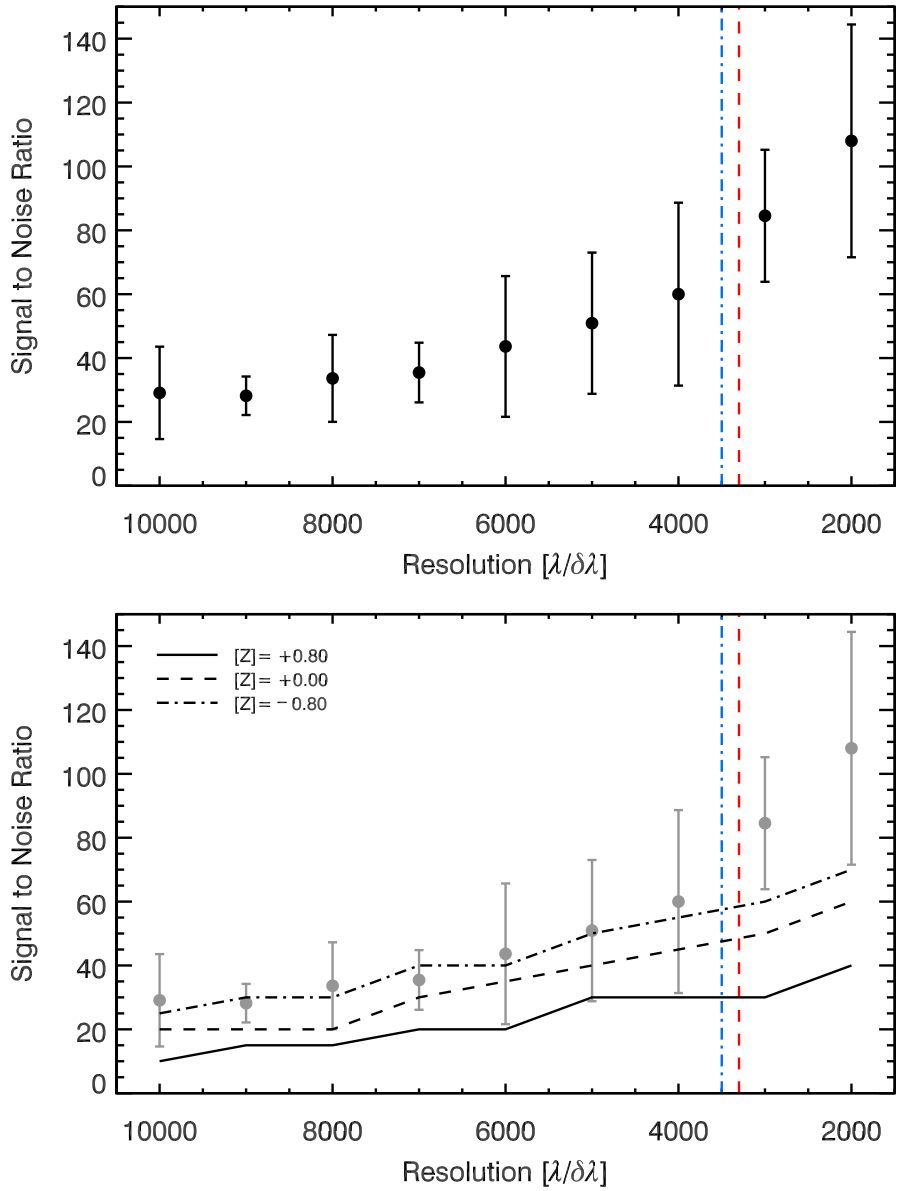

Figure 2.12 Signal to noise ratio needed to achieve target precision for measurement of Z as a function of spectral resolution. Upper Panel: Each point is the average and standard deviation of the necessary signal to noise ratio for the set of eleven RSG spectra. Lower Panel: Results for data are grayed out for comparison. Overplotted are signal to noise predictions for models interpolated from the MARCS NLTE grid for metallicities of +0.8 (solid), 0.0 (dashed), and −0.8 (dash-dotted). Vertical lines mark the spectral resolutions of key J–band spectrographs, KMOS on VLT in dash-dotted blue and MOSFIRE on Keck in dashed red. For a description of the technique, see §2.6.

noise, and imperfect model atmospheres. The $\chi^2_{\rm data}$ spectrum will contain larger sporadic deviations due to those effects. As a result, the $\rm SNR_{meas}$ of Equation 2.6.1 will slightly underestimate the actual SNR of the data. When this propagates into Equation 2.6.2, we end up adding too little noise and not quite reaching $\rm SNR_{target}$. This means that the curve in Figure 2.12 may be skewed downwards. The amplitude of this effect will vary due to the specifics of each observation. This likely accounts for the scatter present in Figure 2.12. The overall shift must be small due to the quality of our data and spectral fits. Still, we recommend using the upper limits of the error bars in Figure 2.12 as a target SNR when planning observations.

We perform a final experiment to test the effects of metallicity on SNR requirements. We interpolate three models from our NLTE grid to values between grid points (Z= +0.8, 0.0, and −0.8) and reanalyze each model as described earlier in this section. The results are plotted in the lower panel of Figure 2.12. A trend of increasing SNR requirements with decreasing metallicity is indeed seen. The effect is not overwhelming, with less than a factor of two difference between models at Z=−0.8 and +0.8. The SNR required for this set of spectra are globally lower than the case of the actual data. This is to be expected as the experiment is performed starting with perfect models which show no contamination from non-gaussian noise sources.

2.7 Spectral Window and Exclusions

2.7.1 Missing Theoretical Lines

In general, we find that the best fits are returned by considering the strongest diagnostic features as well as a sample of the pseudocontinuum between the wavelength range of 1.165-1.215 μm. In this spectral window we find that two spectral lines present in the data are absent in the theoretical spectra. An example of this is presented in Figure 2.13. While the detrimental effects of this are limited at high resolution, as we begin to drop the resolution those features blend into the pseudocontinuum and cause the fit in that wavelength regime to be too shallow. For this reason that spectral window is always blocked out.

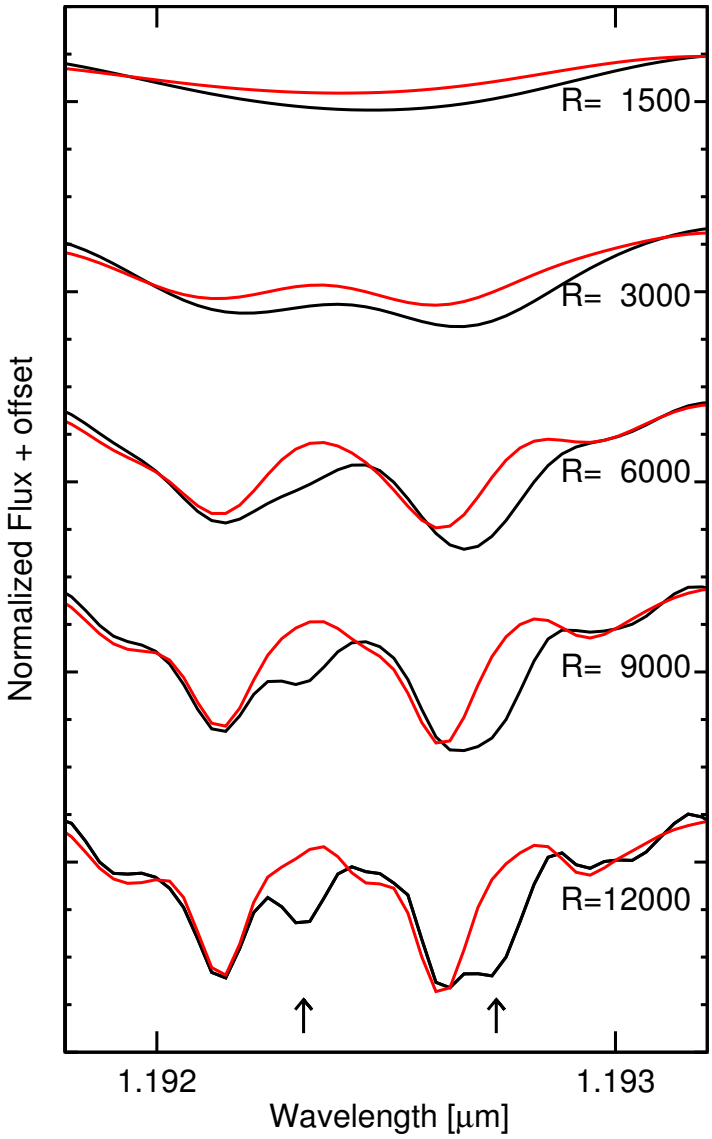

Figure 2.13 A narrow spectral range of one of the Perseus OB-1 spectra showing two missing lines (noted by black arrows) in the theoretical (red) spectrum. At high resolution the effect is minimal as the lines appear in no models, but at low resolution the missing features blend with modeled lines and the effect is to demand higher metallicity to deepen the calculated lines. For this reason this spectral region is not fit in our procedure.

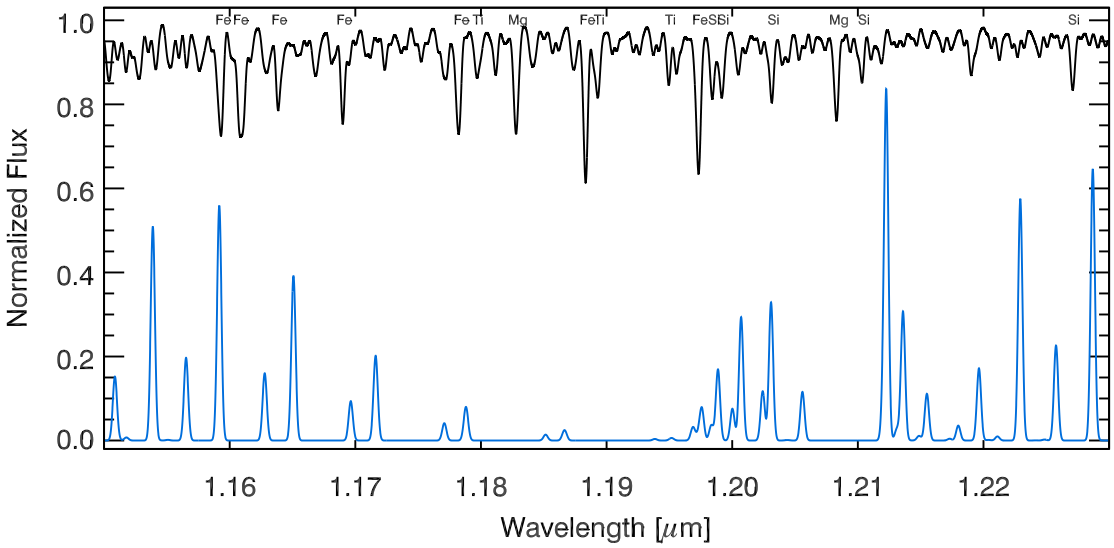

Figure 2.14 Sky emission in the J–band due to OH in the Earth's atmosphere. Contaminative spectrum is plotted in blue while an example model is over plotted in black. Both spectra are at the optimal resolution of KMOS, with R$\sim$3500.

2.7.2 Magnesium

As discussed in §2.4 the magnesium lines are strongly affected by NLTE effects which are not yet included for the diagnostic lines in our model grid. NLTE work on J–band lines of Mg I is nearing completion (Bergemann, Kudritzki, et al. 2014). For now, though, the spectral windows including magnesium are also ignored.

2.7.3 Night Sky Emission and Telluric Absorption

Near-IR spectroscopy from the ground is, even in the best conditions, an observational challenge. The night sky is both an emitter and absorber in the near-IR and without proper correction these features can dominate the already complex spectrum of a RSG. Night sky emission lines are due mainly to the OH collisional emission spectrum and is plotted in blue in Figure 2.14 with a normalized spectrum of a RSG plotted in black. Telluric absorption is a product of mainly water vapor, oxygen, and OH in the line of sight of the observations. An example telluric spectrum is

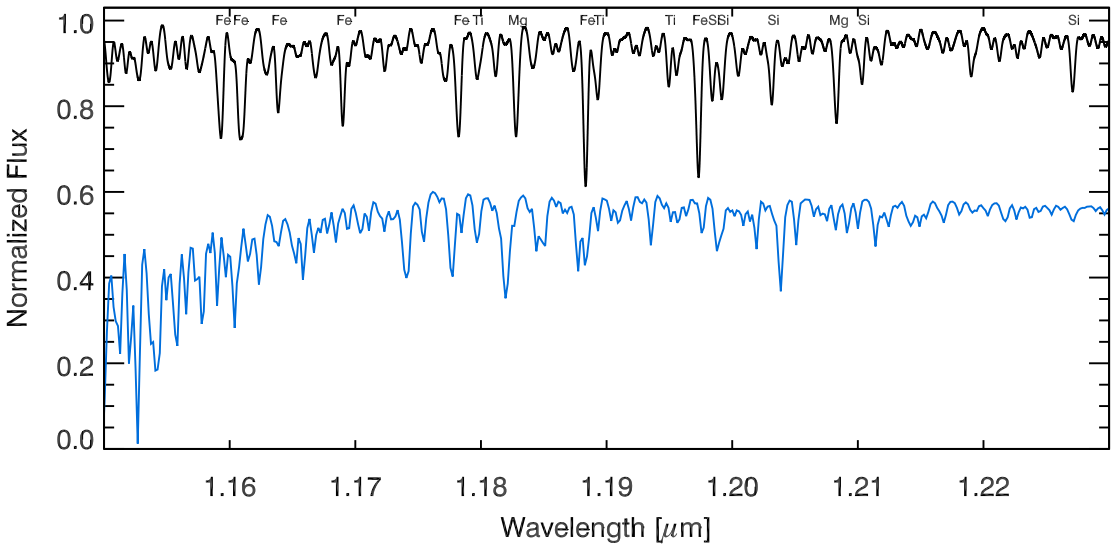

Figure 2.15 Telluric absorption spectrum in blue with a constant value of 0.4 subtracted for clarity. A RSG model spectrum is over plotted in black. Spectral resolution is R$\sim$3500.

plotted in blue in Figure 2.15 with a constant value of 0.4 subtracted with respect to the continuum value. Again, a RSG spectrum is over plotted in black for reference.

The contaminative effects of the night sky emission and telluric absorption are highly variable and require that a standard star be observed in close spatial and temporal proximity to the target source. In cases of stable, photometric weather, these conditions can be relaxed and the removal of spectral contamination can be done cleanly and without issue. For lower quality weather, these sources of spectral contamination become critical.

In cases where sufficient removal of absorption or emission features is not possible, we mask out the wavelength ranges which suffer from that contamination. This is dependent of the targets observed, as line of sight velocities will doppler shift the source wavelength and create contamination at different areas of the spectrum. Thus such masks are done on a case by case basis.

Chapter 3

Applications of the J–band Technique

3.1 The RSG population of the Galactic Cluster h and χ Persei

3.1.1 Motivation

As mentioned previously, the ideal target as a first test of the J–band method is a nearby coeval population of RSGs in the Galaxy, such that we may study the stars as individual objects and test the potential of utilizing distant super star clusters (SSCs) in which the stellar population becomes an unresolved point source.

In order to accomplish the goals set forth in Chapter 2 we investigated a population of RSGs in the galactic h and χ Persei double cluster (henceforth Perseus OB-1) by performing quantitative spectroscopy on high resolution, high precision spectra collected using the Subaru Telescope atop Mauna Kea. In this section we present the scientific results from this investigation.

3.1.2 Observations

On the nights of UT October 4 and 5 2011 we observed 11 of the 21 RSGs in the Perseus OB-1 cluster using the InfraRed Camera and Spectrograph (IRCS − Kobayashi et al. 2000) mounted on the Subaru telescope atop Mauna Kea. The observations took place in non-photometric weather with variable partial cloud cover. We operated to achieve maximum spectral resolution, using the $0''.14$ longslit in echelle mode with natural guide star adaptive optics.

Table 3.1. Catalog of Observed Perseus OB-1 Red Supergiants

Target	RA	DEC	m_V	m_J	m_H	SpT
BD+59 372	01 59 39.66	+60 15 01.9	9.30	5.33	4.20	K5-M0 I [a]
BD+56 595	02 23 11.03	+57 11 58.3	8.18	4.13	3.22	M1 I [a]
HD 14404	02 21 42.41	+57 51 46.1	7.84	3.56	2.68	M1Iab [b]
HD 14826	02 25 21.86	+57 26 14.1	8.24	3.47	2.47	M2 I [a]
HD 236979	02 38 25.42	+57 02 46.2	8.10	3.26	2.30	M2 I [a]
HD 13136	02 10 15.79	+56 33 32.7	7.75	3.00	2.14	M2 Iab [b]
HD 14270	02 20 29.00	+56 59 35.2	7.80	3.38	2.48	M2.5 Iab [b]
BD+56 724	02 50 37.89	+56 59 00.3	8.70	3.10	2.00	M3 Iab [b]
HD 14469	02 22 06.89	+56 36 14.9	7.55	2.82	1.93	M3-4 I [a]
BD+56 512	02 18 53.28	+57 25 16.8	9.20	3.68	2.68	M3 I [a]
HD 14488	02 22 24.30	+57 06 34.4	8.50	3.05	2.11	M4 I [a]

Note. — Target list for calibration of low resolution J–band RSG metallicity extraction. m_V values are adopted from Garmany & Stencel 1992, m_J and m_H from 2MASS (Skrutskie et al. 2006).

[a] Spectral type from Levesque et al. (2005).

[b] Spectral type from Garmany & Stencel (1992).

Spectra of targets and telluric standards were bias corrected, flat fielded, extracted and calibrated using standard packages in IRAF. Due to the variable cloud cover each frame was reduced individually and frames overwhelmed by noise were selectively removed. Absolute flux information cannot be recovered in such weather conditions so no flux calibrations were taken or used.

Observations in sub-optimal weather were possible due to the bright apparent magnitudes of the targets, but some spectra suffer from uncorrectable telluric contamination over certain wavelength ranges. For the analysis in this paper we have masked out those spectral regions.

A summary of the observed targets appears in Table 3.1, with a plot of the high resolution spectra in Figure 3.1 and a version with the spectra artificially degraded to resolutions of 3000 in Figure 3.2.

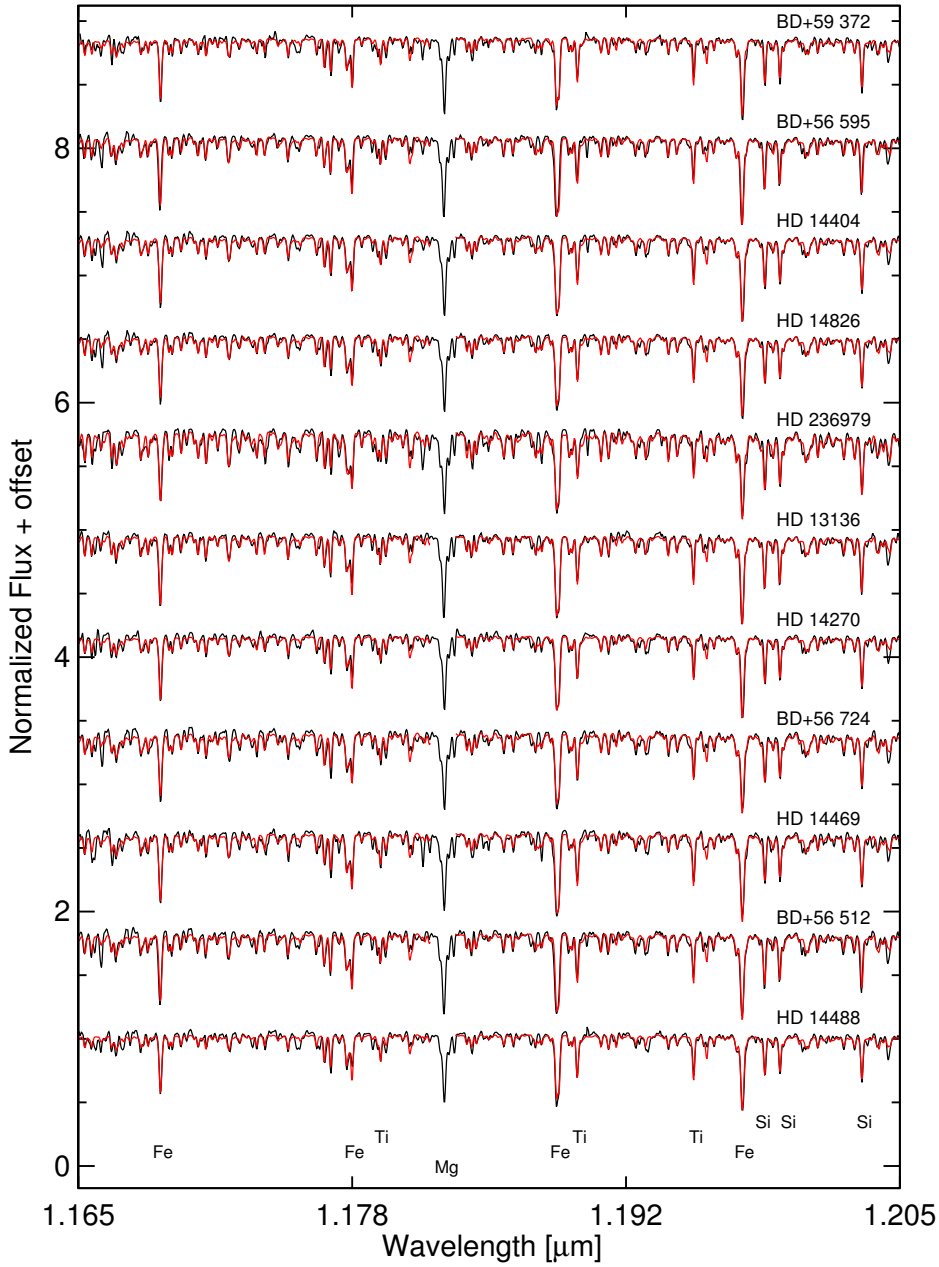

Figure 3.1 Spectral library of RSGs observed at high resolution with IRCS on Subaru. The main diagnostic atomic lines are labeled. Best fitting NLTE models are over plotted in red. The Mg I line is not included in the fit because it is calculated in LTE but subject to strong NLTE effects. NLTE calculations for Mg I will be implemented soon. Plots are arranged by spectral type (see Table 3.1).

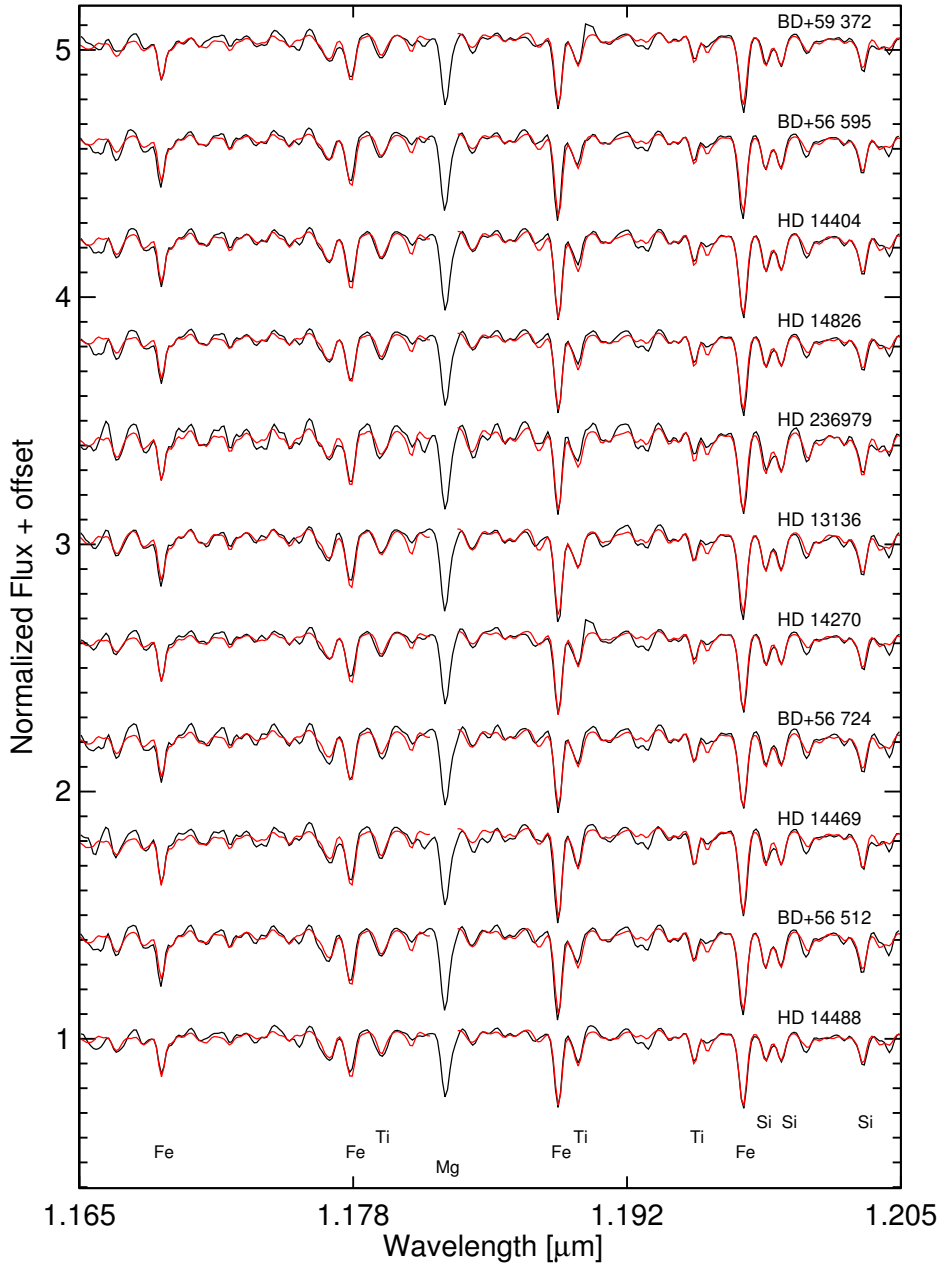

Figure 3.2 Spectral library from Figure 3.1 downgraded to a resolution of R=3000. The main diagnostic atomic lines are labeled. Best fitting NLTE models are over plotted in red. The Mg I line is not included in the fit because it is calculated in LTE but subject to strong NLTE effects. NLTE calculations for Mg I will be implemented soon. Plots are arranged by spectral type (see Table 3.1).

Table 3.2. NLTE Stellar Parameters of Perseus OB-1 Red Supergiants

Target	T_{eff} [K]	log$g$	Z [dex]	ξ [km/s]	$\frac{\lambda}{\delta\lambda}$ [a]	$M/M_\odot$	log $L/L_\odot$	Ev. log$g$	Lit.T_{eff} [b]
BD+59 372	3920 ± 25	+0.5 ± 0.3	−0.07 ± 0.09	3.2 ± 0.2	13600	9.86	4.21	+0.72	3825
BD+56 595	4060 ± 25	+0.2 ± 0.7	−0.15 ± 0.13	4.0 ± 0.2	11900	13.2	4.63	+0.43	3800
HD 14404	4010 ± 25	+0.2 ± 0.4	−0.07 ± 0.10	3.9 ± 0.2	11100	15.4	4.81	+0.24	···
HD 14826	3930 ± 26	+0.1 ± 0.2	−0.08 ± 0.07	3.7 ± 0.4	11200	15.7	5.03	+0.18	3625
HD 236979	4080 ± 25	−0.6 ± 0.3	−0.09 ± 0.09	3.1 ± 0.2	11700	16.5	4.89	+0.18	3700
HD 13136	4030 ± 25	+0.2 ± 0.4	−0.10 ± 0.08	4.1 ± 0.2	12300	17.7	4.95	+0.08	···
HD 14270	3900 ± 25	+0.3 ± 0.3	−0.04 ± 0.09	3.7 ± 0.3	11800	16.2	4.93	+0.14	···
BD+56 724	3840 ± 25	−0.4 ± 0.5	+0.08 ± 0.09	3.0 ± 0.2	10900	16.6	5.08	−0.05	···
HD 14469	3820 ± 25	−0.1 ± 0.4	−0.03 ± 0.12	4.0 ± 0.2	10200	17.6	5.13	−0.17	3575
BD+56 512	4090 ± 35	+0.4 ± 0.3	+0.01 ± 0.12	4.1 ± 0.2	11100	14.7	4.83	+0.31	3600
HD 14488	3690 ± 50	+0.0 ± 0.2	+0.12 ± 0.10	2.9 ± 0.2	10500	16.8	5.08	−0.07	3550

[a] Spectral resolution is measured to ± 100.

[b] Temperatures from Levesque et al. (2005) where target lists overlap.

Note. — Parameter fits to observed RSGs using the grid of synthetic spectra with NLTE corrections to Fe I, Ti I, and Si I lines (Bergemann et al. 2013, 2012). Masses and Evolutionary log$g$ are calculated using the Geneva stellar evolution tracks which include effects of rotation (Meynet & Maeder 2000).

Table 3.3. LTE Stellar Parameters of Perseus OB-1 Red Supergiants

Target	T_{eff} [K]	log$g$	Z [dex]	ξ [km/s]	$\frac{\lambda}{\delta\lambda}$
BD+59 372	3930 ± 90	+0.1 ± 0.3	−0.10 ± 0.06	3.4 ± 0.2	13400
BD+56 595	3970 ± 25	+0.2 ± 0.3	−0.08 ± 0.12	4.1 ± 0.2	12400
HD 14404	3950 ± 40	+0.2 ± 0.1	+0.06 ± 0.09	4.1 ± 0.2	11500
HD 14826	3870 ± 25	+0.3 ± 0.2	+0.04 ± 0.10	3.6 ± 0.2	12600
HD 236979	4040 ± 30	−0.5 ± 0.1	+0.01 ± 0.06	3.1 ± 0.2	12300
HD 13136	4030 ± 40	+0.4 ± 0.2	−0.11 ± 0.09	4.3 ± 0.2	12200
HD 14270	3890 ± 25	+0.2 ± 0.3	+0.06 ± 0.12	3.8 ± 0.2	11200
BD+56 724	3740 ± 25	−0.5 ± 0.1	+0.10 ± 0.06	3.2 ± 0.2	11200
HD 14469	3730 ± 25	−0.1 ± 0.3	+0.11 ± 0.13	4.1 ± 0.2	10800
BD+56 512	3940 ± 40	+0.4 ± 0.4	+0.13 ± 0.11	4.1 ± 0.2	11000
HD 14488	3720 ± 70	+0.2 ± 0.1	+0.17 ± 0.08	3.2 ± 0.2	11700

Note. — Parameter fits to observed RSGs using the TURBOSPECTRUM grid of synthetic spectra calculated in LTE (Plez 2012; Alvarez & Plez 1998).

Model fits to the spectral database observed for this work as described in Chapter 2 allow us to determine the metallicity for the Perseus OB-1 RSGs. We measure Z = +0.04 ± 0.10 (LTE) and Z = −0.04 ± 0.08 (NLTE), where the $\pm\sigma$ values denote the standard deviation of the sample. Estimates of the global metallicity of the cluster are more precise, as the error in the mean scales the reported σ's by $N^{-0.5} = 0.3$ for our population of eleven stars.

The LTE model grid measures higher metallicities for cluster stars than the NLTE grid. This is to be expected; the cores of our strongest diagnostic lines (Fe I, Ti I, and Si I) are deeper in the NLTE case (see Figure 3.3). For any given observed spectrum, a NLTE fit will provide a lower measurement of metallicity. We find that using a full LTE grid of MARCS models induces, on average, a shift in Z of +0.07 dex for RSGs near solar metallicity.

We find good agreement between microturbulence values calculated in this work (2.9-4.3 [km/s] when compared to high resolution spectroscopy ($R\sim10^5$) of α Ori. Lundqvist & Wahlgren (2005) calculate a value of 4.5 km/s using 1D ATLAS9 LTE models. In Wahlgren et al. (2008), the authors refine that value of 3.1 km/s after fitting the same data with the newer 1D ATLAS12 LTE models.

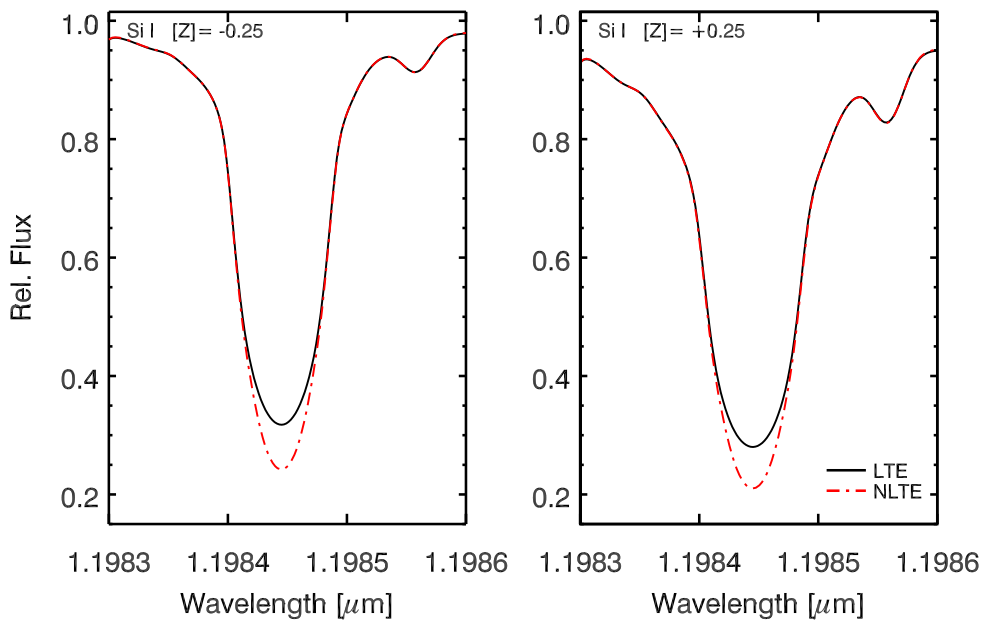

Figure 3.3 The effects of NLTE corrections on diagnostic lines. Left panel shows a model at Z = −0.25, right panel Z = +0.25

The nominal resolution of IRCS in our particular setup is R of ∼20,000. We measure resolutions of 11000 to 14000 (See Tables 3.2 and 3.3). Assuming the difference is caused by macroturbulence (broadening of spectral features based on turbulence in the atmosphere of the RSG), we calculate expected $v_{\rm macro} \approx 15{-}25$ [km/s]. As the resolution of our observations is on order of 15 [km/s], we note that these values should serve only as estimates. Still, they are in good agreement with literature values. Ramírez et al. (2000) and Cunha et al. (2007) find RSG macroturbulences of between 11-25 [km/s] using R=40,000 spectra for a population of galactic RSGs.

3.1.3 Metallicity

The average metallicity of Z = −0.04 ± 0.08 obtained for the Perseus OB-1 RSGs in this work agrees well with the metallicity of young massive stars in the solar neighborhood. Nieva & Przybilla (2012) studied a large sample early B dwarfs and giants using strongly improved detailed NLTE line diagnostics. They obtained surprisingly narrow ($\sigma \approx 0.05$) abundance distributions for the elements C, N, O, Ne, Mg, Si, Fe with average values very close to the sun (Asplund et al. 2009).

This implies that there is little scatter in metallicity of the young massive star population around the sun and also practically no chemical evolution over the last 5 Gyrs. The fact that we also obtain a metallicity very close to the solar value is, thus, a strong indication that the spectroscopic J–band method leads to reliable results.

Unfortunately, the study by Nieva & Przybilla (2012) does not include objects in Perseus OB-1. However, Firnstein & Przybilla (2012) have recently analyzed A supergiant stars in the solar neighborhood including some objects in Perseus OB-1. While this work focuses on the determination of stellar parameters and does not provide a detailed abundance study, it provides magnesium abundances for three objects with an average value of 0.10 dex below the Nieva & Przybilla (2012) average of B stars in the solar neighborhood (the uncerainty for each individual A supergiant is $\approx \pm 0.07$ dex). We take this as a confirmation that the metallicity of Perseus OB-1 is close to solar.

3.1.4 Effective Temperatures

We measure higher $T_{\rm eff}$ for all stars which overlap the target list of Levesque et al. (2005) (see Table 3.2). The average difference in temperatures is 270 ± 130 [K] for our NLTE calculations (220 ± 100 when compared with our LTE calculations), a significant discrepancy. There are a number of differences between this work and that of Levesque et al. (2005), including the new NLTE corrections we use when computing synthetic spectra, the fact that we fit for Z, micro turbulence, and spectral resolution, and the near IR spectral window of this work. The latter is the most likely candidate for the large difference in measured $T_{\rm eff}$ values. While we work in the J–band, Levesque et al. (2005) use optical spectra, concentrating on the strength of molecular bands of TiO to derive temperatures. Davies et al. (2013) have shown that the derivation of RSG temperatures using quantitative spectroscopy in optical bandpasses returns lower values than are measured using methods which are less dependent on model atmospheres (the *flux integration method*). In addition, Davies et al. (2013) show that optical temperatures overestimate the IR flux of RSGs when full spectral energy distributions are available and underestimate reddening as compared to nearby

stars. Temperatures derived from near IR spectroscopy alone are closer to those values from the flux integration method.

As discussed in Davies et al. (2013), new work with 3D models of RSGs will likely do much to resolve the issue of temperature derivation for RSGs, but only a few of these models are available so far (see, for example, Chiavassa et al. 2011).

3.1.5 Stellar Evolution

To compare our results with stellar evolution models we first construct an observational Hertzsprung-Russell diagram (HRD). We calculate bolometric luminosities for program stars using archival K band 2MASS photometry (Table 3.1, Skrutskie et al. 2006), the bolometric correction recipes of Davies et al. (2013), and distance modulus of Currie et al. (2010). We applied the Cardelli et al. (1989) extinction law using measurements of the reddening to Perseus OB-1 (Currie et al. 2010). These luminosities are plotted against the effective temperatures from our spectral fit in the HRD of Figure 3.4. We then over plot evolutionary tracks adopting the Geneva database of stellar evolutionary models including the effects of rotation (Meynet & Maeder 2000). All stars except one align along the evolutionary tracks, having zero age main sequence (ZAMS) masses of 15-20 $M_\odot$. This result is in good agreement with the age of Perseus OB-1 of 14±1 Myr (Currie et al. 2010). Only the 15 $M_\odot$ track agrees with this time frame. At the age of Perseus OB-1, 20 $M_\odot$ stars have already evolved from the RSG phase while 12 $M_\odot$ stars are still on the main sequence.

The object BD+59 372 is a clear outlier with a luminosity corresponding to a mass only slightly higher than 9 $M_\odot$ (see Table 3.2). At this point we have no explanation for this object.

An independent way to compare our spectroscopic results with stellar evolution is the comparison of gravities log g obtained from the spectroscopy and from evolutionary tracks. For the latter, we obtain a stellar mass from the observed luminosities by interpolating evolutionary track masses and luminosities at the effective temperature observed. This mass is then used in conjunction with the observed luminosity and effective temperature to calculate evolutionary gravities. Figure 3.5 compares evolutionary gravities obtained in this way with spectroscopic gravities. Besides one outlier (HD236979) we find general agreement and no indication of a

systematic discrepancy. We also note that the outlier in Figure 3.4, BD+59 372, as the object with the highest gravities agrees within the uncertainties of the error bars.

The general agreement between spectroscopic and evolutionary gravities can be used to discuss the influence of convective turbulence pressure on the model atmosphere stratification. The 3D-hydrodynamic convection simulations by Chiavassa et al. (2011) include effects of pressure caused by the convective motion on the atmospheric density stratification. On the other hand, the 1D MARCS models used in our analysis do not account for convective pressure. It is straightforward to show (see, for instance, Chiavassa et al. 2011, eq. (8)) that as the result of convective pressure the stellar gravity is reduced to an effective gravity which can be approximated by

$$\log g_{\rm eff} = \log g - \log(1 + \beta v_{\rm turb}^2 / v_{\rm sound}^2) \tag{3.1.1}$$

where $v_{\rm turb}$ is the average turbulence speed and $v_{\rm sound}$ the sound speed. β is a parameter close to unity if the turbulent velocity fields is almost isotropic. Chiavassa et al. (2011) concluded from their calculations and a comparison with MARCS models that gravity corrections of 0.25 to 0.3 dex are needed to match the density stratifications of the 1D with the 3D models corresponding to turbulence velocities of the order of the sound speed.

Our comparison of spectroscopic and evolutionary gravities does not indicate a systematic effect of this order. On the other hand, our two objects with the lowest spectroscopic gravities may well be influenced by large effects of turbulence pressure.

3.1.6 Composite Cluster Spectrum

The scientific strength of the low resolution J–band technique derives from the radiative power of RSG stars. In this work we carefully demonstrate that the method is stable and precise well below the spectral resolution of current instrumentation on the largest telescopes available, notably MOSFIRE on Keck and KMOS on the VLT. With these multiplexed instruments we are able to efficiently apply this technique to entire populations of RSGs as individual objects over extragalactic distances. DFK10 calculate a limiting distance for the technique of 7-10 MPC using a single RSG.

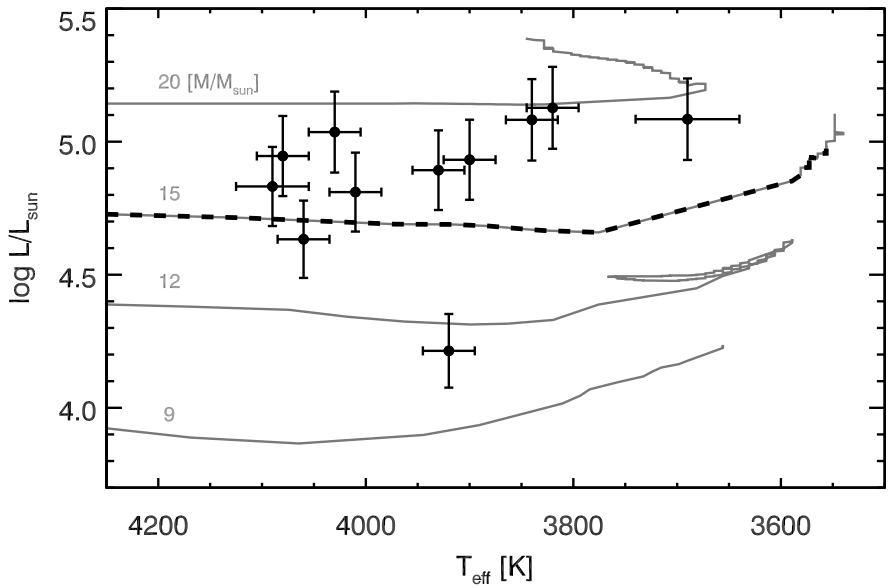

Figure 3.4 H-R diagram of program stars. Bolometric corrections are taken from Davies et al. (2013). Overplotted in gray are Geneva evolution tracks for solar metallicity including the effects of rotation, labeled with their zero-age main sequence mass. The bold dashed overlay represents the space on the geneva tracks which covers the literature age of Perseus OB-1, 14 ± 1 Myr (Currie et al. 2010).

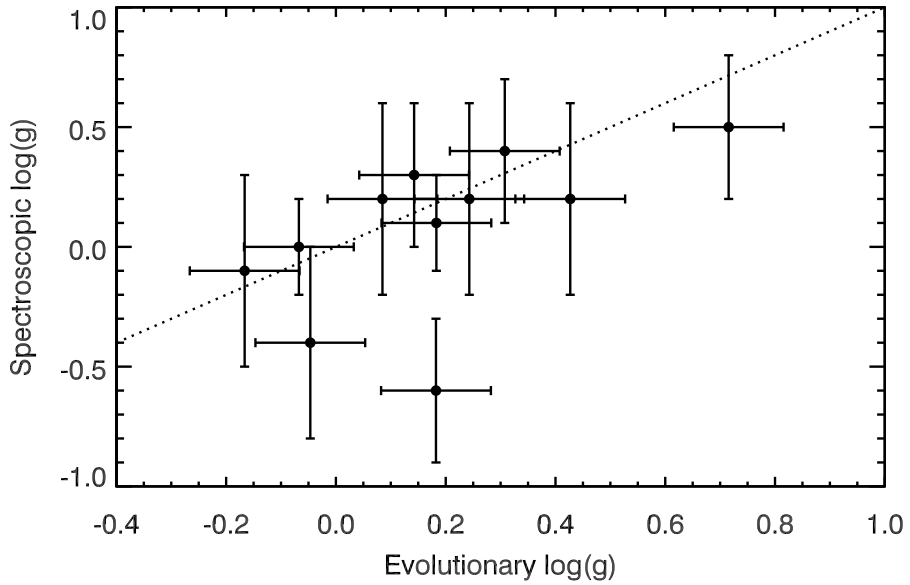

Figure 3.5 A comparison between parameter fits for log$g$ and a calculation of the expected log$g$ values from stellar evolution theory given the age of Perseus OB-1. We find general agreement and note that outliers may be affected by significant turbulent pressure (see §3.1.5)

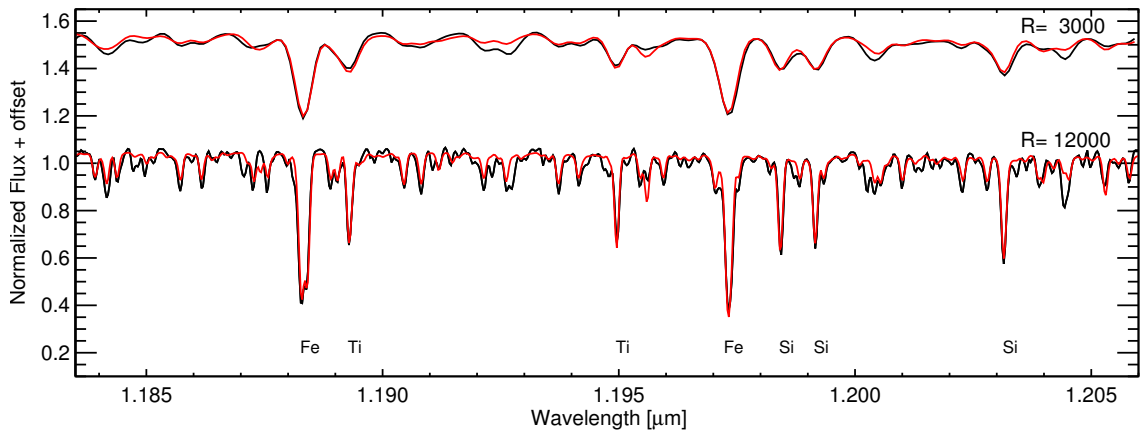

Figure 3.6 The Perseus OB-1 "cluster spectrum" created when all eleven RSG spectra are summed together as weighted by their J magnitudes. The spectrum is plotted twice at different resolutions. We over plot the best fitting model in red.

In Gazak et al. (2013) we presented simulations showing that the near-IR flux of young super star clusters (SSCs) is dominated by their RSG members. These simulations show that the J–band spectrum of a SSC older than 7 Myr will appear very similar to that of a single RSGs. This opens the possibility to use the integrated J–band light of SSCs in distant galaxies as as a source for spectroscopic determination of galaxy metallicities.

Our collection of Perseus OB-1 spectra allows us to test this possibility. With a total estimated mass of 20000 $M_\odot$ (Currie et al. 2010) Perseus OB-1 comes close to the observed mass range of extragalactic SSCs. We construct a simulated SSC spectrum by adding our observed RSGs weighted by their J–band luminosities. The spectrum is shown in Figure 3.6. We then apply the same analysis technique as in section 3 and obtain a metallicity of Z = -0.03 ± 0.12 (NLTE), very similar to the average metallicity obtained from the analysis of the 11 individual spectra. The effective temperature obtained from the cluster spectrum is $T_{\rm eff}$= 3970 $\pm$ 30 and the gravity log$g$= +0.1 $\pm$ 0.2. In agreement with the LTE study of the individual Perseus OB-1 supergiants we measured Z = +0.08 $\pm$ 0.12, $T_{\rm eff}$= 3910 $\pm$ 70, and log$g$= +0.2 $\pm$ 0.1 when fitting with the full LTE model grid.

In Chapter 4 we will show that that the RSG supergiant population will provide ∼95% of the J–band flux in a young SSC (Gazak et al. 2013) . To simulate the effect of the 5% contaminative

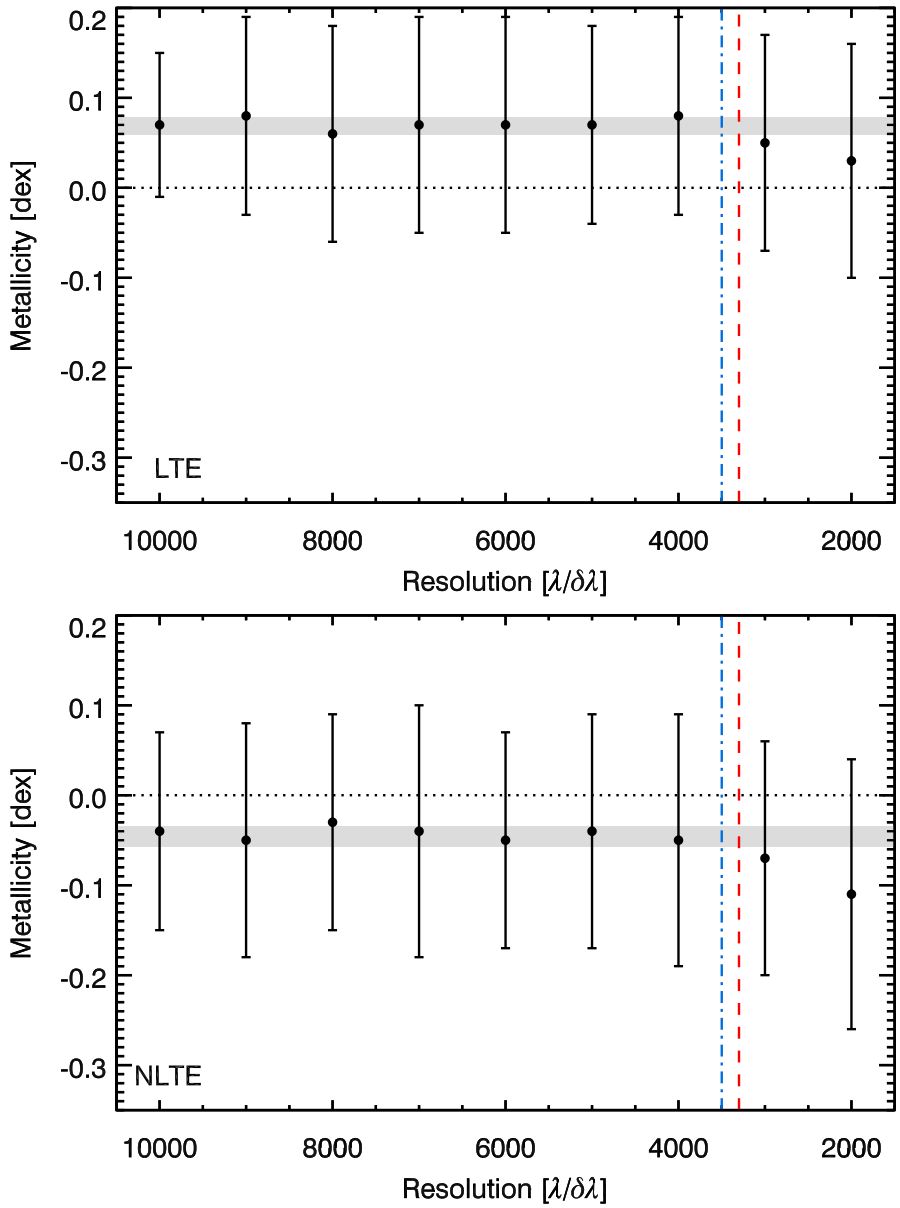

Figure 3.7 Evolution of the average measured metallicity for our sample of Perseus OB-1 stars collapsed into a synthetic cluster spectrum as a function of spectral resolution. Error bars are derived using the Monte Carlo technique discussed in §2.4. The horizontal gray region shows $\pm 1\sigma$ of the average metallicity between $10000 \leq \mathrm{R} \leq 3000$, demonstrating the stability of the technique down to resolutions of R=3000. Vertical lines mark the spectral resolutions of key J–band spectrographs, KMOS on VLT in dash-dotted blue and MOSFIRE on Keck in dashed red. A horizontal dotted line marks solar metallicity. We plot results from the LTE model grid (upper panel) and NLTE grid (lower panel).

flux we added a flat spectrum of 5% of the total flux. We then re-fit the spectrum and measured -0.08 ± 0.13 (NLTE) and $+0.06 \pm 0.14$ (LTE). The change in measured metallicity is minimal (with a systematic offset of at most +0.05 dex) and in the proper direction−contaminant flux will weaken the deepest lines more strongly and thus a drop in extracted metallicity is to be expected. However, the two results agree statistically and offer strong evidence that spectroscopy of unresolved young SSCs can become a powerful application of the J–band technique. We find in this case that an unresolved cluster of proper age can be successfully fit with a single RSG template model, a technique which has been used at very high resolution in the H band (Larsen et al. 2006).

We vary the resolution of our synthetic cluster spectrum down to R=2000. The results of this work echo that of the individual stars, showing stability in fit parameters down to resolutions around 3000. The NLTE and LTE cases of this test are plotted in Figure 3.7.

3.1.7 Conclusions

We obtain reliable abundances in agreement with high resolution, high signal to noise spectroscopy of young massive B-stars in the solar neighborhood. Using the advantage that all of our RSGs formed within a stellar cluster we test our derived parameters against predictions of stellar evolution theory for a cluster of mass and age of Perseus OB-1. Our results are in good agreement with such theoretical work. We thus confirm the technique presented in DFK10 and show that it remains stable down to resolutions of R≈3000. This provides a reliable method to determine extragalactic metallicities from individual RSGs to distances of 7-10 Mpc with existing telescopes and instruments.

By utilizing the large populations of RSGs in young, spatially unresolved SSCs we can extend the applicability of the J–band technique out to distances ten times greater with the same instruments. Thus SSCs may allow us to reach beyond the local group and measure the metallicities of star forming galaxies from the stars themselves instead of relying on existing techniques which are empirically calibrated. We develop the theoretical and observational methods of this SSC method in Chapter 4.

3.2 M31

3.2.1 Motivation

M31−the Andromeda galaxy−is the largest member of the Local Group and a key target for studying star forming galaxies. As the spiral galaxy nearest to the Milky Way, M31's projected extent of over three degrees presents both a scientific opportunity and observational challenge. Efforts to understand M31's metallicity and abundance gradient has been largely targeted towards H II regions, with a recent new dataset and reanalysis of all 85 existing H II observations by Zurita & Bresolin (2012). By applying different "strong line" calibrations, the authors calculate metallicity gradients (in dex/kpc) between -0.007 ± 0.007 and -0.029 ± 0.005, and find a final gradient of -0.023 ± 0.002 after removing calibrations yielding outliers. More shocking, though, is the $\sim$0.3 dex offset between the derived central metallicity using different calibrations such that the value is constrained only between 1.4 and 2.2 times the solar value. This is astonishing when one notes that M31 is within 1 Mpc of the Milky way. In comparison, using 15 blue supergiant stars in M81 at 3.5 Mpc our team has derived a central metallicity of 0.286 ± 0.061 (a spread of ~ 0.12 dex) and a gradient of -0.033 ± 0.009 [dex/kpc] (Kudritzki et al. 2012).

As a massive, nearby spiral galaxy, M31 offers a tantalizing chance to add a high precision measurement of metallicity and gradient to the ongoing scientific effort to understand the evolution of central metallicity and gradient slope with galaxy mass. As a push has been made to use supergiant stars as metallicity indicators at farther and farther distances, the fact that M31 has been largely ignored is due mainly to the challenge of observing enough stars and over a significant range of the galaxy's radial extent. Another common problem is target selection−the large projection of M31 on the sky leaves significant foreground contamination due to dwarfs in the Milky Way halo. To date, spectroscopic observations of the stellar population of M31 are surprisingly sparse: 7 B−type supergiants were studied by Trundle et al. (2002) (and one from the same sample by Smartt et al. (2001)), while another one F− and two A-type supergiants were studied by Venn et al. (2000). These studies are disjointed and individual measurements of metallicity often have error bars of 0.2 to 0.4 dex. The existing sample of stars is thus too small to draw accurate conclusions.

A self consistent study of the stellar population in the disk of M31 is a necessity to make the measurements of central metallicity and abundance gradient for this massive, nearby galaxy.

3.2.2 Target Selection

We focus our observational efforts on the published catalogue of M31 RSGs by Massey et al. (2009). The authors of this work provide a powerful photometric selection technique yielding 437 RSG candidates from the LGGS catalog. Massey et al. (2009) conducted a radial velocity (RV) campaign and observed 16% of the sample, finding that *every* photometric candidate observed was consistent with membership in M31. As objects in the M31 stellar disk, the magnitudes and colors of these candidates basically assures that they are M31 RSGs. Finally, the authors collected optical spectra of sixteen of the RSG candidates and found all of them to be RSGs.

We note that the while the Massey et al. (2009) photometric cuts select RSGs with high fidelity, the method is not designed to find *all* RSGs. Thus many M31 RSGs remain unaccounted for, falling into a color and magnitude range where contamination with foreground objects is higher. Our mask designs focus on first the spectroscopically confirmed RSGs, then those with RV membership in M31, followed by the photometric candidates. To fill empty space in the masks we will dip into the photometric range where Milky Way halo objects begins to affect the selection. We still expect that a significant fraction of these objects will be RSGs in the disk of M31.

Focusing on the high probability RSGs discussed above, we have conducted a statistical study to carefully understand our observational requirements. We selected a number of candidate fields across the disk of M31 and for each combination of two to five masks (the minimum to measure a gradient and the maximum that can be observed in one night, respectively), we conduct the following simulation. First, we construct a simulated measurement of the abundance gradient by applying the values of Zurita & Bresolin (2012) to the de-projected radial distance of each target. For each "measurement" we apply a random scatter of characteristic size 0.1 dex and assign the same uncertainty to the new value. We repeat this process 10,000 times per arrangement of masks, and compile the statistics of linear regression fits for the gradient and central metallicity of each monte carlo trial.

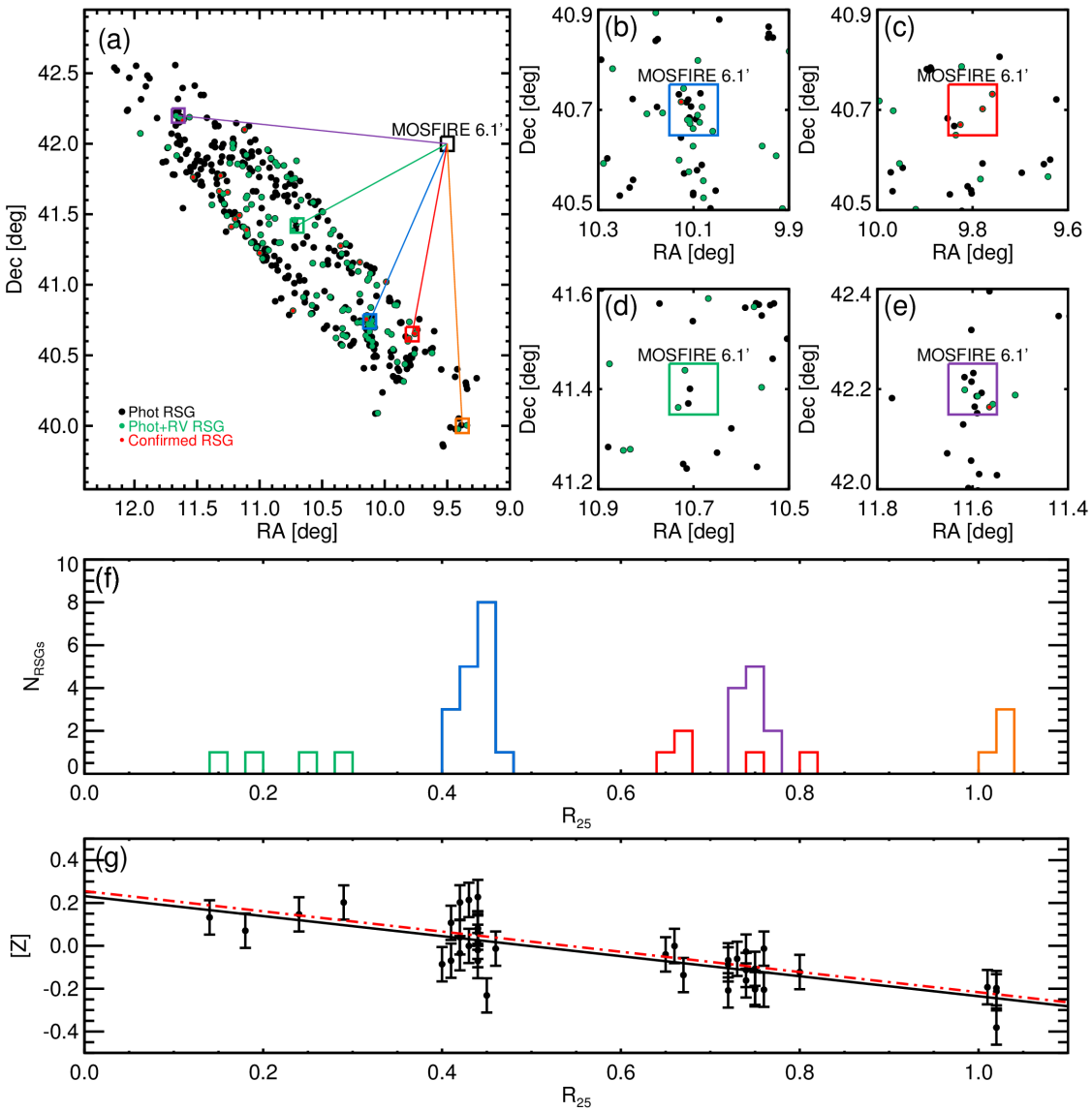

Figure 3.8 Target selection visualizing full radial coverage of M31 with five MOSFIRE fields observed in one night. (a) plots all RSG candidates from Massey et al. (2009) color coded by likeliness: Red are confirmed RSGs, green are photometric candidates and RV members of M31, black are photometric candidates without RV measurements. Note that according to Massey et al. (2009), even the photometric candidates have a better than 90% probability to be M31 RSGs. (b)-(e) plot a detailed zoom of four fields. (f) plots the radial coverage of our target selection normalized to the 25th mag isophote (R_{25}). Radius measurements are de-projected from the on-sky inclination of M31. (g) shows a simulated abundance gradient assuming the measured value of Zurita & Bresolin (2012) and using our expected accuracy of 0.1 dex. The black line is the measured fit for the simulated data, while the red shows the literature measurement based on highly uncertain H II-region measurements (see text).

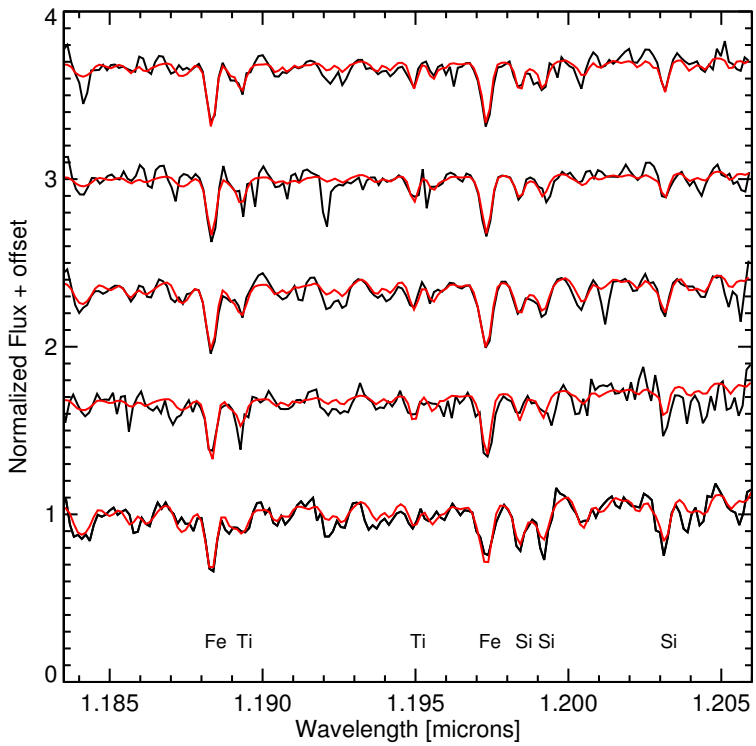

Figure 3.9 A sample of M31 J–band RSG spectra with over plotted spectral fits. The metallicities are slightly super-solar (see Table 3.4).

Of course the Central Limit Theorem dictates that we arrive perfectly at the values of Zurita & Bresolin (2012). The real power in these simulations is that we are able to predict the accuracy with which we would determine those values given the choice of observing fields. For an optimal arrangement of five masks (see Fig 3.8), we simulate a precision determination of the gradient with an error of $\pm$ 0.002 dex/kpc and a determination of the central metallicity with an accuracy of $\pm$ 0.03 dex. The lack of need for empirical calibrations when observing stars instead of H II regions drives the significant increase in our measurement of central metallicity. We note also that any additional RSGs observed from the higher-contamination sample used to fill in the masks will further improve our determination of these parameters.

Table 3.4. NLTE Stellar Parameters for M31 Red Supergiants

Target	r/r_{25}	T_{eff} [K]	log$g$	Z [dex]	ξ [km/s]
J004035.16+404105.2	0.462	4350 ± 20	−0.55 ± 0.20	+0.11 ± 0.10	3.12 ± 0.32
J004019.15+404150.8	0.461	4230 ± 20	+0.58 ± 0.20	+0.06 ± 0.12	3.97 ± 0.20
J004030.64+404246.2	0.441	4080 ± 50	−0.43 ± 0.15	+0.13 ± 0.08	3.75 ± 0.28
J004031.00+404311.1	0.436	3600 ± 30	−0.45 ± 0.20	+0.15 ± 0.15	3.02 ± 0.20
J004026.79+404346.4	0.435	3860 ± 50	+0.29 ± 0.24	+0.10 ± 0.12	3.00 ± 0.20

Note. — Parameter extractions for a sample of RSGs observed in M31.

3.2.3 Initial Results

It was the unfortunate case that we were able to observe only one field in the disk of M31 due to averse weather conditions. The analysis of only a single field does not allow for a measurement of the abundance gradient of M31, but we are able to provide a first discussion on the global metallicity of this galaxy. In Table 3.4 we show parameter fits for this field. Our analysis indicates metallicities ranging from Z = +0.06 to +0.15, indicating super solar metallicity ($\sim 1.2\times$) at roughly 0.45 times the isophotal radius (9.5 kpc).

Zurita & Bresolin (2012) find a central metallicity of between 1.4 and 2.2 times solar (for oxygen abundance and depending on the $H\,ii$ region calibration used) and a gradient of -0.56 (± 0.28) r/r_{25}. At $r/r_{25} \simeq 0.45$ for the field observed in our program this corresponds to Z = -0.10 or Z = 0.09, respectively. Our result indicates agreement with their high metallicity solution. In October of 2014 we will attempt a second observing campaign with MOSFIRE at Keck and, given better conditions, will be capable of providing a study of the central metallicity and gradient in M31 from the RSG population.

3.3 NGC 300

3.3.1 Motivation

Since the start of this dissertation work, the J–band technique has matured and scientific applications are well under way. To understand and develop the technique, we applied it to the Milky Way Perseus OB-1 cluster in Gazak et al. (2014b), which is described in Chapter 2. In Davies et al. (2014, submitted), we apply our technique to RSGs in the LMC and SMC. While the first attempt at observing M31 was hindered significantly by weather conditions, we have extracted promising initial results and will soon attempt a second observing campaign with MOSFIRE at Keck using time granted by the Institute for Astronomy Time Allocation Committee (§3.2). Now, we are ready to begin to realize the true power of the J–band RSG technique, namely to push beyond the Local Group of galaxies and out into the wider universe. The ideal target for this first application is NGC 300, a star forming spiral galaxy in the southern skies at a distance of 1.9 Mpc.

NGC 300 has been well studied with the two existing methods of extracting present day cosmic abundances, blue supergiants and H II regions (Kudritzki et al. 2008; Bresolin et al. 2009a). Those studies show excellent agreement between H II region T_e based oxygen abundances and metallicities determined from the blue supergiant method. Still, there is a wide range in central metallicity and radial gradient when applying "strong line" H II techniques (Bresolin et al. 2009a). Based on the successful metallicity indicators, the galaxy presents an obvious gradient, with a nearly solar value of metallicity at its center and well below half solar near the isophotal radius. The J–band technique must be sensitive to such varying metallicity in a single population and thus a test on such a well established case is critical.

With the successful demonstration of the J–band technique to resolutions of lower than R=3000 (Chapter 2, Gazak et al. 2014b) we obtained nights on the newly commissioned KMOS instrument on the VLT to observe RSGs across the star forming disk of NGC 300.

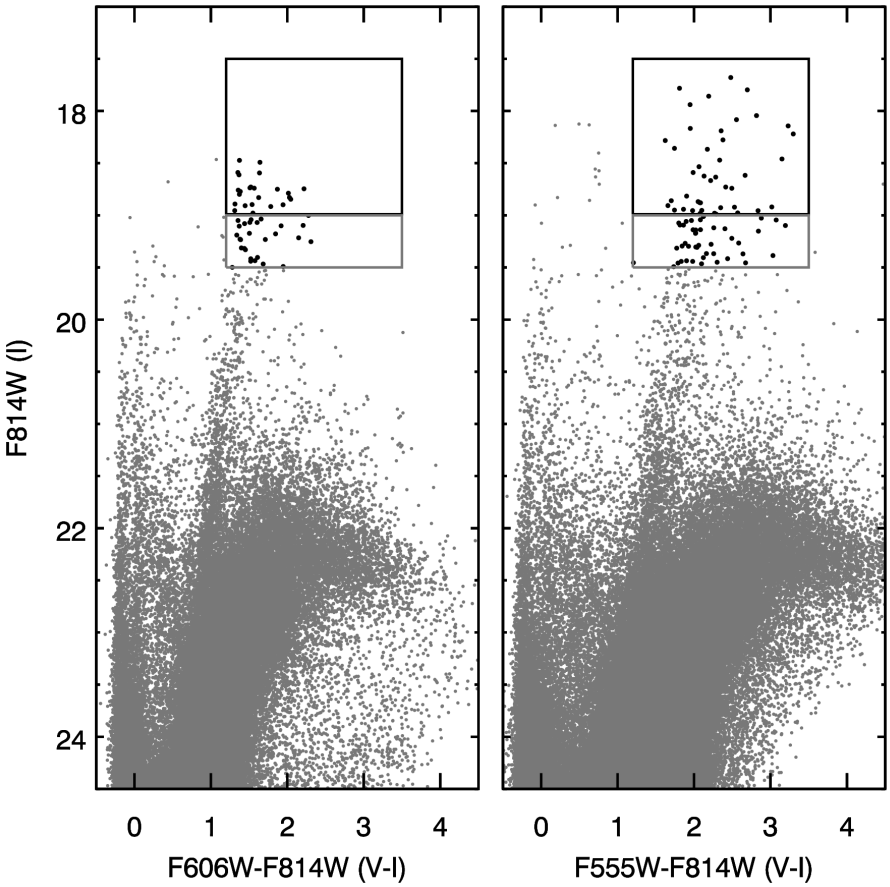

Figure 3.10 Color Magnitude selection for extragalactic RSGs. The left panel shows color vs magnitude for the WFPC observations of NGC 300 while the right panel is the same but for ACS fields (See §3.3.2, Fig. 3.11). The boxed regions show the brighter "priority one" RSG candidates in this color magnitude space and the fainter "priority two" region below.

3.3.2 Target Selection

We prepared an initial database of RSG candidates using the ACS Nearby Galaxy Survey Treasury (ANGST: Dalcanton et al. 2009), a public database of stellar photometry measured from Hubble Space Telescope observations. The ANGST catalog contains 6 fields in NGC 300 from the Advanced Camera for Surveys (ACS) and 3 fields observed with the Wide Field and Planetary Camera 2 (WFPC2). The layout of these fields can be seen in Figure 3.11. We select the red F814W ("I") filter for magnitude cuts. The color cut for both instruments was F555W−F814W filters for ACS, F606W−F814W filters for WFPC2 (V−I). The cool temperatures and extreme luminosities of RSGs allow for high fidelity selection using such color-magnitude cuts. This is demonstrated in Figure 3.10: the "RSG plume" (boxed) separates from the population of fainter red objects in m_I magnitude dimension and is distinct from other bright, hotter objects with a red V−I color. Using the ANGST photometry we define RSG candidates as those objects with colors bounded in V−I color between 1.2 and 3.5. and having m_I brighter than 19.5, a value selected to achieve our target signal to noise ratio (SNR) of ∼100 (Gazak et al. 2014b). Seeking the best spectra possible we divided these targets into two lists separated at $m_I \geq 19.0$ and gave higher priority to the brighter group.

Because the HST coverage of NGC 300 is incomplete we used overlaps in our database with a more complete but shallower catalog of B and V photometry (Bresolin, private communication) to train a B−V vs m_V color-magnitude cut. Candidates selected by this method were placed in a third ranked priority group such that HST selected targets would be observed first but that no IFUs would go unused.

As a final adjustment to our RSG candidate list we search for overlaps between our existing candidates and Spitzer photometry of NGC 300 from Khan et al. (2010). The important Spitzer diagnostic for RSG candidacy is the color-magnitude plane defined using IRAC Band 1($m_{3.5}$) and the color Band 1 − Band 2 ([3.5]−[4.5]). RSGs separate as the brightest $m_{3.5}$ targets with color blueward of 0.0 in [3.5]−[4.5] (Verhoelst et al. 2009). We upgrade all objects in our candidate list with overlap as Spitzer RSG candidates to the top priority group.

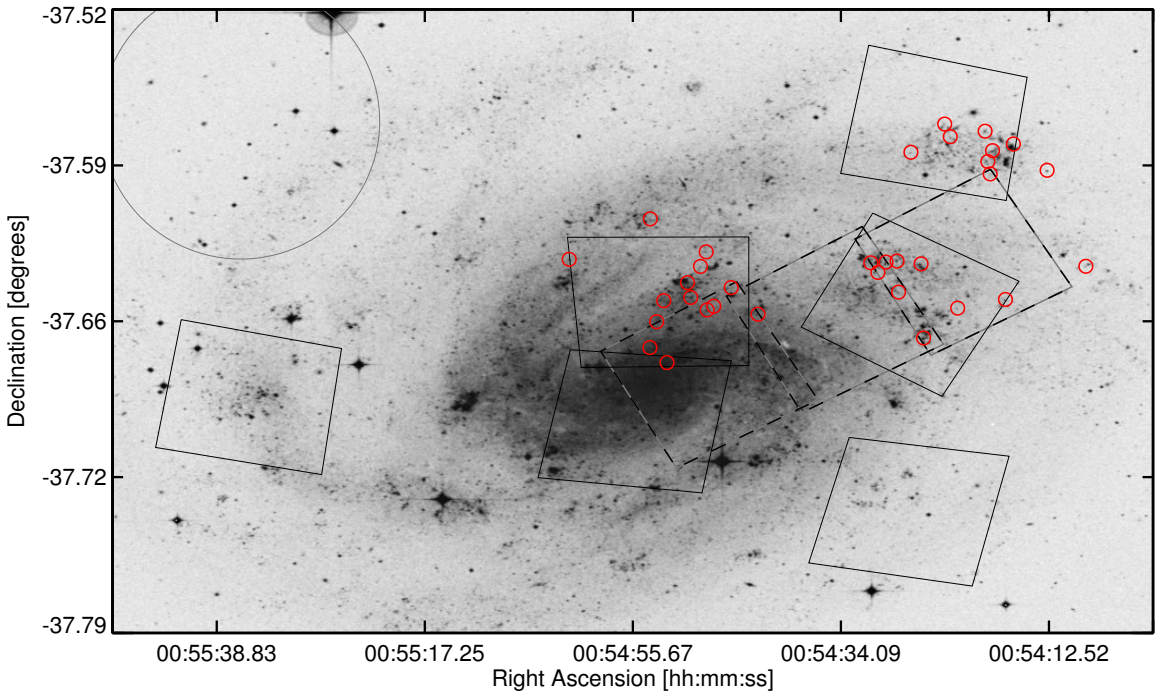

Figure 3.11 The spiral galaxy NGC300. The Hubble ACS fields are over plotted in black, with WFPC2 frames in black dashed with gray. Observed RSGs are circled in red. In the upper left a gray circle denotes the size of the KMOS field of view, within which 24 IFUs can be placed per pointing.

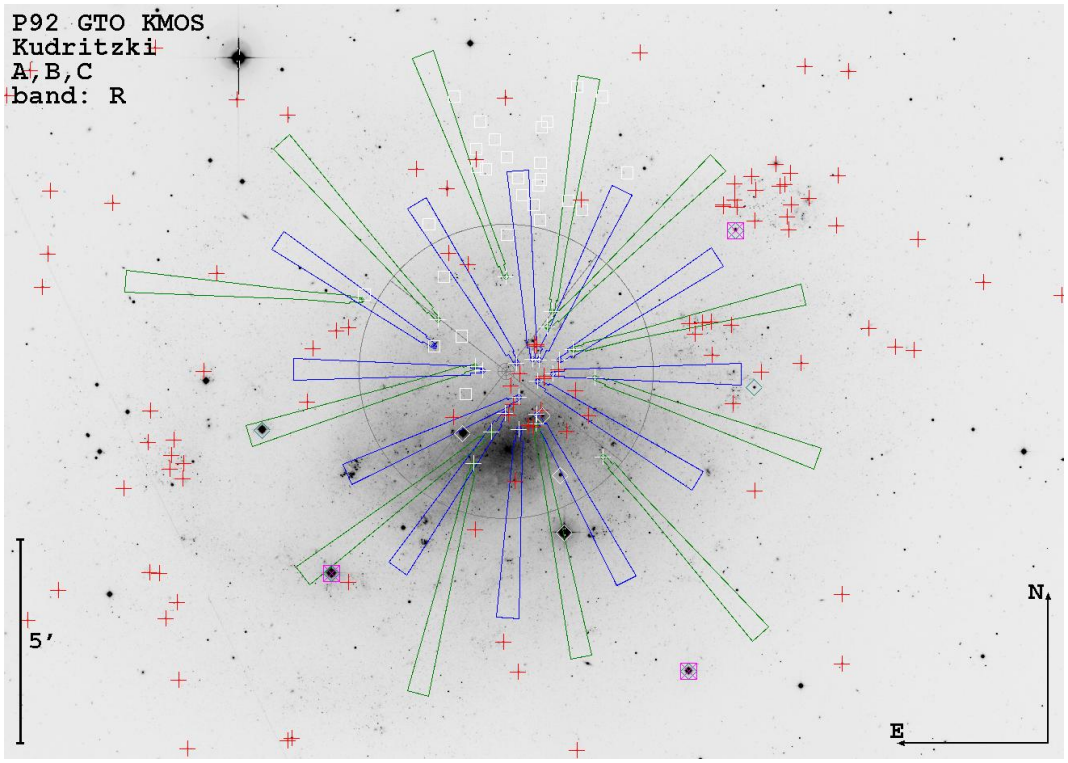

Figure 3.12 The KMOS KARMA Arm Allocation tool. After preparing a database of RSG candidates, the complexities of arranging fields for observation with KMOS are minimized by the provided KARMA software. An example of the inner layout for one KMOS field (the gray circle) and the KMOS IFU arms (blue and green) arranged to most efficiently observe the field.

3.3.3 Observations

The resulting candidate catalog was used as input to the KMOS ARM Allocator (KARMA) software for planning the setup of the 24 KMOS Integral Field Units (IFUs). These $2''.8$ square IFUs can be placed over the $7'.2$ KMOS field of view (shown in Figure 3.11). We observed an inner and outer field to cover a significant range of the radial extent of NGC300. These fields were observed in 600s integrations over the nights of 2013 October 14, 15, and 16. The 14th and 15th nights were clear and stable at Paranal with median seeing of $\approx 1''.1$. Weather degraded slightly on the night of the 16th with intermittent cloud cover and variable seeing with the median value around $1''.3$.

KMOS was operated in nod to sky mode with science integrations of 600 seconds. Telluric standards were observed down each IFU at a frequency of once per every 60 to 90 minutes. KMOS IFU data cubes were flat fielded, wavelength calibrated, and telluric corrected using the KMOS pipeline (v1.3.2) provided publicly as a specific instance of the European Southern Observatory (ESO) Reflex automated data reduction environment (Freudling et al. 2013). We employ a manual sky subtraction using background spaxels on science exposure frames. We produce final science spectra by extracting the median of all individual frames. The spectral atlas is plotted in Figures 3.13 and 3.14.

3.3.4 Results

Measured parameters and their uncertainties are listed in Table 3.5, arranged by increasing radial distance from the center of NGC 300. The parameter fits are in general quite precise, and while we note one significant outlier (object 134) which appears significantly higher metallicity than the rest of the sample, we find no obvious reason to discount this object. The strength of the Si I lines may indicate that this object is of higher temperature than our grid covers (see the increased sensitivity of Si to $T_{\rm eff}$ in Figure 2.2) and, in fact, we do fit at the high edge of our temperature range. In this case this object may be a higher mass star which settles briefly into the fully convective Hayashi Limit at temperatures of closer to 5000K.

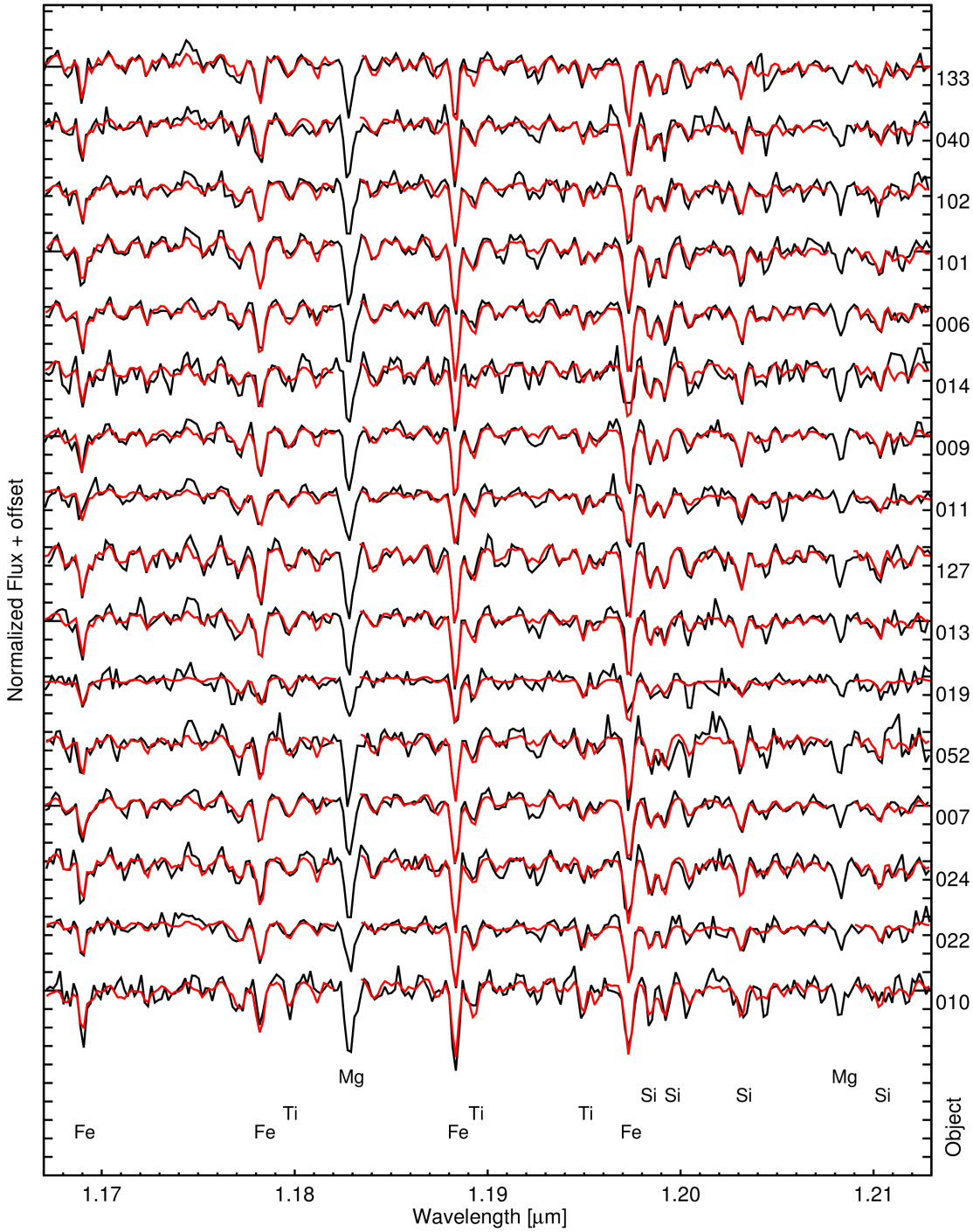

Figure 3.13 First half of the NGC 300 RSG spectra plotted in black with corresponding best model fits in red. Diagnostic features are marked. Each object is labeled to the left of the plotted axis and information corresponding to the fit is tabulated by this name in Table 3.5. NLTE corrections are not yet available for lines of Mg I, so they are masked out in this analysis.

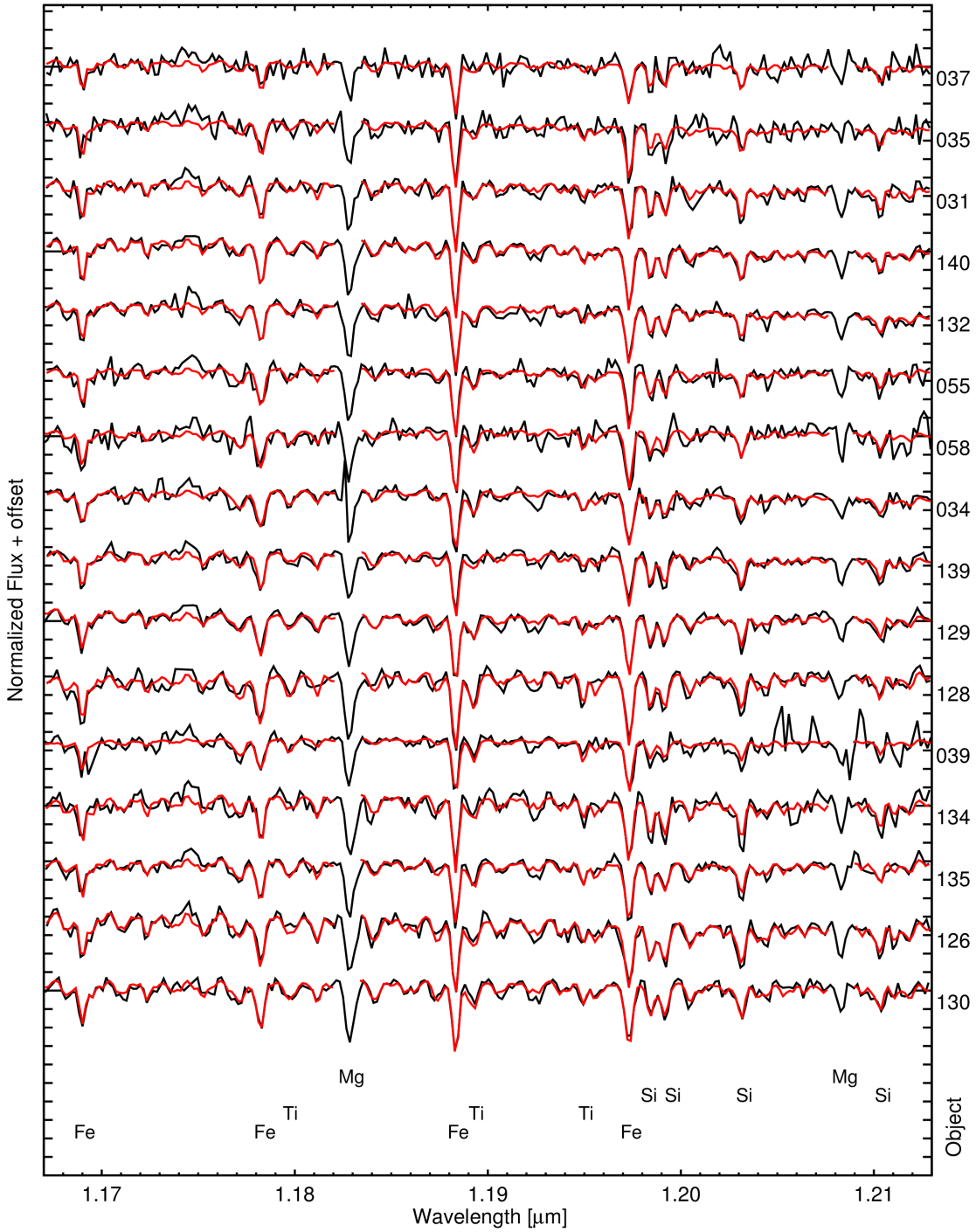

Figure 3.14 Second half of the NGC 300 RSG spectra plotted in black with corresponding best model fits in red. Diagnostic features are marked. Each object is labeled to the left of the plotted axis and information corresponding to the fit is tabulated by this name in Table 3.5. NLTE corrections are not yet available for lines of Mg I, so they are masked out in this analysis.

Table 3.5. NLTE Stellar Parameters for NGC 300 Red Supergiants

Target	r/r_{25}	T_{eff} [K]	log$g$	Z [dex]	ξ [km/s]
010	0.069	3770 ± 40	−0.52 ± 0.4	−0.08 ± 0.11	4.2 ± 0.2
022	0.120	3560 ± 30	−0.74 ± 0.2	−0.17 ± 0.13	3.0 ± 0.2
024	0.204	4040 ± 30	+0.21 ±0.3	−0.04 ± 0.11	4.1 ± 0.2
007	0.250	3800 ± 20	−0.56 ± 0.3	−0.15 ± 0.15	4.2 ± 0.2
052	0.265	4090 ± 50	−0.48 ± 0.5	−0.15 ± 0.12	4.2 ± 0.2
019	0.272	3580 ± 40	−0.01 ± 0.2	−0.06 ± 0.12	2.1 ± 0.2
013	0.282	3800 ± 50	−0.71 ± 0.2	−0.20 ± 0.13	4.3 ± 0.2
127	0.293	4060 ± 40	−0.36 ± 0.5	+0.06 ± 0.16	3.9 ± 0.3
011	0.330	3710 ± 40	−0.16 ± 0.3	−0.55 ± 0.20	1.6 ± 0.4
009	0.332	3930 ± 30	−0.48 ± 0.2	−0.06 ± 0.14	4.0 ± 0.2
014	0.384	4230 ± 40	−0.47 ± 0.4	−0.08 ± 0.11	2.3 ± 0.2
006	0.432	4095 ± 40	−0.95 ± 0.3	−0.26 ± 0.12	4.0 ± 0.3
101	0.487	4085 ± 50	−0.70 ± 0.3	−0.01 ± 0.13	4.2 ± 0.2
102	0.551	3790 ± 40	−0.76 ± 0.2	−0.31 ± 0.11	3.1 ± 0.2
040	0.559	3830 ± 40	−0.24 ± 0.6	−0.27 ± 0.11	3.1 ± 0.2
133	0.564	4215 ± 40	−0.77 ± 0.3	−0.31 ± 0.13	3.2 ± 0.2
130	0.569	4000 ± 30	−0.48 ± 0.3	−0.30 ± 0.10	4.0 ± 0.2
126	0.589	4320 ± 50	−0.84 ± 0.4	−0.12 ± 0.12	4.1 ± 0.2
135	0.590	3940 ± 50	−0.62 ± 0.2	−0.35 ± 0.12	3.0 ± 0.2
134	0.610	4340 ± 30	−0.48 ± 0.4	+0.25 ± 0.15	3.0 ± 0.2
039	0.647	3980 ± 50	−0.18 ± 0.6	−0.33 ± 0.16	2.8 ± 0.3
128	0.672	3830 ± 30	−0.37 ± 0.2	−0.02 ± 0.13	4.5 ± 0.2
129	0.776	4050 ± 40	−0.06 ± 0.3	−0.36 ± 0.12	3.8 ± 0.2
139	0.866	4400 ± 10	−1.00 ± 0.3	−0.44 ± 0.14	2.9 ± 0.2
034	0.918	3970 ± 30	+0.10 ± 0.4	−0.48 ± 0.15	3.9 ± 0.2
058	0.940	3840 ± 40	−0.69 ± 0.2	−0.45 ± 0.15	2.8 ± 0.3
055	0.949	3890 ± 30	−0.85 ± 0.2	−0.42 ± 0.13	2.6 ± 0.3
132	0.962	4110 ± 20	+0.69 ± 0.3	−0.47 ± 0.13	4.3 ± 0.3
140	0.970	4055 ± 40	−0.48 ± 0.3	−0.59 ± 0.12	4.0 ± 0.2
031	0.975	4220 ± 40	−0.37 ± 0.2	−0.47 ± 0.14	3.6 ± 0.2
035	1.004	4140 ± 50	+0.24 ± 0.5	−0.56 ± 0.16	4.0 ± 0.3
037	1.014	4370 ± 30	+0.10 ± 0.4	−0.38 ± 0.15	2.7 ± 0.2

Note. — Stellar parameters for the population of RSGs observed in NGC 300

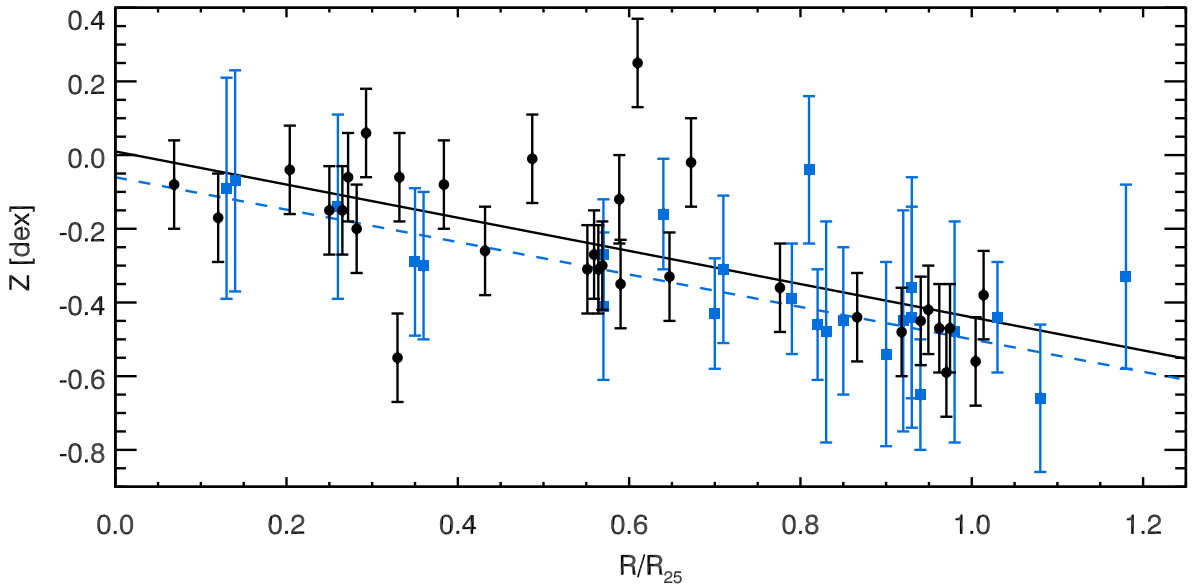

Figure 3.15 The stellar abundance gradients in NGC 300 at 1.9 Mpc. Blue squares are BSGs from Kudritzki et al. (2008), black circles are RSGs from this work.

The most direct comparison of our metallicity results is to work by Kudritzki et al. (2008), who studied 24 A-type supergiants across the radial extent of this galaxy. This first step in quantitative stellar spectroscopy beyond the local group of galaxies used synthetic NLTE spectra to derive metallicities using an ensemble of heavy atomic species (Mg, Si, S, Ti, Cr, and Fe). Using an assumed solar abundance pattern from Grevesse & Sauval (1998) they derive metallicities as a function of the solar value from that host of elements. The precision on individual measurements of metallicity was roughly 0.2 dex and allowed for the measurement of central metallicity of -0.07 ± 0.09 dex and a gradient of -0.081 ± 0.011 dex kpc^{-1}. We note that the original Kudritzki et al. (2008) values for central metallicity and gradient were -0.06 dex and -0.083 dex kpc^{-1}, respectively. We applied the new galactic orientation model of Bresolin et al. (2009a) to calculate slightly different galactocentric distances. This resulted in a small change of those parameters.

Our J–band method is a natural extension of the Kudritzki et al. (2008) technique. We use an independent but evolutionarily connected population of stars, as blue supergiants below masses of $\sim$35M$_\odot$ evolve into the RSGs we observe as they exhaust their core hydrogen. By all means, then, the two techniques should agree. Still, the stellar models and synthetic spectral calculations

are independent for our two techniques as the physical conditions of these two populations are distinct. The cool, inflated atmospheres of RSGs contain a host of singly ionized metals and a forest of molecular features which are absent in the hot spectra of BSGs. We also observe our stars in a different wavelength regime subject to separate observational difficulties. Finally, due to the added complexity of RSG atmospheres it is not yet possible to perform calculations in pure NLTE, even though our grid of synthetic spectra do have NLTE corrections for the most critical spectral features. Despite these differences, the J–band technique derives metallicity as a ratio of the solar abundance pattern just as the BSG method does, using strong atomic lines of Fe, Ti, Si, and Mg. Our observations of NGC300 RSGs then become an excellent test of both methods and of the theoretical calculations from which they draw.

We measure a central metallicity of $+0.01 \pm 0.04$ dex and a gradient of -0.084 ± 0.011 dex kpc^{-1}. This is a stunning agreement between BSGs and the RSG J–band method and certainly represents a breakthrough of the technique.

Bresolin et al. (2009a) provide an important second measurement of the central metallicity and gradient of NGC 300 using measurements of H II region auroral lines. As discussed in §1.3, the [O III] auroral lines give access to a key physical parameter, the electron temperature T_e, which can disentangle the effect of line strengths based on oxygen abundance and temperature. Bresolin et al. (2009a) find a central oxygen abundance of 12+log(O/H) = 8.57 ± 0.02 and a gradient of -0.077 ± 0.006 dex kpc^{-1}. The gradient is slightly shallower than for the RSGs and BSGs, but the difference is small. The comparison of central metallicity depends on the assumed value for the solar oxygen abundance. Choosing $12+\log(\mathrm{O/H})_\odot = 8.69$ (Asplund et al. 2009) returns a H II region central metallicity value of Z = -0.12 ± 0.02. While this value agrees with the BSG result it indicates a small offset (∼0.13 dex) relative to the RSGs. We note, however, that such an offset is also found in the recent work by Kudritzki et al. (2013, 2014) in the spiral galaxies NGC 4258 and 3621 when BSG and T_e H II region metallicities are compared. Depletion of oxygen onto dust in H II regions or temperature fluctuations are discussed as possible reasons. Regardless, given that three completely different methods are applied, the agreement between them is striking.

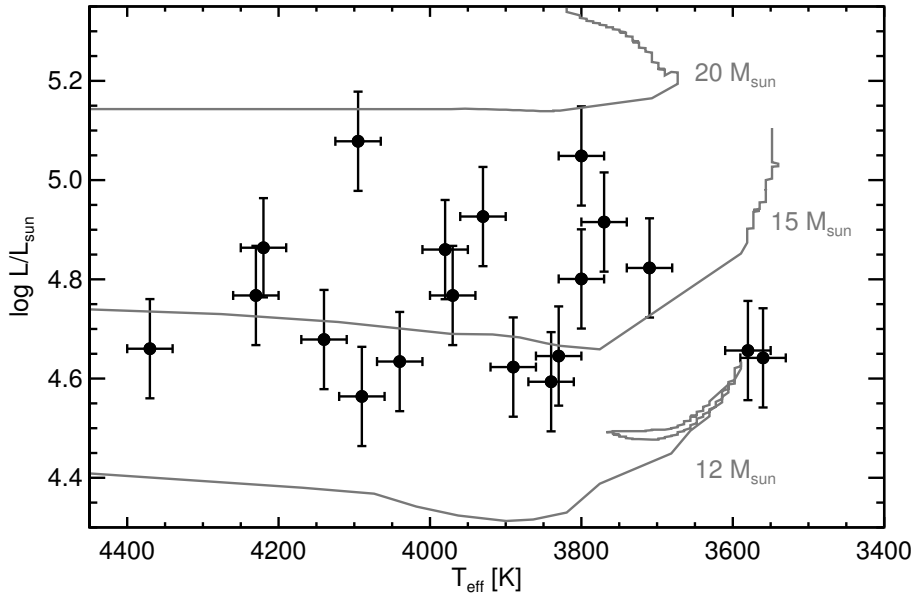

Figure 3.16 Hertzsprung-Russell diagram of program stars for which we have f814W (I) band photometry from Hubble. Temperatures are the parameter fits from our analysis procedure and we calculate luminosities using the bolometric correction recipes for RSGs of Davies et al. (2013).

We construct a Hertzsprung-Russell diagram (HRD) to compare our results with stellar evolution theory. We calculate bolometric luminosities for program stars using f814W (I) band photometry from Hubble and the bolometric correction recipes of Davies et al. (2013). We adopt the distance modulus of $\mu = 26.37$ from the work by Kudritzki et al. (2008). These luminosities are plotted against the effective temperatures from our spectral fit in the HRD of Figure 3.16. We then over plot evolutionary tracks adopting the Geneva database of stellar evolutionary models including the effects of rotation (Meynet & Maeder 2000). We note that all program stars with HST magnitudes fall well within the ranges in temperature and luminosity which are appropriate for RSGs.

Table 3.6. Comparison of NGC 300 Metallicity and Gradient Literature

Study	Central Abundance		Metallicity Gradient		Notes
	dex, metals	12+log(O/H)	r/r_{25}	dex kpc^{-1}	
Kudritzki et al. (2008)	-0.06 ± 0.09	$\cdots$	-0.44 ± 0.06	-0.081 ± 0.011	Blue Supergiants, Metals
Bresolin et al. (2009a)	$\cdots$	8.57 ± 0.02	-0.41 ± 0.03	-0.077 ± 0.006	H II regions, auroral oxygen
This work	$+0.01 \pm 0.04$		-0.45 ± 0.06	-0.084 ± 0.011	Red Supergiants, Metals

Note. — Three independent measurements of the evolution of chemical abundance across the star forming disk of NGC 300. The agreement between BSGs, RSGs, and auroral H II region methods is excellent.

3.3.5 Conclusions

In this section we demonstrate that the J–band RSG technique has reached the precision and accuracy necessary to measure the central metallicity and metallicity gradient in a galaxy beyond the Local Group. By focusing on NGC 300 we are able to compare our results with work on both the BSGs and H II region T_e methods. The agreement between these three techniques, all of which track the present day interstellar medium chemical abundances, is striking. With this test case in hand we provide a strong endorsement for the BSG abundance methods and reinforce the promise of the J–band RSG method developed in this dissertation.

Chapter 4

Super Star Clusters

In this chapter we demonstrate a new method for extending the observational baselines of stellar techniques by exploiting the integrated light of coeval ensembles of stars. In star forming galaxies, such populations exist as super star clusters (SSCs), the result of single bursts of star formation creating a population with a stellar mass of 10^4-10^6 $M_\odot$ in a tight association (Portegies Zwart et al. 2010).

In §4.1 we demonstrate that a discrete jump in the IR colors of SSCs at ages beyond 6 Myrs is caused by the appearance and flux dominance of the RSG members of these clusters by performing population synthesis experiments with synthetic photometry. The simulations agree well with observed near IR colors of SSCs across a range of ages in M83 measured by Bastian et al. (2011, 2012). Indeed, by 7 Myr the population of tens to hundreds of RSGs dominates the near-IR light, providing $\geq$ 90-95% of the J–band flux (Gazak et al. 2013).

We extend this theoretical work in §4.2 by demonstrating how SSCs older than 6 Myr can be used for quantitative spectroscopy and the measurement of metallicity at far greater distances than is possible for single supergiants. We explore the practicality of this spectroscopic technique and the modifications needed to the analysis technique described in Chapter 2.

In §4.3 we present observations of SSCs in three galaxies. We analyze a single SSC in M83 at significantly super-solar metallicity in §4.3.1, followed by a single SSC in the galaxy NGC 6946 in §4.3.2 at sub-solar metallicity. With success on both of these test cases we secured time with the KMOS multi IFU spectrograph on the VLT and observed three SSCs in the distant interacting

Antennae galaxies (NGC 4038/4039). That analysis of SSCs at a distance of over 20 Mpc is described in §4.3.3, and represents a groundbreaking success for the application of supergiant metallicity techniques significantly beyond the Local Group of galaxies.

With this novel method we increase the applicable distance of the J–band RSG technique from roughly 10 to over 35 Mpc using existing instruments and point out that this limiting distance will extend to 70-100 Mpc with the advent of the next generation of 30 meter telescopes.

4.1 Theoretical Color Evolution of Super Star Clusters

In order to study a population of stellar clusters, i.e. to derive cluster dispersal times, relate cluster to star-formation events in the galaxy, or estimate their impact on the surrounding interstellar medium, the ages of individual clusters must be accurately measured. For this purpose, there have been a variety of techniques proposed in the literature to estimate the age of young massive clusters (YMCs), both in the Galaxy as well as in more distant (e.g., starburst) systems.

The techniques can be broadly split into four categories. The first compares the integrated broad/narrow band photometry (e.g., Anders et al. 2004), integrated spectral shape (e.g., Smith et al. 2006), or spectral line strengths (e.g., Trancho et al. 2007) to a grid of models (age, extinction, metallicity) that follow the evolution of the spectral energy distribution of a simple stellar population. The second uses resolved photometry of individual stars in order to make color-magnitude diagrams (as a proxy for the more physical Hertzsprung−Russell diagram) in order to compare with theoretical stellar evolutionary isochrones. This technique has a long history in clusters within the Milky Way (see, for example, Russell 1914) and has recently been extended to massive $> 10^5 M_\odot$ YMCs in nearby galaxies (e.g., Larsen et al. 2011). The third category is to use some feature of the YMC, such as surface brightness fluctuations, the size of the bubble created by the YMC in the surrounding ISM (e.g, Whitmore et al. 2011), or the equivalent width of recombination lines (e.g. Leitherer & Heckman 1995) as a proxy for the cluster age. The fourth and final broad category is the use of specific spectral features that are due to a unique stellar evolutionary phase with known beginning time and duration.

While each technique requires accurate models of stellar evolution and spectral synthesis−of which our understanding and techniques continue to develop−the main difference is observational. Techniques requiring only broadband photometry are observationally efficient, but spectra provide richer sources of information and may warrant the increased exposure time based on the goals of the specific project, i.e. age, metallicity, morphology, etc.

An example of the fourth category of age dating techniques is the use of Wolf-Rayet spectral features (namely the 4650Å emission "bump") in the integrated spectra of young clusters (e.g., Bastian et al. 2006; Sidoli et al. 2006). This type of technique is particularly attractive, as it avoids the complexities of modeling a full stellar population, and focusses on a single stellar evolutionary phase. Here, we introduce a new technique along similar lines, based on the evolution of massive stars. We apply this technique to a photometric catalogue of young massive clusters in M83.

The near-IR flux of RSGs dominates the integrated properties of clusters which contain them. For example, a single RSG of 25 $M_\odot$ at 4000 K emits 25% of the J band flux of a 10^5 $M_\odot$ cluster when initially formed. When the massive stars in such a cluster begin to evolve to the RSG evolutionary phase they emit in excess of 95% of the J–band light of the full population. In this letter we discuss a new technique using near-IR colors as an absolute age indicator for young star clusters. This technique utilizes the initial appearance of RSGs and their strong effect on the integrated properties of their host populations.

Cluster simulations in this chapter utilize a Salpeter initial mass function with mass boundaries of 0.8-100 $M_\odot$.

4.1.1 Observations

The catalogue of clusters in M83 was taken from Bastian et al. (2011, 2012). We refer the reader to those papers for details on the cluster selection, photometry and derivation of cluster properties (ages, masses, extinctions, sizes). Here we briefly outline the methodology adopted. Cluster candidates were selected through visual inspection of *Hubble Space Telescope* (HST) Wide Field Camera 3 (WFC3) V-band images, from a larger list of candidates selected through the automated *SExtractor* (Bertin & Arnouts 1996) routine, to be resolved, centrally concentrated and symmetric

in the inner regions of the cluster profile. The cluster properties were derived through comparison of each clusters U (F336W), B (F438W), V (F555W or F547M), Hα (F657N), and I-band (F814W) magnitudes with simple stellar population models (SSP) using the method described in Adamo et al. (2010). For the SSP models we adopted those of Zackrisson et al. (2011) that include nebular emission, and we adopted a metallicity of 2.5 times solar (Bresolin & Kennicutt 2002; Bresolin et al. 2005).

We emphasize that only optical and UV colors were used in deriving the age of each cluster. Additionally, we only included cluster candidates that had inferred photometric masses above $5 \times 10^3 M_\odot$. This cut was made to limit the effects of a stochastically sampled stellar initial mass function within the clusters. Catalogue clusters near the minimum mass may be affected slightly. In clusters of lower mass, the population of massive stars poorly samples the full probability density distribution of stellar masses such that the appearance of RSGs is skewed to older ages by gaps in the cluster population.

We also make use of the WFC3 Early Release Science images of M83 taken in the F110W (J) and F160W (H) bands. We carried out aperture photometry on these near-IR images, using the cluster catalogue described above, with an aperture radius, background radius and annulus size of 2.5, 4, and 1 pixel, respectively, the same (in arcsec) as was used for measuring the optical colors. The zeropoints were taken from the WFC3 HST Zeropoint website. Aperture corrections were derived from bright and isolated sources (clusters and individual−likely foreground−stars). We applied aperture corrections of 0.53 and 0.59 magnitudes in the F110W and F160W bands. We note that the individual aperture correction for each sources varied, depending on the extent of which the source was resolved. However, the difference between the F110W and F160W bands was always 0.06 (with scatter less than 0.03 mag). Finally, we only included clusters in the sample discussed here that have photometric errors less than 0.1 mag in both near-IR bands.

4.1.2 Age vs. near-IR color

In Figure 4.1 we show the F110W–F160W color vs. the derived age (from optical colors only) for clusters in the inner field (top panel) and outer field (bottom panel). In both fields we see a

bi-modal color distribution, with clusters with ages $\lesssim$ 5 Myr having F110W–F160W colors < 0.4, and older clusters having redder colors. In particular, we note the appearance of a step-like change in colors at $\sim$ 5 Myr. As will be discussed below, this jump is predicted from stellar evolutionary models due to massive stars entering the RSG phase, becoming extremely luminous and red.

The data plotted in Figure 4.1 include the effects of reddening, which are relatively small in the infrared. Using the Cardelli et al. (1989) reddening law and assuming R_V=3.1 we estimate δ(J−H) $\sim$0.09*A_V. This means that a selective increase in A_V by 9 mag is needed for the older clusters exactly at the age of the J−H blue vs. red transition to produce an 0.8 mag jump in the colors. In principle a YMC that is heavily embedded may be extincted enough to appear "old" in the J−H index. However, studies of YMCs in merging galaxies have shown that the deeply embedded stage is relatively short lived, and that nearly all YMCs detected in the radio continuum are also detected in the optical, so this is unlikely to present a strong bias (Whitmore & Zhang 2002). The inclusion of emission line (e.g. Brγ) photometry in such an analysis would allow such deeply embedded clusters, if present, to be detected. On the other hand, the comparison with the SSP models and simulated J-H colors (see below) is, of course, affected by the reddening. We note that the average A_V is about 0.37 and 0.30 for the cluster catalogues of the inner and outer fields, respectively. Thus Figure 4.1 is not strongly affected by reddening. The J−H technique may be inapplicable to cases of high or strongly varied extinction, such as Arp 220 or M82.

4.1.3 The effect of RSGs on near-IR cluster colors

As a massive star evolves into a RSG following the blue supergiant phase it expands and cools while the bulk of emitted flux shifts from optical to near-IR wavelengths. These objects evolve through the main sequence quickly−within 10 Myr, for masses above 15 $M_\odot$−and through the blue supergiant phase even faster, in less than 1 Myr for similarly massive stars (Meynet & Maeder 2000; Kudritzki et al. 2008).

In Figure 4.2 we show the dominance of RSGs on the J-band flux of massive star clusters as a function of age. These simulations are done using Geneva evolutionary tracks with rotation at

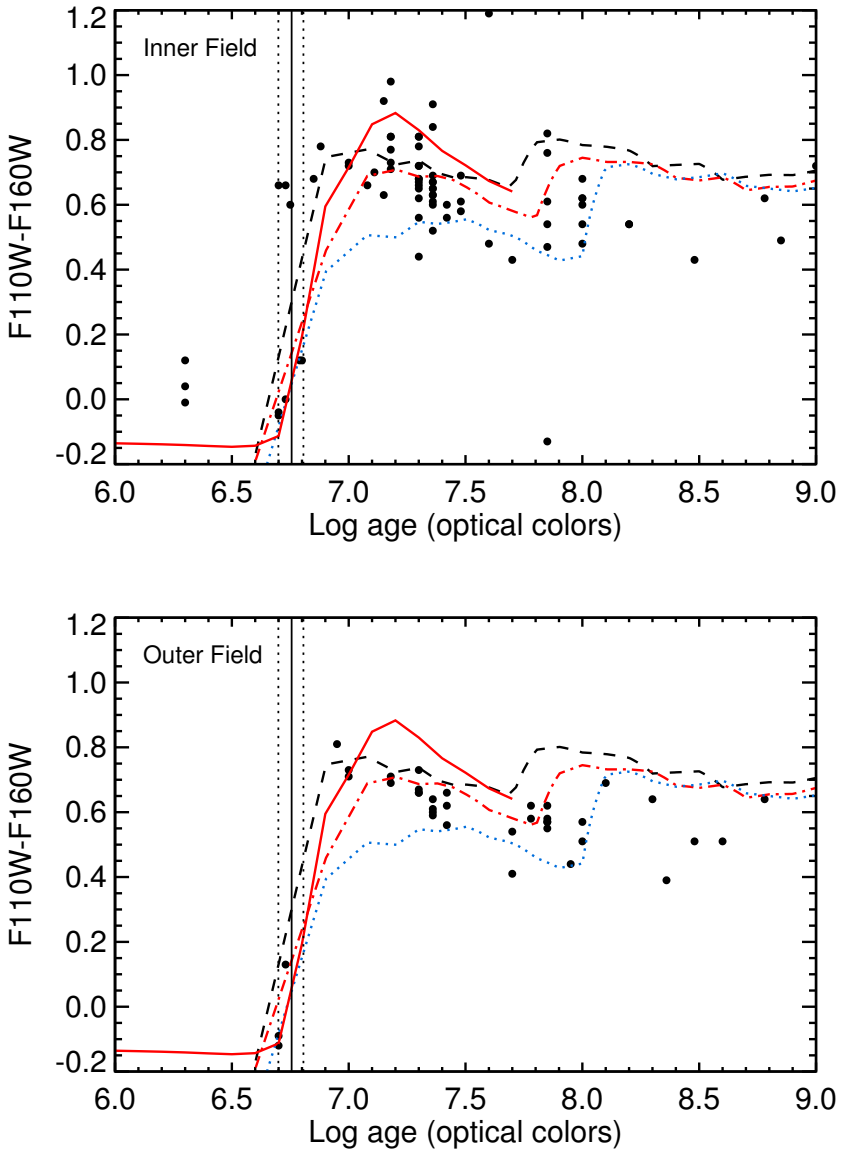

Figure 4.1 The derived ages of the cluster sample (using optical colors) vs. the $J - H$ (F110W−F160W) color for the inner field (top panel) and outer field (bottom panel) fields of M83 (Bastian et al. 2011, 2012). These colors have not been dereddened. The solid red curve displays our theoretically calculated color evolution using Geneva evolutionary tracks and colors calculated from Kurucz models for the main sequence and MARCS models for RSGs. The other curves are obtained with the GALEV SSP code for twice solar (dashed black), solar (red dashed-dotted), and half solar (blue dotted) metallicity. Note that the GALEV simulations begin at cluster age of 6.6 [log years] while our simulations end at 7.7 [log years]. The solid and dotted vertical lines show the appearance of RSGs and uncertainty as calculated in this work.

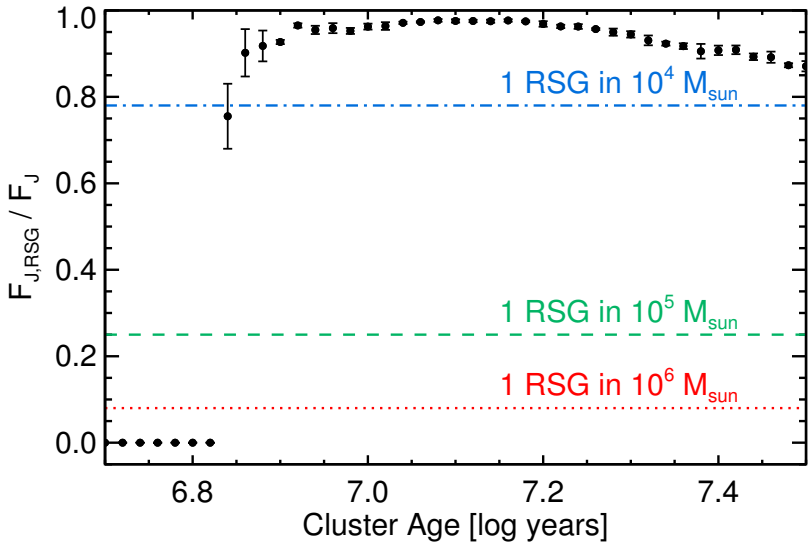

Figure 4.2 The J-band flux contribution of RSGs in a simulated super star cluster of 10^5 $M_\odot$ using Geneva evolution tracks at solar metallicity including stellar rotation. Error bars show estimated scatter from ten simulated clusters using a Salpeter initial mass function. Horizontal lines represent the flux contribution from a single 25 $M_\odot$ 4000 K RSG injected into simulations of zero age clusters with masses of 10^4 $M_\odot$ (blue, dash-dotted), 10^5 $M_\odot$ (green, dashed), and 10^6 $M_\odot$ (red, dotted).

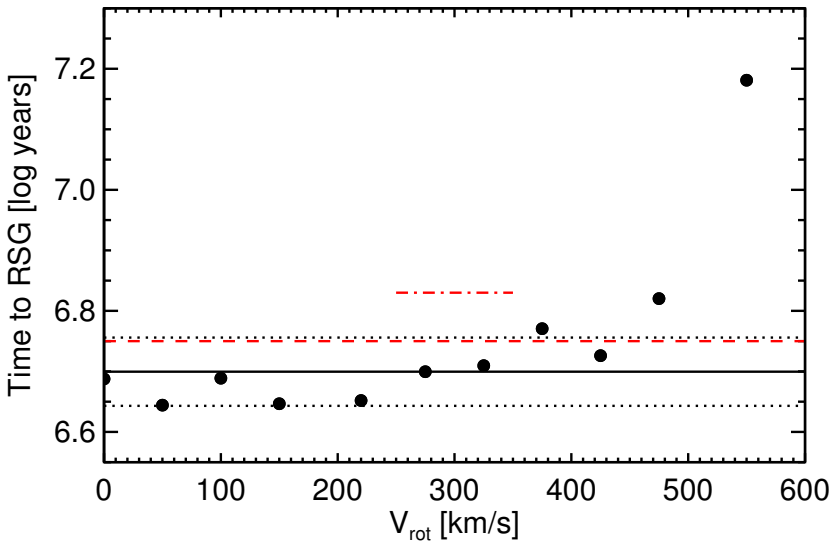

Figure 4.3 Effects of rotation on the mass and age of the first RSGs in a simple stellar population. Points represent the first appearance of RSGs as a function of initial rotational velocity, V_{rot} (Brott et al. 2011). The solid and dotted black lines show the average and scatter in these initial ages excluding the point at V_{rot} = 550 [km/s]. The red dashed line marks the appearance of RSGs in Geneva evolution tracks without rotation, and the red dash-dotted line Geneva with rotation included at $V_{rot} = 0.4\ V_c$ ($\sim$ 250-350 km/s for the initial population of RSGs). Utilizing the three sets of stellar evolution models, the initial appearance of RSGs occurs at 5.7 $\pm$ 0.8 Myr.

solar metallicity. The work clearly shows that the appearance of RSGs marks a significant change in the observational properties of the integrated light of the cluster in the near-IR.

The appearance of the first RSG in a young massive cluster initializes a hysteresis effect in which near-IR color reddens significantly and remains red as increasing numbers of less luminous stars evolve to red evolutionary phases. As a single RSG affects the near-IR colors of a massive star cluster in this way, the measurement of that change in color represents an absolute age indicator.

Observations show that 50-60% of massive stars form and evolve as binaries (Sana & Evans 2011; Sana et al. 2013). The technique presented in this letter requires that the age of the first RSGs remain stable (Figure 4.3) and that the RSGs dominate the near-IR flux of the YMC (Figure 4.2). Eldridge et al. (2008) argue that, for a reasonable distribution of binary separations and mass ratios, the mean lifetime of RSGs may be reduced by a factor of 2 to 3 compared with the predictions of single-star models. Evolution towards the RSG phase is unaffected. The most extreme effect of

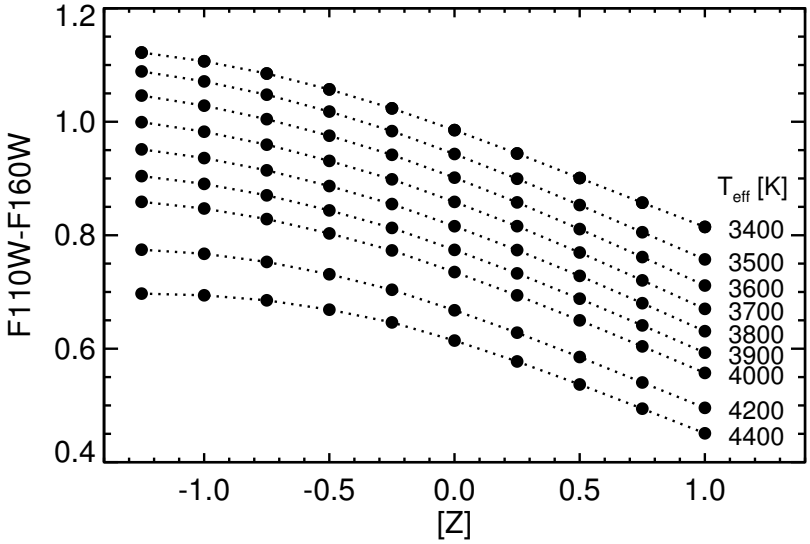

Figure 4.4 Color evolution of RSGs in temperature and metallicity used in this work. Colors are measured using a new grid of MARCS models and TURBOSPECTRUM (Alvarez & Plez 1998; Plez 2012).

binarity on the stellar population is therefore to remove ∼60% of the RSGs, to be replaced by blue supergiants. Though this will cause the YMC to be fainter in the near-IR, the RSGs' contribution to the cluster's total near-IR flux decreases by only a few percent, and the sharp jump in J-H color for ages of $\gtrsim$5Myr remains. Hence, the impact of binarity on our results is merely to increase stochasticity effects in low-mass clusters.

4.1.4 Age Dating Clusters Using the Presence of RSGs

Our simulations localize the color break in clusters with and without RSGs to 5.7 ± 0.8 Myrs by weighting multiple techniques present in the literature to measure the timescale of formation for RSGs.

The main uncertainty inherent in the RSG age dating technique arises from processes which affects stellar evolution. Here we describe the role of stellar rotation, which affects the maximum stellar mass which evolves to the RSG phase. We utilize the Brott evolutionary models for this discussion as they cover a range of metallicities and rotation (Brott et al. 2011). Figure 4.3 shows

the evolution of the appearance of the first RSG in the Brott evolution tracks as a function of initial stellar rotation, as well as the appearance of RSGs in two sets of Geneva evolution tracks with and without rotation at solar metallicity (Meynet & Maeder 2000).

The Brott models show a slow increase in the time to the appearance of a RSG which evolves with a decreasing mass of the initial RSGs. This effect is due to an increasing size in the hydrogen burning core of fast rotating stars. At high rotational velocities, stars evolve as if they were more massive, and as such explode in core collapse supernova before reaching the RSG phase. At rotation velocities above 500 km/s this effect becomes significant, lowering the mass of the first RSG to $\sim$15$M_\odot$ from the consistently 30-40 $M_\odot$ initial RSG population for less extreme rotation velocities. Assuming a spread of velocities in a simple stellar population, we drop the 550 km/s case as all stars would not be expected to rotate with such extreme velocities and calculate an age for the appearance of RSGs to 5 $\pm$ 0.7 Myr from the Brott models. The Geneva tracks yield slightly longer delays before RSG appearance of 5.6 Myr for tracks without rotation and 6.9 Myr for tracks with rotation. The Geneva group models with rotation adopt initial rotation speeds of V_{rot}= 0.4V_c. Weighting these three measurements we measure a time of RSG appearance of 5.7 $\pm$ 0.8 Myr.

As discussed in §3.2, the effects of these initial populations of RSGs on the near-IR cluster colors are expected to appear as a significant hysteresis jump allowing for a clear differentiation between young "blue" clusters and "red" clusters in which massive stars have evolved into RSGs and dominate the near-IR properties. Our cluster catalogue shows exactly such evolution in the HST J-H (F110W−F160W) color as plotted in Figure 4.1. The ages of these clusters have been calculated by an independent method utilizing optical colors (see §2), and the work in this letter shows that a clear age differentiation may be measured using only near-IR colors. We model this effect by simulating clusters using the Geneva stellar evolution models including rotation. Cluster colors are calculated at every time step with synthetic photometry of cluster stars, utilizing the Kurucz grid of spectral energy distributions for main sequence stars and a new grid of MARCS models calculated for the critical RSG population (Gustafsson et al. 2008). In Figure 4.4 we plot the new grid of colors applied to RSGs in our synthetic cluster calculations. This technique successfully

recreates the form and scale of the observed effect in M83 (Figure 4.1). We recover nearly identical results using the GALEV code to model our simple stellar populations over a range of metallicities from half to twice solar, and note that the effect is recovered in similar passbands using starburst99 (Kotulla et al. 2009; Leitherer et al. 2010).

We note, however, that SSP calculations at metallicities lower than half solar with different sets of evolutionary tracks give conflicting results with regard to the steepness of the blue to red (J−H) transition. This is obviously the result of a different treatment of mass-loss and rotational mixing. A careful observational investigation of stellar clusters in low metallicity environments will be worthwhile in this regard.

Studies such as Sharma et al. (2007) have found a significant spread in the age of the stellar population in young associations. Naylor (2009) shows that a systematic difference in age determination between young main sequence and pre main sequence stars can explain the apparent spread in ages. Regardless, our catalogue has been specifically designed to exclude sources such as the one in Sharma et al. (2007). For those true YMCs which remain, no evidence for such age spreads in the massive star population have been found (Kudryavtseva et al. 2012).

4.1.5 Conclusions

In this section we presented a new absolute age indicator for young massive star clusters using J−H color which can be used to determine if a massive star cluster is older or younger than 5.7 ± 0.8 Myr. Because this technique requires only near-IR photometry it can be used well beyond the HST era when both space and ground based telescopes move to the near-IR. The technique can be used with spectroscopic data as well and we show this in the following sections. While this age dating method is shown to work well in the range between half to twice solar metallicities, a careful observational investigation of its applicability at significantly lower metallicity is suggested, since present evolutionary tracks give conflicting results in this low metallicity domain.

4.2 Theoretical Spectral Evolution of Super Star Clusters

In the next step, we demonstrate how the metallicities of young super star clusters can be measured using novel spectroscopic techniques in the J–band. As shown in the previous section, the near-infrared flux of super star clusters older than ∼6 Myr is dominated by tens to hundreds of red supergiant stars. This means that the J–band spectra must also be dominated by the RSGs.

4.2.1 Synthetic Super Star Clusters

In §3.1.6 we synthesized an integrated J–band cluster spectrum by combining the individual spectra of a population of RSGs in the galactic double cluster h and χ Persei. We demonstrated that the quantitative analysis of the integrated spectrum yields a metallicity consistent to the mean metallicity of the individual RSGs. This is the starting point for the population synthesis experiment described in this section.

Simulations presented in §4.1 (Gazak et al. 2013) successfully recreated observed trends in the near infrared colors of SSCs based on the evolution of the first RSG members. RSGs contribute 90-95% of the near-IR flux emitted by young SSCs older than ∼6 Myr. Now we expand on those photometric results and composite cluster test by simulating the full spectra of SSCs as a function of age. Here we use the same methodology as §4.1 to derive theoretical stellar populations of a 10^5 $M_\odot$ SSC from 1-22 Myr. Notably, we assume a Salpeter initial mass function with mass boundaries of 0.8-100 $M_\odot$and evolve the theoretical cluster using the Geneva stellar evolution tracks which include effects of rotation (Meynet & Maeder 2000).

At each time step we construct a theoretical spectral energy distribution (SED) at a resolution of R=10,000 using theoretical SEDs from the Pollux database[1] (Palacios et al. 2010). This database draws from three sets of 1D LTE synthetic spectra, including CMFGEN (Hillier & Miller 1998), ATLAS12 using the Kurucz stellar atmospheres (Kurucz 2005), and TURBOSPECTRUM calculations using MARCS atmospheres (Plez 2012; Gustafsson et al. 2003). For stellar parameters typical of

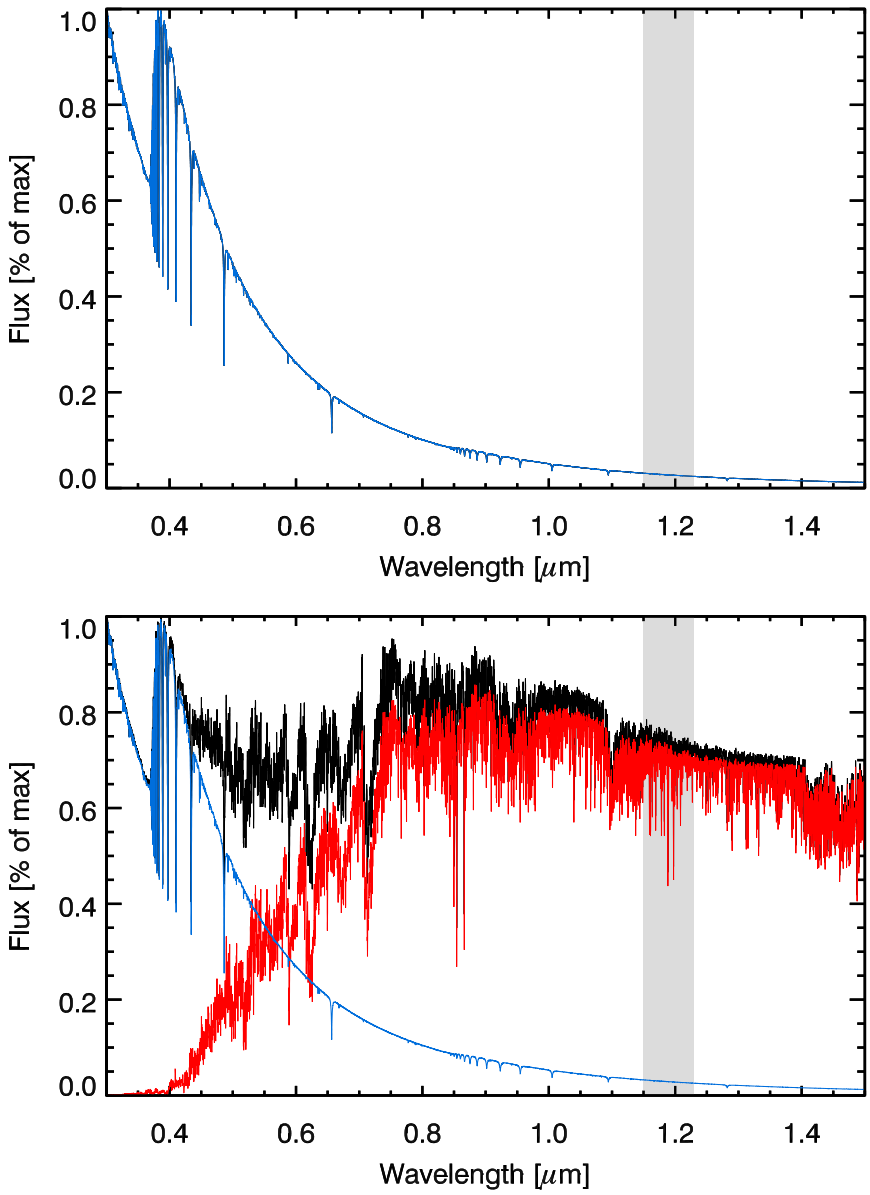

Figure 4.5 Theoretical spectra for a 10^5 $M_\odot$ super star cluster after 5 Myr (left panel) and 15 Myr (right panel). Black spectrum represents the full SSC SED, blue represents the main sequence and blue supergiant stars, and red plots flux due to red supergiant members. The J–band is highlighted in gray.

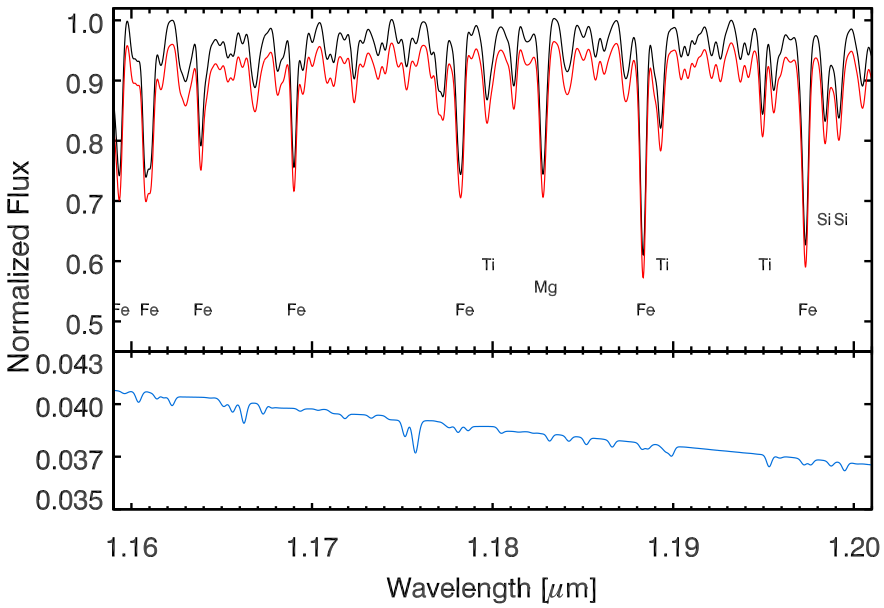

Figure 4.6 Theoretical J–band spectrum of a 15 Myr old, 10^5 $M_\odot$ super star cluster. Black spectrum plots the SSC spectrum normalized to unity in the J–band, red shows the contribution of the red supergiants and the lower panel provides a zoomed view of the 5-6% level of the blue spectrum which represents the main sequence and blue supergiant stars.

RSGs we supplant the latter with our own NLTE theoretical spectra in the J–band (Bergemann et al. 2012, 2013). Solar metallicity is assumed.

In Figure 4.5 we plot a synthetic SED from 0.3-1.5 microns at 5 Myr and 15 Myr (before and after the evolution of the first massive stars into RSGs which begins at roughly 7 Myr). The evolution of the first RSGs have an overwhelming effect on the near IR SED, wholly dominating the flux of the cluster. We plot two panels showing just the J–band in Figure 4.6.

4.2.2 Analysis Techniques and Tests

We test the hypothesis that a J–band spectra could yield the Z abundance of that cluster by applying our analysis method (See chapter 2) to the synthetic spectra of Figure 4.6 between ages of 8 and 22 Myr. For the model SSC spectra at R=3500 we recover Z consistent with solar metallicity and with measurement errors of 0.10 to 0.14 (See Figure 4.7). When we subtract a flat spectrum

[1]Operated at LUPM (Universit Montpellier II - CNRS, France) with the support of the PNPS and INSU. http://pollux.graal.univ-montp2.fr

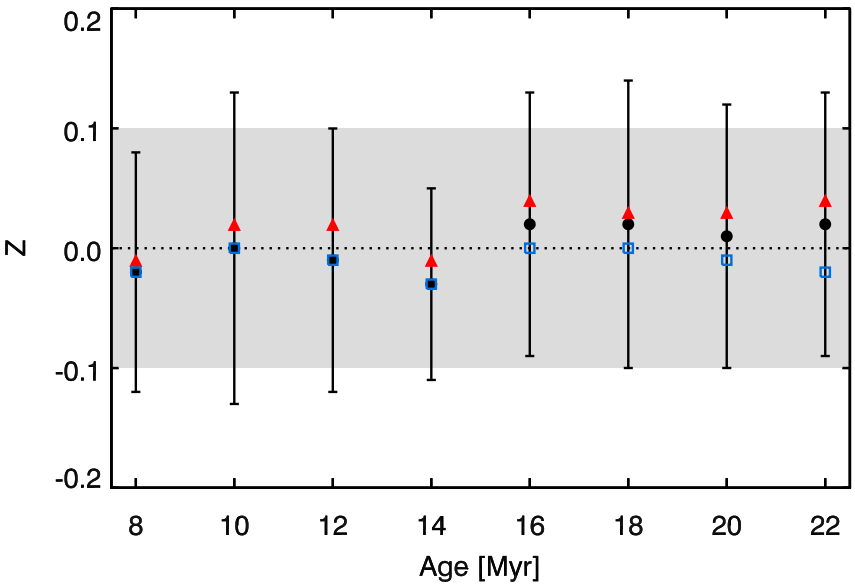

Figure 4.7 Metallicities extracted from synthetic SSC spectra as a function of age. Black circles show values extracted from the spectra when a 5% flat contaminative flux is removed from each spectra , red triangles are a result of the RSG population alone, and blue squares show metallicities extracted from the full spectra. Error bars on the black circles are consistent for each of the three types of measurement. The gray zone is the expected region of uncertainty for a single solar metallicity red supergiant analyzed with the method used in this letter and initially presented by Davies et al. (2010) and Gazak et al. (2014b).

that is 5% of the total flux (to simulate the removal of the "main sequence" contribution), the measured metallicities increase, remaining consistent with solar.

We experiment with the effect of ∼5-10% contaminative flux from the remaining stellar flux of the SSC (Gazak et al. 2013). This is accomplished by assuming a flat spectral dilution and removing 5% and 10% of the median flux of our observed spectra. The effect is to deepen the absorption features−it is in the depths of strong lines that the flat spectrum contributes the largest percent flux. We repeat our fitting procedure after scaling out 5% of the median flux. These adjusted spectra yield consistent measurements of Z; measurement uncertainties dominate the shift in metallicity due to deeper absorption features.

4.3 Super Star Cluster Observation Campaign

Our technique is designed to harness the integrated light of a SSC and produces accurate metallicities for new observations in galaxies above (M83) and below (NGC 6946) solar metallicity. In M83 we find Z = +0.28 ± 0.14 dex using a moderate resolution (R∼3500) J–band spectrum and in NGC 6496 we report Z = –0.32 ± 0.20 dex from a low resolution spectrum of R∼1800.

4.3.1 M83

Observations of M83-1f-117 (α=13$^{\rm h}$37$^{\rm m}$02$^{\rm s}$, δ=−29°52′13″) were obtained using ISAAC/VLT (Moorwood et al. 1998) on the night of 2012 March 13 under the ESO programme 089.D-0750(A) (P.I. Bastian, N). We employed the 1″.0 slit width with a central wavelength of 1.17 μm and integrated on source for two hours using an ABA nod pattern. We observed a B-type star with a similar airmass as a telluric standard.

The spectra were reduced following the methodology outlined in Davies et al. (2012). Briefly, this reduction consists of the subtraction of nod pairs, flat-fielding, rectification to correct for distortion in the spatial and dispersion directions, sky subtraction, and cosmic-ray removal. The observed spectrum is plotted in Figure 4.8.

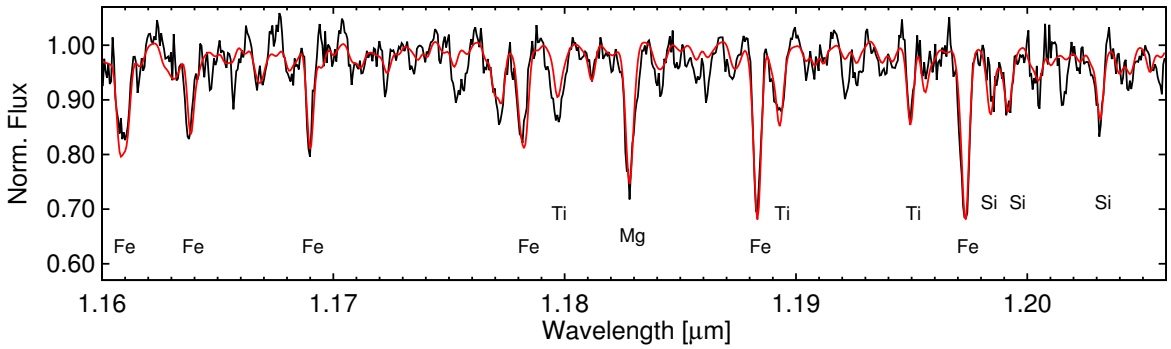

Figure 4.8 Observed spectra of the young super star cluster M83-1f-117 (black). The spectrum is overplotted with a best fitting red supergiant synthetic spectrum (red dashed with gray) in the spectral window analyzed. The critical diagnostic lines of Fe I, Ti I, Si I, and Mg I are marked. Spectral fitting is carried out over Fe I, Ti I, Si I, and the Mg I line is included only in the display model to show the preliminary results of new NLTE corrections to this diagnostic feature.

Multiple investigations of M83's chemical enrichment using both "direct" and "strong line" H II methods have found abundance gradients across the inner and outer disk of the galaxy (Bresolin & Kennicutt 2002; Bresolin et al. 2005, 2009b). While plagued by the biases and uncertainties discussed in §1.3, those papers produce lower limits for the [O/H] enrichment in the inner disk of M83 of 1.6× solar and admit that the values require refinement. In particular, Bresolin et al. (2009b) find that two common calibrations of the H II region method on the same dataset return identical slopes for the metallicity gradient but the measurements of the overall metallicity level vary by 0.47 dex−a factor of nearly three. Furthermore, early work on H II regions returned values of 2-10× solar oxygen abundance (Dufour et al. 1980). While current work settles around more modest values of 1.5-2×, it is clear that the calibration of H II region metallicities exceeding solar remains problematic.

In Table 4.1 we tabulate the parameters measured from our spectra corrected for a flat 5% flux contamination. By applying our method for extracting metallicities from the J–band spectra of RSGs we measure a disk metallicity of 1.9× solar (Z = +0.28 ± 0.14) for M83. This value is consistent with H II region measurements by Bresolin et al. (2005) who report a metallicity from H II region auroral lines in the inner disk of [O/H] = 1.78× solar. This excellent agreement provides

Table 4.1. NLTE Parameters for M83 and NGC 6946 Super Star Clusters

Param	M83-1f-117	NGC6946-1447
T_{eff}	3540 ± 80	3940 ± 100
log$g$	+0.48 ± 0.18	+0.10 ± 0.15
Z^a	+0.28 ± 0.14	−0.32 ± 0.20
ξ	3.1 ± 0.25	3.0 ± 0.25
R_{eff} $[\lambda/\delta\lambda]$	3500 ± 50	1800 ± 50

Note. — Parameter fits to the observed spectra.

compelling evidence that the SSC J–band technique is reliable and has an enormous potential for extragalactic applications.

4.3.2 NGC 6946

NGC6946-1447 (α=20^{h}34^{m}52^s, δ=60°08′14″) was observed on 2011 August 3 and 2011 October 12 with the near-IR medium resolution SpeX spectrograph mounted on the 3−meter NASA InfraRed Telescope Facility (IRTF) on the summit of Mauna Kea (Rayner et al. 2003). SpeX was set up in short wavelength cross-dispersed mode with a 0″.3 slit. The data were reduced and telluric-corrected using the IDL spectral extraction package Spextool (Vacca et al. 2003; Cushing et al. 2004). The observed spectrum is plotted in Figure 4.9.

Measurements of the central abundance and gradient of NGC 6946 suffer from the same setbacks of the H II region method. Using two empirical calibrations, Moustakas et al. (2010) measure a central metallicity and metallicity at the isophotal radius R_{25} (Z_0, $Z_{R_{25}}$) of 3.0× solar and 1.5× solar for the calibration of Kobulnicky & Kewley (2004) and 0.6× solar and 0.4× solar based on an alternate calibration of Pilyugin & Thuan (2005). Cedrés et al. (2012), using the same two calibrations, measure Z_0, $Z_{R_{25}}$ of 3.4 and 1.7× solar for one and of 0.8 and 0.3× solar for the other. In this case three of the four measured gradients are consistent but the offsets in central metallicity between calibrations are factors of four to five (0.63-0.68 dex). We targeted the SSC

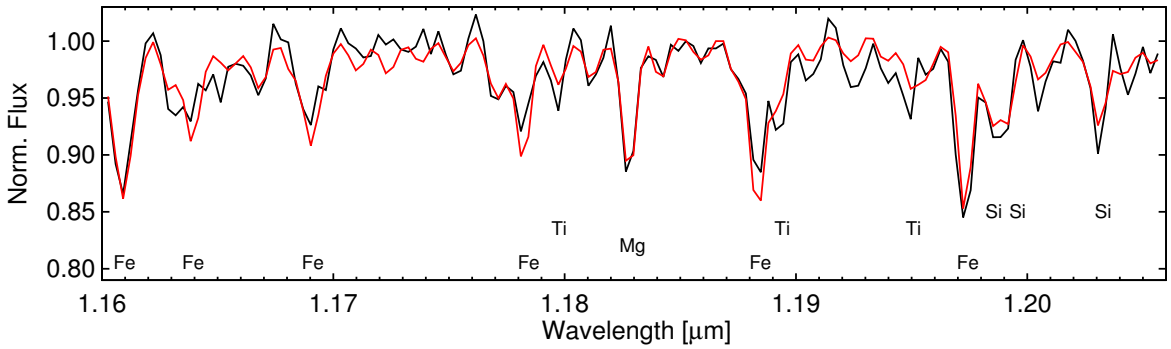

Figure 4.9 Observed spectra of the young super star cluster NGC6946-1447 (black). The spectrum is overplotted with a best fitting red supergiant synthetic spectrum (red dashed with gray) in the spectral window analyzed. The critical diagnostic lines of Fe I, Ti I, Si I, and Mg I are marked. Spectral fitting is carried out over Fe I, Ti I, Si I, and the Mg I line is included only in the display model to show the preliminary results of new NLTE corrections to this diagnostic feature.

NGC 6946-1447 because it has been the target of a careful, high-resolution analysis: Larsen et al. (2006) use R=25,000 H and K spectra and a proprietary spectral synthesis code to measure [Fe/H] $= -0.45 \pm 0.08$ (0.35× solar) and $[\alpha/\mathrm{Fe}] = +0.22 \pm 0.11$.

With our method we measure a metallicity of ∼0.5× solar ($Z = -0.32 \pm 0.20$). Our measurement agrees within 1σ to the published value in Larsen et al. (2006), but we note that the resolution of our NGC 6946-1447 spectrum is less than ideal. Even with this observation at modest R ∼1800 we can claim that the disk of this galaxy is significantly sub-solar in metallicity, something that H II region methods cannot do without an arbitrary choice of calibration. Still, the J–band SSC method is better suited to spectral resolutions above R=2500. It is important to note that Larsen et al. (2006) also find a significant enrichment in α-elements relative to iron. Our assumption of a solar α/Fe will then skew our measured Z to higher metallicities. Assuming the SSC does have a super-solar α/Fe, the silicon and titanium lines in our models will be globally too shallow relative to iron. In this case the best global fit to the spectrum using our grid will require a model with higher Z and may explain the difference between this work and Larsen et al. (2006).

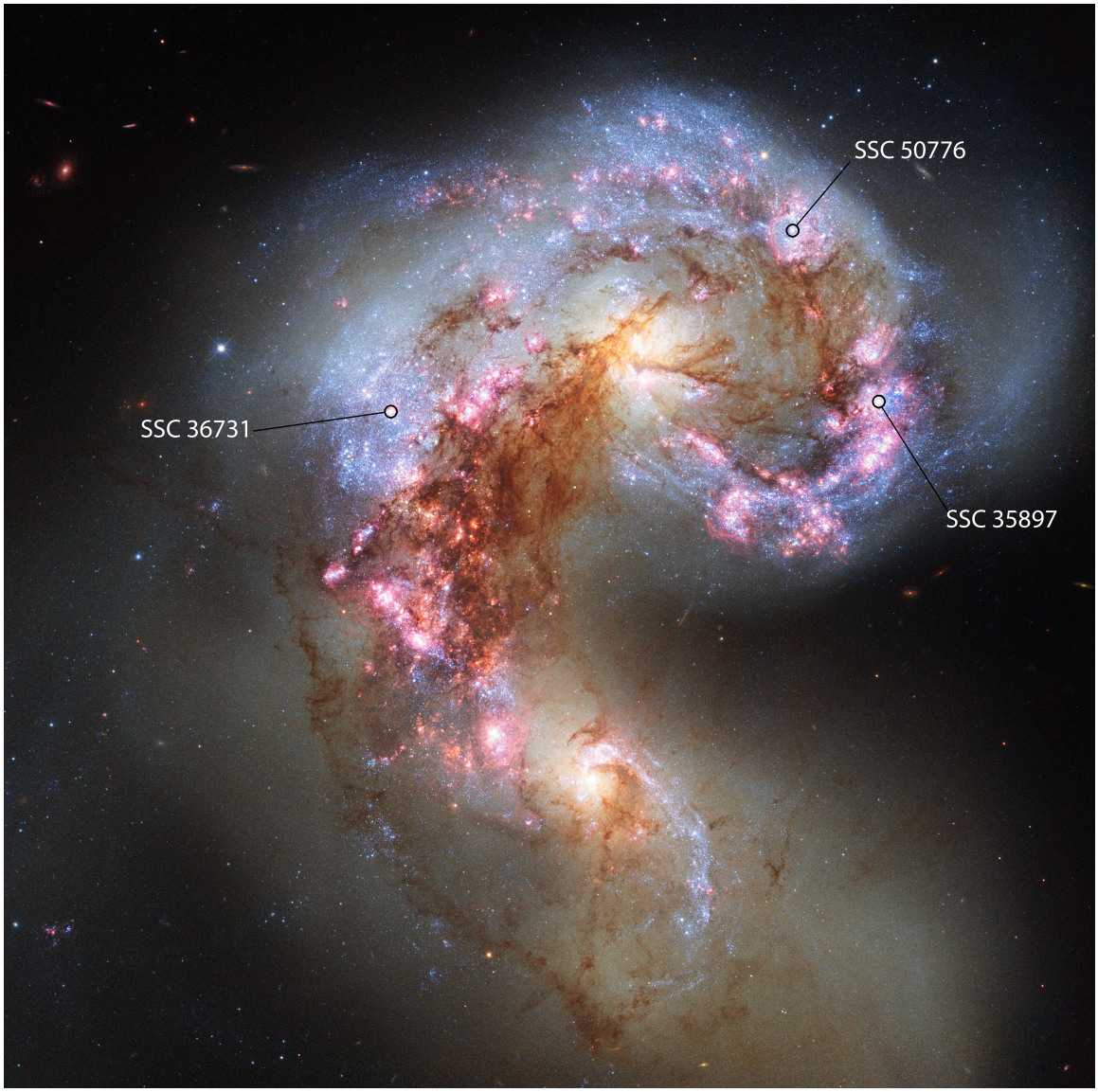

Figure 4.10 Central region of the merging Antennae system. The locations of the three SSCs observed for §4.3.3 are marked and labeled. See Figure 4.11 for the spectra and model fits and Table 4.2 for the parameters of these clusters. Photo credit: ESA/Hubble & NASA.

4.3.3 SSCs in the Antennae

The Antennae galaxies (NGC 4038/4039) are the nearest example of a pair of merging gas-rich disk galaxies. This proximity makes the system a key target for the understanding of the dynamics of galaxy mergers, a critical test case for modeling galaxy evolution during merger, and a compact example of the extremes of astrophysics. The bulk of the measurements on the distance to the Antennae settle around 20 Mpc, with the most recent measurement of 22 $\pm$ 3 Mpc (see Schweizer et al. 2008 and the discussion therein). Outlier measurements which place this interacting pair closer or farther (most recently a measurement of 13.3 Mpc by Saviane et al. (2008)) have been largely discredited as misinterpretations. Bastian et al. (2009) used photometry and optical spectroscopy to measure the metallicities of a number of SSCs in the Antennae by calculating photometric ages and then modeling the absorption and/or emission line spectra with simple stellar population models. That study returns values roughly solar, ranging from Z = -0.05 to $+0.11$ with uncertainties ranging from ± 0.1 to 0.4 dex. The methods used are complex and rely on spectroscopy and photometry across optical wavelengths.

The Antennae system, while nearby for an interacting galaxy, will be far past the limits of individual supergiant metallicity techniques until the construction of the next generation of 30 meter class telescopes. By presenting measurements of the global metallicity of three SSCs in Antennae we provide a powerful demonstration of the J–band technique and provide an IR method as an alternate to that presented by Bastian et al. (2009).

We selected seven SSCs for study from the catalogue presented by Whitmore et al. (2010) as having proper magnitudes, masses, and ages to be dominated by RSGs as the method requires. We used HST imaging to select only visually compact and isolated clusters so as to minimize the effects of blending with other active regions of star formation. On the nights of 2014 April 7 and 8 we observed those SSCs in the Antennae galaxies with KMOS on the VLT. The total on target integration time was 100 minutes per target, with roughly 120 minutes of overhead to observe sky frames, telluric standard stars, and calibration frames. The weather was clear and stable with median seeing of $\sim 1''$ across both nights.

Table 4.2. Catalog and Metallicities of Antennae Super Star Clusters

Target	Right Ascension hh:mm:ss	Declination dd:mm:ss	m_J	Z [dex] [dex]
50776	12:01:51.324	−18:51:46.1	16.41	+0.02 ± 0.13
36731	12:01:55.917	−18:52:11.5	17.30	+0.03 ± 0.14
35897	12:01:50.372	−18:52:12.7	15.80	−0.11 ± 0.16

We find that four of the objects are RSG dominated SSCs and present RSG spectra in the J–band, although for one object the SNR is too low for quantitative study. The remaining three objects present emission lines, placing them in an early nebular stage of development.

Analysis of the three remaining SSC J–band spectra yield metallicities which are roughly solar (see Table 4.2). These results are in good agreement with the work done by Bastian et al. (2009). By requiring only a single observation (and not the photometry and spectroscopy needed for earlier work), and by sampling the SSCs at the peaks of their spectral energy distributions we see the potential of the J–band technique. Here we apply only moderate assumptions to stellar spectroscopy and return accurate abundance measurements at a distance of 20 Mpc. This is the first successful application of the J–band technique at such a large distance and demonstrates the enormous astrophysical potential of this new method.

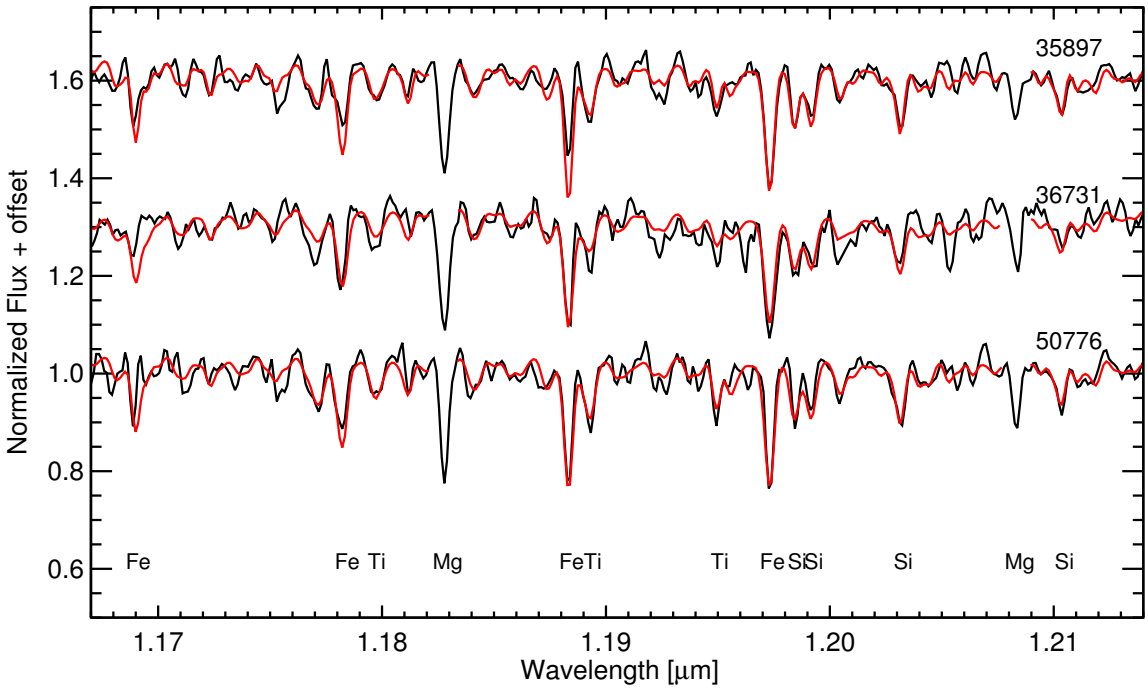

Figure 4.11 Three Antennae J–band super star cluster spectra over plotted with best fit models. The derived metallicities are roughly solar (see Table 4.2). NLTE corrections are not yet available for lines of Mg I, so they are masked out in this analysis.

Chapter 5

Conclusions

A new spectroscopic method has been developed and carefully tested which, with the advent of the next generation of 30 meter class telescopes will enable us to study the chemical evolution of galaxies through the spectroscopy of individual stars out to the Coma cluster of galaxies. By applying the method to the integrated light of Super Star Clusters (SSCs) we will be able to reach distances of a factor of ten farther. This dissertation provides the opening sentences of a new chapter of astrophysical research.

5.1 The J–band Method

In this dissertation we have described a novel method of extracting extragalactic metallicities in the disks of star forming galaxies by conducting low resolution near-IR quantitative spectroscopy of red supergiant (RSG) stars. We show how the technique can be applied with impressive precision down to resolutions below $\lambda/\delta\lambda$ of 3000. After proving this capability we were able to apply the technique to the RSG populations of the Milky Way, M31, and NGC 300 using, in the latter two cases, recently commissioned multi object spectrographs on Keck and VLT. The promising returns of those observational campaigns place the J–band technique in an ideal position to return metallicities of individual RSGs at distances of up to 10 Mpc.

We further extended the capabilities of the J–band technique out to a distance of 20 Mpc by proving its applicability to the integrated light spectra of super star clusters (SSCs) of the proper age. We also demonstrate a method of photometrically selecting those SSCs for which the method

is useful. These clusters contain tens to hundreds of RSGs after a certain age and, beyond being the brightest objects in their host galaxies, can extend the baseline over which the J–band is useful by roughly the square root of the number of RSGs, or up to a factor of ten in distance.

5.2 Future Perspectives

The success of the J–band RSG technique presented in this dissertation is truly just a hint of what science this method will allow. In the coming decades, significant investments in both the instrumentation and theory will provide a boost to this already powerful technique, and allow the investigation of stars and clusters out to clusters of galaxies.

A trend towards near-IR instrumentation is already evident on the 8 meter telescopes, and we have the privilege to present applications using both of the premier newly commissioned near-IR spectrographs, KMOS on the VLT and MOSFIRE on Keck. These spectrographs return resolutions of between 3200 and 3500 and operate in the spectral windows of J, H, and K where atmospheric absorption does not overwhelm the night sky. As we enter the era of 30 meter class telescopes, astronomical instrumentation will continue to skew heavily towards the infrared with both ground and space based missions.

As the era of Hubble comes to an end and JSWT and the new extremely large telescopes become available, many of the tools and techniques used to age date and study super star clusters will become−at least temporarily−obsolete. This was part of the motivation for Gazak et al. (2013), in which we defined a new criterion for measuring the ages of SSCs using only near-IR colors. Such techniques will replace those currently in place which require observations in the optical wavelengths.

Instruments in this near future will require the advantages of adaptive optics, including multi-conjugate AO for multi object spectrographs. These AO systems perform with enhanced efficiency in the near-IR where wavelengths are longer and the stress on a deformable mirror is reduced.

While significant science has been done with RSGs in the optical regime, observing these objects near their flux maxima is obviously advantaged. We extend the observational baseline significantly

for individual supergiant stars and, in the case of SSCs, we require the flux dominance of these stars over their progenitor blue supergiants to disentangle the two populations and conduct the spectroscopic J–band analysis at all.

The theoretical aspects of this project are also continuing and future applications of theory to observations will continue to increase the returns from observations.

We met with success using the 1D LTE MARCS models with synthetic spectra computed using TURBOSPECTRUM. Still, there is plenty of room for improvement both in the evolution and structure of RSGs and in the computation of model spectra. Already NLTE corrections are available for the strongest atomic features of Fe I, Si I, and Ti I in the J–band, and for our analysis we use grids of spectra with these corrections (Bergemann et al. 2012, 2013). That work is being expanded to lines of Mg I, the final major diagnostic of the J–band. There is some promise that magnesium will be especially sensitive to stellar gravity and thus further tighten the precision in our extractions of stellar parameters. The researchers doing this type of work have met with great success in securing steady funding and are building up research teams to promote the observational and theoretical sides of this work.

While 3D models of RSGs have appeared in the literature, these remain too computationally expensive to produce large grids, and while additional work is needed to understand the poor replication of "micro turbulence" seen in actual RSGs, this work is poised to enhance the field. As this type of work is unleashed on the next generation of telescopes, capable of observing individual RSGs in entire clusters of galaxies, so too will the theoretical models calculated in 3D NLTE become available. The future is, as they say, bright.

References

Adamo, A., Östlin, G., Zackrisson, E., Hayes, M., Cumming, R. J., & Micheva, G. 2010, MNRAS, 407, 870

Alvarez, R., & Plez, B. 1998, A&A, 330, 1109

Anders, P., Bissantz, N., Fritze-v. Alvensleben, U., & de Grijs, R. 2004, MNRAS, 347, 196

Asplund, M., Grevesse, N., Sauval, A. J., & Scott, P. 2009, ARA&A, 47, 481

Aufdenberg, J. P., Hauschildt, P. H., Baron, E., Nordgren, T. E., Burnley, A. W., Howarth, I. D., Gordon, K. D., & Stansberry, J. A. 2002, ApJ, 570, 344

Bastian, N., et al. 2011, MNRAS, 417, L6

—. 2012, MNRAS, 419, 2606

Bastian, N., Emsellem, E., Kissler-Patig, M., & Maraston, C. 2006, A&A, 445, 471

Bastian, N., Trancho, G., Konstantopoulos, I. S., & Miller, B. W. 2009, ApJ, 701, 607

Bergemann, M., Kudritzki, R.-P., Plez, B., Davies, B., Lind, K., & Gazak, Z. 2012, ApJ, 751, 156

Bergemann, M., Kudritzki, R.-P., Würl, M., Plez, B., Davies, B., & Gazak, Z. 2013, ApJ, 764, 115

Bergemann, M., et al. 2014, ArXiv e-prints

Bertin, E., & Arnouts, S. 1996, A&AS, 117, 393

Bresolin, F., Gieren, W., Kudritzki, R., Pietrzyński, G., & Przybilla, N. 2002, ApJ, 567, 277

Bresolin, F., Gieren, W., Kudritzki, R., Pietrzyński, G., Urbaneja, M. A., & Carraro, G. 2009a, ApJ, 700, 309

Bresolin, F., & Kennicutt, Jr., R. C. 2002, ApJ, 572, 838

Bresolin, F., Kudritzki, R., Mendez, R. H., & Przybilla, N. 2001, ApJ, 548, L159

Bresolin, F., Pietrzyński, G., Urbaneja, M. A., Gieren, W., Kudritzki, R., & Venn, K. A. 2006, ApJ, 648, 1007

Bresolin, F., Ryan-Weber, E., Kennicutt, R. C., & Goddard, Q. 2009b, ApJ, 695, 580

Bresolin, F., Schaerer, D., González Delgado, R. M., & Stasińska, G. 2005, A&A, 441, 981

Bresolin, F., Urbaneja, M. A., Gieren, W., Pietrzyński, G., & Kudritzki, R. 2007, ApJ, 671, 2028

Brooks, A. M., Governato, F., Booth, C. M., Willman, B., Gardner, J. P., Wadsley, J., Stinson, G., & Quinn, T. 2007, ApJ, 655, L17

Brott, I., et al. 2011, A&A, 530, A115

Cardelli, J. A., Clayton, G. C., & Mathis, J. S. 1989, Astrophysical Journal, 345, 245

Cedrés, B., Cepa, J., Bongiovanni, Á., Castañeda, H., Sánchez-Portal, M., & Tomita, A. 2012, A&A, 545, A43

Chiavassa, A., Freytag, B., Masseron, T., & Plez, B. 2011, A&A, 535, A22

Colavitti, E., Matteucci, F., & Murante, G. 2008, A&A, 483, 401

Cunha, K., Sellgren, K., Smith, V. V., Ramirez, S. V., Blum, R. D., & Terndrup, D. M. 2007, ApJ, 669, 1011

Currie, T., et al. 2010, ApJS, 186, 191

Cushing, M. C., Vacca, W. D., & Rayner, J. T. 2004, PASP, 116, 362

Daflon, S., & Cunha, K. 2004, The Astrophysical Journal, 617, 1115

Dalcanton, J. J., et al. 2009, ApJS, 183, 67

Davies, B., et al. 2012, MNRAS, 419, 1871

Davies, B., Kudritzki, R., & Figer, D. F. 2010, MNRAS, 407, 1203

Davies, B., et al. 2013, ApJ, 767, 3

De Lucia, G., Kauffmann, G., & White, S. D. M. 2004, MNRAS, 349, 1101

de Rossi, M. E., Tissera, P. B., & Scannapieco, C. 2007, MNRAS, 374, 323

Deharveng, L., Peña, M., Caplan, J., & Costero, R. 2000, MNRAS, 311, 329

Dufour, R. J., Talbot, Jr., R. J., Jensen, E. B., & Shields, G. A. 1980, ApJ, 236, 119

Eldridge, J. J., Izzard, R. G., & Tout, C. A. 2008, MNRAS, 384, 1109

Ercolano, B., Wesson, R., & Bastian, N. 2010, MNRAS, 401, 1375

Evans, C. J., Bresolin, F., Urbaneja, M. A., Pietrzyński, G., Gieren, W., & Kudritzki, R. 2007, ApJ, 659, 1198

Evans, C. J., et al. 2011, A&A, 527, A50+

Finlator, K., & Davé, R. 2008, MNRAS, 385, 2181

Firnstein, M., & Przybilla, N. 2012, A&A, 543, A80

Freudling, W., Romaniello, M., Bramich, D. M., Ballester, P., Forchi, V., García-Dabló, C. E., Moehler, S., & Neeser, M. J. 2013, A&A, 559, A96

García-Rojas, J., & Esteban, C. 2007, ApJ, 670, 457

Garmany, C. D., & Stencel, R. E. 1992, A&AS, 94, 211

Garnett, D. R. 2004, in Cosmochemistry. The melting pot of the elements, ed. C. Esteban, R. García López, A. Herrero, & F. Sánchez , 171–216

Gazak, J. Z., Bastian, N., Kudritzki, R.-P., Adamo, A., Davies, B., Plez, B., & Urbaneja, M. A. 2013, MNRAS, 430, L35

Gazak, J. Z., et al. 2014a, ApJ, 787, 142

Gazak, J. Z., Davies, B., Kudritzki, R., Bergemann, M., & Plez, B. 2014b, ApJ, 788, 58

Grevesse, N., & Sauval, A. J. 1998, Space Sci. Rev., 85, 161

Groth, H.-G. 1961, ZAp, 51, 231

Gustafsson, B., Edvardsson, B., Eriksson, K., Jørgensen, U. G., Nordlund, Å., & Plez, B. 2008, A&A, 486, 951

Gustafsson, B., Edvardsson, B., Eriksson, K., Mizuno-Wiedner, M., Jørgensen, U. G., & Plez, B. 2003, in Astronomical Society of the Pacific Conference Series, Vol. 288, Stellar Atmosphere Modeling, ed. I. Hubeny, D. Mihalas, & K. Werner, 331

Hillier, D. J., & Miller, D. L. 1998, ApJ, 496, 407

Hosek, Jr., M. W., et al. 2014, ApJ, 785, 151

Humphreys, R. M., & Davidson, K. 1979, Astrophysical Journal, 232, 409, a&AA ID. AAA026.115.001

Kaufer, A., Venn, K. A., Tolstoy, E., Pinte, C., & Kudritzki, R.-P. 2004, AJ, 127, 2723

Kewley, L. J., & Ellison, S. L. 2008, ApJ, 681, 1183

Khan, R., Stanek, K. Z., Prieto, J. L., Kochanek, C. S., Thompson, T. A., & Beacom, J. F. 2010, ApJ, 715, 1094

Kobayashi, N., et al. 2000, SPIE

Kobulnicky, H. A., & Kewley, L. J. 2004, ApJ, 617, 240

Köppen, J., Weidner, C., & Kroupa, P. 2007, MNRAS, 375, 673

Kotulla, R., Fritze, U., Weilbacher, P., & Anders, P. 2009, MNRAS, 396, 462

Kudritzki, R., Urbaneja, M. A., Bresolin, F., Przybilla, N., Gieren, W., & Pietrzyński, G. 2008, ApJ, 681, 269

Kudritzki, R. P. 1973, PhD thesis, Diss. Tech. Univ. Berlin, 76 p.

Kudritzki, R. P. 1998, in Stellar astrophysics for the local group: VIII Canary Islands Winter School of Astrophysics, ed. A. Aparicio, A. Herrero, & F. Sánchez, 149

Kudritzki, R. P., Bresolin, F., & Przybilla, N. 2003, ApJ, 582, L83

Kudritzki, R.-P., Lennon, D. J., & Puls, J. 1995, in Science with the VLT, ed. J. R. Walsh & I. J. Danziger, 246

Kudritzki, R.-P., Urbaneja, M. A., Bresolin, F., Hosek, Jr., M. W., & Przybilla, N. 2014, ApJ, 788, 56

Kudritzki, R.-P., Urbaneja, M. A., Gazak, Z., Bresolin, F., Przybilla, N., Gieren, W., & Pietrzyński, G. 2012, ApJ, 747, 15

Kudritzki, R.-P., Urbaneja, M. A., Gazak, Z., Macri, L., Hosek, Jr., M. W., Bresolin, F., & Przybilla, N. 2013, ApJ, 779, L20

Kudryavtseva, N., et al. 2012, ApJ, 750, L44

Kurucz, R. L. 2005, Memorie della Societa Astronomica Italiana Supplementi, 8, 14

Larsen, S. S., et al. 2011, A&A, 532, A147

Larsen, S. S., Origlia, L., Brodie, J. P., & Gallagher, J. S. 2006, MNRAS, 368, L10

Lee, H., Skillman, E. D., & Venn, K. A. 2006, ApJ, 642, 813

Leitherer, C., & Heckman, T. M. 1995, ApJS, 96, 9

Leitherer, C., Ortiz Otálvaro, P. A., Bresolin, F., Kudritzki, R.-P., Lo Faro, B., Pauldrach, A. W. A., Pettini, M., & Rix, S. A. 2010, ApJS, 189, 309

Lequeux, J., Peimbert, M., Rayo, J. F., Serrano, A., & Torres-Peimbert, S. 1979, A&A, 80, 155

Levesque, E. M., Massey, P., Olsen, K. A. G., Plez, B., Josselin, E., Maeder, A., & Meynet, G. 2005, ApJ, 628, 973

Lundqvist, M., & Wahlgren, G. M. 2005, Nuclear Physics A, 758, 304

Magrini, L., Vílchez, J. M., Mampaso, A., Corradi, R. L. M., & Leisy, P. 2007, A&A, 470, 865

Maiolino, R., et al. 2008, A&A, 488, 463

Massey, P., Silva, D. R., Levesque, E. M., Plez, B., Olsen, K. A. G., Clayton, G. C., Meynet, G., & Maeder, A. 2009, ApJ, 703, 420

McCarthy, J. K., Kudritzki, R.-P., Lennon, D. J., Venn, K. A., & Puls, J. 1997, ApJ, 482, 757

McCarthy, J. K., Lennon, D. J., Venn, K. A., Kudritzki, R.-P., Puls, J., & Najarro, F. 1995, ApJ, 455, L135

Meynet, G., & Maeder, A. 2000, A&A, 361, 101

Moorwood, A., et al. 1998, The Messenger, 94, 7

Moustakas, J., Kennicutt, Jr., R. C., Tremonti, C. A., Dale, D. A., Smith, J.-D. T., & Calzetti, D. 2010, ApJS, 190, 233

Naylor, T. 2009, MNRAS, 399, 432

Nieva, M.-F., & Przybilla, N. 2012, A&A, 539, A143

Pagel, B. E. J., Edmunds, M. G., Blackwell, D. E., Chun, M. S., & Smith, G. 1979, MNRAS, 189, 95

Palacios, A., Gebran, M., Josselin, E., Martins, F., Plez, B., Belmas, M., & Lèbre, A. 2010, A&A, 516, A13

Pilyugin, L. S., & Thuan, T. X. 2005, ApJ, 631, 231

Plez, B. 2012, Turbospectrum: Code for spectral synthesis, astrophysics Source Code Library

Portegies Zwart, S. F., McMillan, S. L. W., & Gieles, M. 2010, ARA&A, 48, 431

Prantzos, N., & Boissier, S. 2000, MNRAS, 313, 338

Przybilla, N., Butler, K., Becker, S. R., & Kudritzki, R. P. 2006, A&A, 445, 1099

Ramírez, S. V., Sellgren, K., Carr, J. S., Balachandran, S. C., Blum, R., Terndrup, D. M., & Steed, A. 2000, ApJ, 537, 205

Rayner, J. T., Toomey, D. W., Onaka, P. M., Denault, A. J., Stahlberger, W. E., Vacca, W. D., Cushing, M. C., & Wang, S. 2003, PASP, 115, 362

Rolleston, W. R. J., Smartt, S. J., Dufton, P. L., & Ryans, R. S. I. 2000, A&A, 363, 537

Rosolowsky, E., & Simon, J. D. 2008, The Astrophysical Journal, 675, 1213, (c) 2008: The American Astronomical Society

Russell, H. N. 1914, Nature, 93, 252

Sana, H., et al. 2013, A&A, 550, A107

Sana, H., & Evans, C. J. 2011, in IAU Symposium, Vol. 272, IAU Symposium, ed. C. Neiner, G. Wade, G. Meynet, & G. Peters, 474–485

Sánchez-Blázquez, P., Courty, S., Gibson, B. K., & Brook, C. B. 2009, MNRAS, 398, 591

Saviane, I., Momany, Y., da Costa, G. S., Rich, R. M., & Hibbard, J. E. 2008, ApJ, 678, 179

Schweizer, F., et al. 2008, AJ, 136, 1482

Sharma, S., Pandey, A. K., Ojha, D. K., Chen, W. P., Ghosh, S. K., Bhatt, B. C., Maheswar, G., & Sagar, R. 2007, MNRAS, 380, 1141

Sidoli, F., Smith, L. J., & Crowther, P. A. 2006, MNRAS, 370, 799

Skrutskie, M. F., et al. 2006, AJ, 131, 1163

Smartt, S. J. 2009, ARA&A, 47, 63

Smartt, S. J., Crowther, P. A., Dufton, P. L., Lennon, D. J., Kudritzki, R. P., Herrero, A., McCarthy, J. K., & Bresolin, F. 2001, MNRAS, 325, 257

Smith, L. J., Westmoquette, M. S., Gallagher, J. S., O'Connell, R. W., Rosario, D. J., & de Grijs, R. 2006, MNRAS, 370, 513

Stasińska, G. 2005, A&A, 434, 507

Trancho, G., Bastian, N., Miller, B. W., & Schweizer, F. 2007, ApJ, 664, 284

Tremonti, C. A., et al. 2004, ApJ, 613, 898

Trundle, C., Dufton, P. L., Lennon, D. J., Smartt, S. J., & Urbaneja, M. A. 2002, A&A, 395, 519

U, V., Urbaneja, M. A., Kudritzki, R., Jacobs, B. A., Bresolin, F., & Przybilla, N. 2009, ApJ, 704, 1120

Urbaneja, M. A., Herrero, A., Kudritzki, R.-P., Najarro, F., Smartt, S. J., Puls, J., Lennon, D. J., & Corral, L. J. 2005, The Astrophysical Journal, 635, 311

Urbaneja, M. A., Kudritzki, R., Bresolin, F., Przybilla, N., Gieren, W., & Pietrzyński, G. 2008, ApJ, 684, 118

Vacca, W. D., Cushing, M. C., & Rayner, J. T. 2003, PASP, 115, 389

Venn, K. A. 1995a, ApJS, 99, 659

—. 1995b, ApJ, 449, 839

—. 1999, ApJ, 518, 405

Venn, K. A., et al. 2001, ApJ, 547, 765

Venn, K. A., McCarthy, J. K., Lennon, D. J., Przybilla, N., Kudritzki, R. P., & Lemke, M. 2000, ApJ, 541, 610

Venn, K. A., Tolstoy, E., Kaufer, A., Skillman, E. D., Clarkson, S. M., Smartt, S. J., Lennon, D. J., & Kudritzki, R. P. 2003, AJ, 126, 1326

Verhoelst, T., van der Zypen, N., Hony, S., Decin, L., Cami, J., & Eriksson, K. 2009, A&A, 498, 127

Vilchez, J. M., Pagel, B. E. J., Diaz, A. I., Terlevich, E., & Edmunds, M. G. 1988, MNRAS, 235, 633

Wahlgren, G. M., Nave, G., Nilsson, H., & Lundqvist, M. 2008, Journal of Physics Conference Series, 130, 012019

Whitmore, B. C., et al. 2011, ApJ, 729, 78

—. 2010, AJ, 140, 75

Whitmore, B. C., & Zhang, Q. 2002, AJ, 124, 1418

Wiersma, R. P. C., Schaye, J., Theuns, T., Dalla Vecchia, C., & Tornatore, L. 2009, MNRAS, 399, 574

Wolf, B. 1971, A&A, 10, 383

—. 1972, A&A, 20, 275

—. 1973, A&A, 28, 335

Yin, J., Hou, J. L., Prantzos, N., Boissier, S., Chang, R. X., Shen, S. Y., & Zhang, B. 2009, A&A, 505, 497

Zackrisson, E., Rydberg, C.-E., Schaerer, D., Östlin, G., & Tuli, M. 2011, ApJ, 740, 13

Zurita, A., & Bresolin, F. 2012, MNRAS, 427, 1463